

國立臺灣海洋大學

河海工程學系

碩士學位論文

指導教授：陳正宗 博士

零場積分方程求解含圓形邊界之應力集中問題

Null-field Integral Equation Approach for
Solving Stress Concentration Problems
with Circular Boundaries

研究生：陳柏源 撰

中華民國 95 年 6 月



零場積分方程求解含圓形邊界之應力集中問題

Null-field Integral Equation Approach for Solving
Stress Concentration Problems with Circular
Boundaries

研 究 生：陳柏源

Student：Po-Yuan Chen

指導教授：陳正宗

Advisor：Jeng- Tzong Chen

國 立 臺 灣 海 洋 大 學
河 海 工 程 學 系
碩 士 論 文

A Thesis
Submitted to Department of Harbor and River Engineering
College of Engineering
National Taiwan Ocean University
in partial Fulfillment of the Requirements
for the Degree of
Master of Engineering
in

Department of Harbor and River Engineering

June 2006

Keelung, Taiwan, Republic of China

中華民國 95 年 6 月

謝誌

「書山有路勤為徑，學海無涯苦作舟」，碩士兩年的寫照，一語道破。回首兩年前，初生之犢不畏虎，毅然決然投入 陳正宗 教授門下，總覺得學長口中勸退小學弟的言語，言過其實，直到進入研究室，從老師身上看到執著、認真的態度，才了解做學問應有的嚴謹態度。兩年研究室的洗禮，在學長們成績的壓力之下，莫名的有股責任感要把持住研究室的水平，從上課到做研究都不斷的告誡自己要比別人更加努力；兩年來學習到做研究執著的態度，以及面對難題時該怎麼解決是我最大的收穫。

「師之教、記於心，師之情、長相憶」，由衷感謝 陳正宗 老師兩年來無微不至的耳提面命叮嚀，撰寫論文期間不厭其煩地審閱修正，得以順利完成這本論文。

論文口試期間，感謝三位國科會特約研究員 台大楊德良教授、台科大趙振綱教授、成大陳東陽教授，以及宜蘭大學李洋傑博士悉心指教，寶貴的意見使本論文更加完善，由衷感謝。研究所期間，感謝中興顧問公司呂學育老師，學業上與生活上對學生的關心。

回首風風雨雨的基隆生活，感謝同甘共苦的同窗安傑，從修課到做玩樂、從醫院再把我拉回研究軌道，一路伴隨砥礪；在我生命中不斷加入的好友，欣怡、英豪、雅筑、宇書、雨軒、勝凱、怡真、文廣、靖筠、秀堅、宗慶、筱靖、欣瑜、彥彰、尚津、勁毅、世勸、家俊、俊豪、珮敏、怡君、家綾，在二十多年的日子裡激起許許多多的漣漪，讓生命充滿驚奇。求學期間，感謝研究室學長，桂鴻、應德、清森、文成、嘉俊、佳聰，在學業及生活上的指導，感謝研究室同學與學弟，政宏、奐禎、佳男，處處給予協助並分擔了許多研究室大小事情。再者，感謝國科會計畫 NSC 94-2115-M-019-003 提供之碩士生獎學金，讓我於做研究時無經濟之壓力。

能夠順利取得碩士學位，特別要感謝我的家人，爸爸、媽媽，大姐、二姐，還有加入我的家人行列的姊夫以及小姪女，給了我強大的後盾，無憂鬱地去完成我的目標。

學生生涯暫時告一段落，接下來的，待續～

基隆 仲夏 2006

Null-field integral equation approach for solving stress concentration problems with circular boundaries

Contents

Contents

Table captions

Figure captions

Notations

Abstract

中文摘要

Chapter 1 Introduction

1.1 Motivation of the research	1
1.2 Organization of the thesis	6

Chapter 2 Null-field integral equation formulation

Summary	8
2.1 Dual boundary integral formulation for domain point	8
2.2 Expansions of fundamental solution and boundary density	10
2.2.1 Degenerate kernels for the fundamental solution	10
2.2.2 Fourier series expansion for the boundary density	10
2.3 Adaptive observer system	11
2.4 Vector decomposition technique for the potential gradient in the hypersingular equation	11
2.5 Linear algebraic equation	12
2.6 Matching of interface conditions for problems of cavities and inclusions	15

2.7 Concluding remarks	16
Chapter 3 Application to Laplace problems	
Summary	17
3.1 Introduction	17
3.2 Degenerate kernels of BIE formulation for Laplace problems	19
3.3 Torsion problem for a bar	21
3.3.1 Problem statements	21
3.3.2 Illustrative examples and discussions	23
3.4 Bending problem for a cantilever beam	24
3.4.1 Problem statements	24
3.4.2 Illustrative examples and discussions	26
3.5 Concluding remarks	27
Chapter 4 Application to exterior Helmholtz problems	
Summary	29
4.1 Introduction	29
4.2 Degenerate kernels of BIE formulation for the Helmholtz problem	30
4.3 Image technique for solving scattering problems of half-plane	33
4.4 Half-plane problems with a cavity subject to the incident SH-wave	34
4.4.1 Problem statement	34
4.4.2 Illustrative examples and discussions	36
4.5 Half-plane problems with inclusions subject to the incident SH-wave	37
4.5.1 Problem statement	37
4.5.2 Illustrative examples and discussions	40
4.6 Concluding remarks	43
Chapter 5 Derivation of Green's function and Poisson integral formula for annular Laplace problems	
Summary	45
5.1 Introduction	45

5.2	Derivation of the Green's function for annular Laplace problems	46
5.2.1	Problem statement and null-field approach to construct the Green's function	46
5.2.2	Expansions of kernel and boundary density	47
5.3	Series representation for the Green's function of annular case	48
5.4	An illustrative example and discussions	50
5.5	Concluding remarks	51
Chapter 6 Conclusions and further research		
6.1	Conclusions	52
6.2	Further research	54
References		56
Appendix		
Appendix	Analytical evaluation of the integrals for Laplace kernels	65
Appendix	Analytical evaluation of the integrals for Helmholtz kernels	67
Appendix	Image concept and the decomposition of superposition of a circular cavity	75
Appendix	Image concept and the decomposition of superposition of a alluvial valley	76
Appendix	Limiting process of annular Green's function reduce to exterior cases.	77

Table captions

Table 1-1	Comparisons of the present method and conventional BEM.	79
Table 3-1	Comparison of formulation between the present approach and conventional BEM	80
Table 3-2	Torsional rigidity of a circular cylinder with a single eccentric hole ($a/R=1/3$)	81
Table 3-3	Torsional rigidity of a circular cylinder with a ring of N holes $a/R=1/4$, $b/R=1/2$	82
Table 3-4	Torsional rigidity in Ling's examples	82
Table 5-1	Green's function of interior and exterior problem	83
Table 5-2	Green's function of annular case	84

Figure captions

Figure 1-1	The boundary value problems with arbitrary boundaries.	85
Figure 2-1	Problem statement.	86
Figure 2-2 (a)	The 1-D degenerate kernel for $U(s,x)$.	87
Figure 2-2 (b)	The 2-D degenerate kernel for $U(s,x)$.	87
Figure 2-2 (c)	The 3-D degenerate kernel for $U(s,x)$.	87
Figure 2-3 (a)	Sketch of the null-field integral equation in conjunction with the adaptive observer system.	88
Figure 2-3 (b)	Sketch of the boundary integral equation for the domain point in conjunction with the adaptive observer system.	88
Figure 2-4	Vector decomposition for the potential gradient in the hypersingular equation.	89
Figure 2-5	The flowchart of the present method.	90
Figure 3-1	Cross section of a bar weakened by N ($N = 3$) equal circular holes.	91
Figure 3-2	Torsion rigidity versus the number of Fourier terms.	92
Figure 3-3	Cross-section of a cantilever beam of symmetrical holes.	93
Figure 3-4	Stress concentration for $R = 1.0$, $b = 0.5$, $\bar{\theta} = \pi/4$ and $a = 0.1$.	94
Figure 3-4 (a)	Sc along AB (Present method)	94
Figure 3-4 (b)	Sc along CD (Present method)	94
Figure 3-4 (c)	Sc along OT (Present method)	94
Figure 3-4 (d)	Sc along AB (Naghdi's result)	94
Figure 3-4 (e)	Sc along CD (Naghdi's result)	94
Figure 3-4 (f)	Sc along OT (Naghdi's result)	94
Figure 3-5	Stress concentrations around the third circle (a) $\bar{\theta} = 22.5$ (b) $\bar{\theta} = 45$ (c) $\bar{\theta} = 67.5$.	95
Figure 3-6	Stress concentration versus b for $a = 0.12$ and $R = 1.0$.	96
Figure 3-6 (a)	$\bar{\theta} = \pi/8$ (Present method).	96
Figure 3-6 (b)	$\bar{\theta} = 3\pi/8$ (Present method).	96
Figure 3-6 (c)	$\bar{\theta} = \pi/8$ (Bird's result).	96
Figure 3-6 (d)	$\bar{\theta} = 3\pi/8$ (Bird's result).	96
Figure 3-7	Stress concentration versus b for $a = 0.12$, $R = 1.0$ and three different values of $\bar{\theta} = \pi/8$, $\bar{\theta} = \pi/4$ and $\bar{\theta} = 3\pi/8$.	97
Figure 3-7 (a)	Sc at the point B (Present method)	97

Figure 3-7 (b)	Sc at the point B (Naghdi's result)	97
Figure 3-8	Stress concentration along \overline{AB} and extremely close to the point B for $b=5$, $a=1$, $R=10$ and $\bar{\theta}=\pi/4$.	98
Figure 3-9	Stress concentration on point B for $R=1.0$, $b=0.5$, $\bar{\theta}=\pi/4$ and $a=0.1$.	98
Figure 3-10	Contour plot for $R=1.0$, $b=0.4$, $a=0.12$ for three various values of (a) $\bar{\theta}=\pi/8$, (b) $\bar{\theta}=\pi/4$ and (c) $\bar{\theta}=3\pi/8$.	99
Figure 3-11	Cantilever beam under bending weakened by two holes the on $x-axis$.	100
Figure 3-12	Stress concentration versus $D/2a$ for the point P .	100
Figure 3-12 (a)	Present method.	100
Figure 3-12 (b)	Bird's result.	100
Figure 3-13	Contour of stress concentration of $D/2a=0.0625$.	101
Figure 3-13 (a), (b)	Present method.	101
Figure 3-13 (c), (d)	Bird's result.	101
Figure 4-1	A half-plane problem with a circular cavity subject to incident SH-wave.	102
Figure 4-2	A full-plane problem with two cavities subject to the incident SH-wave.	103
Figure 4-2 (a)	Two cavities with centers on the $y-axis$.	103
Figure 4-2 (b)	Two cavities with centers on the $45^\circ-axis$.	103
Figures 4-2 (c)~(d)	Shear stress around the smaller cavity (Honein's result).	103
Figures 4-2 (e)~(f)	Shear stress around the smaller cavity (Present method).	103
Figure 4-3	Shear stress ($\sigma_{\theta z}$) around the cavity of a full-plane problem subject to the horizontally incident SH wave.	104
Figure 4-3 (a)	A full-plane problem with a cavity subject to SH-wave.	104
Figure 4-3 (b)	Pao and Mow's result (only half).	104
Figure 4-3 (c)	Present method ($\gamma=90^\circ$).	104
Figure 4-4	Shear stress ($\sigma_{\theta z}^*$) around the cavity under the ground surface subject to the SH-wave.	105
Figures 4-4 (a)~(d)	Present method.	105
Figures 4-4 (e)~(h)	Lin and Liu's results.	105
Figure 4-4 (i)	Limiting case of $\gamma=0^\circ$ and $h/a=100$.	105
Figure 4-5	A half-plane problem with a semi-circular alluvial valley subject to the SH-wave.	106
Figure 4-6	Surface amplitudes of the alluvial valley problem for $\eta=0.5$ ($h/a=1$, $\mu^I/\mu^M=1/6$ and $\rho^I/\rho^M=2/3$).	107

Figures 4-6 (a) ~ (d)	Present method.	107
Figures 4-6 (e) ~ (h)	Manoogian's results.	107
Figure 4-7	Surface amplitudes of the alluvial valley problem for $\eta = 1.0$ ($h/a = 1, \mu^I / \mu^M = 1/6$ and $\rho^I / \rho^M = 2/3$).	108
Figures 4-7 (a) ~ (d)	Present method.	108
Figures 4-7 (e) ~ (h)	Manoogian's results.	108
Figure 4-8	Surface amplitudes of the alluvial valley problem for $\eta = 1.5$ ($h/a = 1, \mu^I / \mu^M = 1/6$ and $\rho^I / \rho^M = 2/3$).	109
Figures 4-8 (a) ~ (d)	Present method.	109
Figures 4-8 (a) ~ (d)	Manoogian's results.	109
Figure 4-9	Surface amplitudes of the alluvial valley problem for $\eta = 2.0$ ($h/a = 1, \mu^I / \mu^M = 1/6$ and $\rho^I / \rho^M = 2/3$).	110
Figures 4-9 (a) ~ (d)	Present method.	110
Figures 4-9 (a) ~ (d)	Manoogian's results.	110
Figure 4-10	Limiting case of a canyon for $\mu^I / \mu^M = 10^{-8}$ and $\eta = 0.5$ ($h/a = 1$ and $\rho^I / \rho^M = 2/3$).	111
Figures 4-10 (a) ~ (d)	Present method.	111
Figures 4-10 (e) ~ (h)	Manoogian's results.	111
Figure 4-11	Limiting case of a canyon for $\mu^I / \mu^M = 10^{-8}$ and $\eta = 1$ ($h/a = 1$ and $\rho^I / \rho^M = 2/3$).	112
Figures 4-11 (a) ~ (d)	Present method.	112
Figures 4-11 (e) ~ (h)	Manoogian's results.	112
Figure 4-12	Limiting case of a canyon for $\mu^I / \mu^M = 10^{-8}$ and $\eta = 1.5$ ($h/a = 1$ and $\rho^I / \rho^M = 2/3$).	113
Figures 4-12 (a) ~ (d)	Present method.	113
Figures 4-12 (e) ~ (h)	Manoogian's results.	113
Figure 4-13	Limiting case of a canyon for $\mu^I / \mu^M = 10^{-8}$ and $\eta = 2.0$ ($h/a = 1$ and $\rho^I / \rho^M = 2/3$).	114
Figures 4-13 (a) ~ (d)	Present method.	114
Figures 4-13 (e) ~ (h)	Manoogian's results.	114
Figure 4-14	Limiting case of a rigid alluvial valley ($\mu^I / \mu^M = 10^4$, $\eta = 2$, $h/a = 1$ and $\rho^I / \rho^M = 2/3$).	115
Figure 4-15	Surface displacements as a function of x/a and η for the vertical incidence ($\gamma = 0^\circ$, $\rho^I / \rho^M = 2/3$ and $c^I / c^M = 1/2$).	116
Figure 4-15 (a)	Present method.	116
Figure 4-15 (b)	Trifunac's result.	116
Figure 4-16	Surface displacements as a function of x/a and η for the	117

	vertical incidence ($\gamma = 0^\circ$, $\rho^I / \rho^M = 2/3$ and $c^I / c^M = 1/3$).	
Figure 4-16 (a)	Present method.	117
Figure 4-16 (b)	Trifunac's result.	117
Figure 4-17	Spectral displacement with harder material of alluvial valley versus the dimensionless frequency η for the vertically incident SH-wave. ($\rho^I / \rho^M = 3/2$ and $c^I / c^M = 2$).	118
Figure 4-17 (a)	Present method.	118
Figure 4-17 (b)	Trifunac's result.	118
Figure 4-18	Spectral amplification at $x/a = 0.8$ versus the dimensionless frequency η .	119
Figure 4-19	Spectral amplification at $x/a = -0.8$ versus the dimensionless frequency η .	120
Figure 4-20	A half-plane problem with two alluvial valleys subject to the incident SH-wave.	121
Figure 4-21	Surface displacements of two alluvial valleys ($\mu^I / \mu^M = 1/6$ and $\rho^I / \rho^M = 2/3$). (a) ~ (d) $\eta = 0.5$, (e) ~ (h) $\eta = 1.0$.	122
Figure 4-22	Surface displacements of two alluvial valleys ($\mu^I / \mu^M = 1/6$ and $\rho^I / \rho^M = 2/3$). (a) ~ (d) $\eta = 1.5$, (e) ~ (h) $\eta = 2.0$.	123
Figure 4-23	Limiting case of two canyons ($\mu^I / \mu^M = 10^{-8}$ and $\eta = 1$).	124
Figures 4-23 (a) ~ (d)	Present method.	124
Figures 4-23 (e) ~ (h)	Tsaur <i>et al.</i> 's results.	124
Figure 4-24	Limiting case of two canyons ($\mu^I / \mu^M = 10^{-8}$ and $\eta = 2$).	125
Figures 4-24 (a) ~ (d)	Present method.	125
Figures 4-24 (e) ~ (h)	Tsaur <i>et al.</i> 's results.	125
Figure 4-25	A half-plane problem with a circular inclusion subject to the incident SH-wave.	126
Figure 4-26	Surface displacements of the inclusion problem under the ground surface with $\eta = 2$ and $h/a = 1.5$ ($\mu^I / \mu^M = 1/6$ and $\rho^I / \rho^M = 2/3$).	127
Figures 4-26 (a) ~ (d)	Present method.	127
Figures 4-26 (e) ~ (h)	Tsaur <i>et al.</i> 's results.	127
Figures 4-26 (i) ~ (l)	Manoogian and Lee's results.	127
Figure 4-27	Surface amplitudes of a inclusion problem for various values of η and $h/a = 1.5$ ($\mu^I / \mu^M = 1/6$ and $\rho^I / \rho^M = 2/3$), (a) ~ (d) $\eta = 0.5$, (e) ~ (h) $\eta = 1.0$, (i) ~ (l) $\eta = 1.5$.	128

Figure 4-28	Limiting case of a cavity problem ($\mu^I / \mu^M = 10^{-8}$ and $h/a = 1.5$).	129
Figures 4-28 (a) ~ (d)	Present method ($\eta = 2$ and $\rho^I / \rho^M = 2/3$).	129
Figures 4-28 (e) ~ (h)	Lee and Manoogian's results for the cavity case.	129
Figure 4-29	Limiting case of a cavity problem ($\mu^I / \mu^M = 10^{-8}$ and $h/a = 5$).	130
Figures 4-29 (a) ~ (d)	Present method ($\eta = 2$ and $\rho^I / \rho^M = 2/3$).	130
Figures 4-29 (e) ~ (h)	Lee and Manoogian's results for the cavity case.	130
Figure 4-30	Limiting case of a rigid inclusion problem ($\mu^I / \mu^M = 10^4$, $h/a = 1.5$, $\rho^I / \rho^M = 2/3$ and $\eta = 2$).	131
Figure 4-31	A half-plane problem with two circular inclusions subject to the SH-wave.	132
Figure 4-32	Surface amplitudes of two-inclusions problem ($\mu^I / \mu^M = 1/6$, $\rho^I / \rho^M = 2/3$, $h/a = 1.5$, $D/a = 2.5$ and $L = 10$).	133
Figure 4-33	Limiting case of two-cavities problem ($\mu^I / \mu^M = 10^{-8}$, $\rho^I / \rho^M = 2/3$, $h/a = 1.5$, $D/a = 2.5$ and $L = 10$).	134
Figures 4-33 (a) ~ (d)	Present method.	134
Figures 4-33 (e) ~ (h)	Jiang <i>et al.</i> result.	134
Figure 5-1	Two-dimensional annular problems.	135
Figure 5-1 (a)	Green's function of annular case.	135
Figure 5-1 (b)	Annular Dirichlet problem.	135
Figure 5-2	Two limiting cases ($a \rightarrow 0, b \rightarrow \infty$) of annular Green's function.	136
Figure 5-2 (a)	Limiting case of annular Green's function ($a = 1, b = 10^7, L = 20$ and $\xi(1.25, 0^\circ)$).	136
Figure 5-2 (b)	Limiting case of annular Green's function ($a = 0.001, b = 1, L = 20$ and $\xi(0.8, 0^\circ)$).	136
Figure 5-2 (c)	Series-form Green's function of exterior case.	136
Figure 5-2 (d)	Series-form Green's function of interior case.	136
Figure 5-3	Contour plot for the annular Green's function.	137
Figure 5-3 (a)	Analytical solution ($L = 50$).	137
Figure 5-3 (b)	Semi-analytical solution ($L = 50$).	137

Notations

a	radius of a circular hole
a_n, b_n	Fourier coefficients of boundary density $u(s)$
A	area of beam cross section
b	radius of the ring
B	boundary
c	velocity of shear wave
c_k	center of the circle ($k = 0, 1, 2, \dots$)
$C.P.V.$	Cauchy principal value
D	distance between the circles at the closest points
G	torsional rigidity
$G(x, \xi)$	Green's function
h	depth from ground to the center of circle
$H.P.V.$	Hadamard principal value
$H_n^{(1)}(\cdot)$	n th order Hankel function of the first kind
$[I]$	identity matrix
$\text{Im}(\cdot)$	imaginary part of complex variable
$J_n(\cdot)$	the n th order Bessel function of the first kind
J_n^i	the i th zero for the n th order Bessel function $J_n(\cdot)$
$J'_n(\cdot)$	the derivative of $J_n(\cdot)$
k	wave number
L	truncated terms of Fourier series
$L(s, x)$	kernel function in the hypersingular formulation
$L^i(s, x)$	degenerate kernel function of $L(s, x)$ for $R > \rho$
$L^e(s, x)$	degenerate kernel function of $L(s, x)$ for $\rho > R$
$M(s, x)$	kernel function in the hypersingular formulation
$M^i(s, x)$	degenerate kernel function of $M(s, x)$ for $R \geq \rho$
$M^e(s, x)$	degenerate kernel function of $M(s, x)$ for $\rho > R$
n	normal vector
n_s	normal vector at the source point s
n_x	normal vector at the field point x
N	number of the circles
p_n, q_n	Fourier coefficients for the boundary density of $t(s)$
Q	shear force
R	radius of the outer boundary

$R.P.V.$	Riemann principal value
$\text{Re}(\cdot)$	real part of complex variable
r	distance between the source point s and the field point x , $r \equiv x-s $
s	source point
Sc	stress concentration
t_x, t_y, t_z	traction in the x , y and z directions
$\{\mathbf{t}\}$	vector of Fourier coefficients $\{p_0 \ p_1 \ q_1 \ \cdots \ p_M \ q_M\}^T$
T	torque
$T(s, x)$	kernel function in the singular formulation
$T^i(s, x)$	degenerate kernel function of $T(s, x)$ for $R > \rho$
$T^e(s, x)$	degenerate kernel function of $T(s, x)$ for $\rho > R$
$[\mathbf{T}]$	influence matrix of the kernel function $T(s, x)$
$t(s)$	normal derivative of $u(s)$ at s
$t(x)$	normal derivative of $u(x)$ at x
$U(s, x)$	kernel function in the singular formulation
$U^i(s, x)$	degenerate kernel function of $U(s, x)$ for $R \geq \rho$
$U^e(s, x)$	degenerate kernel function of $U(s, x)$ for $\rho > R$
$[\mathbf{U}]$	influence matrix of the kernel function $U(s, x)$
$\{\mathbf{u}\}$	vector of Fourier coefficients $\{a_0 \ a_1 \ b_1 \ \cdots \ a_M \ b_M\}^T$
$\{\mathbf{u}(\mathbf{x})^{i+r}\}$	vector of forcing term
u, v, w	displacement in the x , y and z directions
$u(s)$	potential function on the source point s
$u(x)$	potential function on the field point x
x	field point
(x_k, y_k)	boundary point for the k th circle
$Y_n(\cdot)$	the n th order Bessel function of the second kind
Y_n^i	the i th zero for the n th order Bessel function $Y_n(\cdot)$
$Y_n'(\cdot)$	the derivative of $Y_n(\cdot)$
α	angle of twist per unit length
$\delta(x-s)$	Dirac-delta function
$\varepsilon_x, \varepsilon_y, \varepsilon_z$	normal strain in the x , y and z directions
\mathbf{f}	differential operator
γ	incident angle of SH-wave
$\gamma_{xy}, \gamma_{xz}, \gamma_{yz}$	shear strain
ν	Possion's ratio
μ	shear modulus
$[\boldsymbol{\mu}]$	diagonal matrix of shear modulus

ρ	density
ω	angular frequency
η	dimensionless frequency
λ	wavelength of SH-wave
φ	warping function
ψ	bending function
ξ, ξ'	concentrated source point and image source point of Green's function
$\sigma_{xx}, \sigma_{yy}, \sigma_{zz},$	stress components
$\sigma_{xy}, \sigma_{xz}, \sigma_{yz}$	
τ^∞	shear stress applied at infinity
θ	polar angle measured related to x_1 direction
$\bar{\theta}$	angle of the layout of holes
Ω	domain of interest
Ω^c	complementary domain
(R, θ)	polar coordinate of s
(ρ, ϕ)	polar coordinate of x
∇^2	Laplacian operator
“ f ”	external force
“ i ”	incident waves
“ I ”	inclusion
“ M ”	matrix
“ r ”	reflected waves
“ t ”	total field including radiation and scattering

“ ” denotes the superscript or subscript

Abstract

In the thesis, boundary value problems with circular boundaries are formulated in a unified manner by using null-field integral equation in conjunction with degenerate kernels and Fourier series expansions. Laplace problems of circular holes as well as Helmholtz problem of SH-wave impinging on circular cavities and/or inclusions were studied. The fundamental solution is expanded to degenerate form by separating the source point and field point in the polar coordinate. The main gain of using degenerate kernels for interior and exterior expansions is free of calculating the principal values. In order to fully describe the circular boundary, the present method employs the Fourier series to approximate the boundary potential. By collocating the null-field points on the real boundary with the same number of Fourier coefficients, the unknown coefficients in the algebraic system can be easily determined. The present method is treated as a “semi-analytical” solution since error only attributes to the truncation of Fourier series. Four advantages, well-posed model, principal value free, elimination of boundary-layer effect and exponential convergence, are achieved. Besides, the null-field approach in conjunction with degenerate kernels and Fourier series expansions is also employed to derive the Green’s function for boundary value problems stated for annular problems of Laplace equations and the generalized Poisson integral formula is obtained. Finally, several examples involving torsion, bending, and infinite domain with cavity and half-plane with alluvial valleys and inclusions problem were given to demonstrate the validity of the proposed method. Also, the numerical results agree well after comparing with available solutions in the literature. A general-purpose program for multiple circular cavities and/or inclusions of various radii and arbitrary positions was developed.

Keywords: degenerate kernel, Fourier series, null-field integral equation, Laplace and Helmholtz problem, Green’s function, inclusion.

中文摘要

本文係使用零場積分方程搭配分離核函數與傅立葉級數求解含圓形邊界之問題。文中，不僅將求解含圓孔洞之拉普拉斯問題，SH 波入射圓洞和/或置入物之赫姆茲問題也將一併探討。在此，基本解將以場、源點分離的概念展開為分離（退化）的型式，而邊界物理量則使用傅立葉級數展開。藉由分離核函數的內域與外域表示式，可解析計算所有的邊界積分而免於計算主值的困擾。均勻分佈與傅立葉係數相同個數之觀察點於真實邊界上，因此，未知傅立葉係數即可輕易地求得。由於誤差僅來自於擷取有限項的傅立葉級數，故本方法可視為“半解析法”。此方法具(1) 良態模式；(2) 無需主值計算；(3) 無邊界層效應；(4) 指數收斂，等四大優勢。此外，此法亦被利用推導同心圓環之格林函數的拉普拉斯問題並推導廣義 Poisson 積分方程。最後，為了驗證此方法的可行性與正確性，對於扭轉、彎矩，含圓孔之全平面與含沉積土或置入物之半平面問題均予以測試，所得的數值結果也與文獻中之結果進行比較，均能得到不錯的結果。我們開發一套系統性求解含任意數目、不同大小與位置的圓孔洞和/或置入物分析拉普拉斯與赫姆茲問題的程式。

關鍵字：分離核函數、傅立葉級數、零場積分方程、拉普拉斯與赫姆茲問題、格林函數、置入物。

Chapter 1 Introduction

1.1 Motivation of the research

Engineering problems with circular holes are often encountered, *e.g.* missiles, aircraft, naval architecture, etc., either to reduce the weight of the whole structure or to increase the range of inspection as well as piping purposes. An analytical approach using the bi-polar coordinate [49] was developed for two-holes problems. Complex variable techniques were also employed for the annular case using technique of conformal mapping. For a problem with several holes, various numerical methods, *e.g.* finite difference method (FDM), finite element method (FEM), boundary element method (BEM) and meshfree method, *etc.* are always resorted to solve. Among diverse numerical approaches, FEM and BEM have become popular research tools for engineers. In the past decade, FEM has been widely applied to carry out many engineering problems, but one disadvantage is that discretizations on the domain are time-consuming to set up the mesh models. Regarding to the benefit of using BEM, only discretizations on boundaries are required and the boundary conditions at infinity are automatically satisfied. Although BEM has been involved as an alternative method for solving engineering problems, four critical issues are of concern.

(1) It is well-know that improper integrals (weak, strong and hypersingular) should be handled particularly when BEM is used. Hong and Chen [101] have developed the theory of dual boundary integral equation (BIE) and dual BEM containing hypersingular kernels. In the dual BIEM/BEM formulation, the singular and hypersingular integrals need special care on the sense of the Cauchy and Hadamard principal values, respectively. How to determine accurately the free terms has received more attentions in the past decade and a large amount of papers can be found. In the past, many researchers proposed several regularization techniques to deal with the singularity and hypersingularity. Two conventional approaches were employed to regularize the singular and hypersingular integrals. First, Guiggiani [42] has derived the free terms for Laplace and Navier equations using differential geometry and bump contour approach. Second, Gray and Manne [40] have employed a limiting process to

ensure a finite value from an interior point to boundary by using symbolic software. Two alternatives, fictitious BEM and null-field approach (off boundary approach), can avoid the singularity since the source and field points never coincide in the boundary integration. However, they result in an ill-posed matrix which will be elaborated on later. This indicates that direct problem instead of inverse one is solved by an ill-posed model. How to extract principle values of singularity and hypersingularity using the well-posed model is one of our objects in this thesis.

(2) On the other hand, many researchers tried to regularize the approach to regular formulation. In order to avoid directly calculating the singular and hypersingular integrals, null-field approach or fictitious BEM yields an ill-condition system which needs regularization. Achenbach *et al.* [1] employed the off-boundary approach in order to overcome the fictitious frequencies free of singularity. Null field integral equation approach is used widely for obtaining the numerical solutions of engineering problems. Various names, *e.g.*, T-matrix method [83] and extended boundary condition method (EBCM) [37] have been coined. A crucial advantage of this method consists in the fact that the influence matrix can be computed easily. Although many works for acoustic and water wave problems have been done, we focus on the solid mechanics here. By moving the null-field points to the real boundary or adjusting the fictitious boundary to the real boundary, the system can be changed to be well-posed. However, CPV and HPV need to be calculated. To construct a well-posed mathematical formulation free of singularity and hypersingularity as well as no need of regularization technique is not trivial. In the thesis, we may wonder whether it is possible to push the null-field point on the real boundary but free of calculating singularity and hypersingularity. The answer is yes. Instead of determining the singular (hypersingular) integrals using the definition of CPV (HPV), the kernel function is described in an analytical form from each side (interior and exterior) by employing the separable technique since the double-layer potential is discontinuous across the boundary. Therefore, degenerate kernel, namely separable kernel, is employed to represent the potential of the perforated domain which satisfies the governing equation.

(3) Boundary-layer effect is inherent in BEM. In real applications, data near boundary

can be artificially smoothened Laplace field satisfies maximum and minimum principles; nevertheless, it also deserves study to know how to manipulate the nearly singular integrals. Chen and Hong [23] regularized the boundary-layer effect by subtracting the boundary density with the constant and linear terms. Chen *et al.* [18] in China independently also using the similar idea. Zhou [94] proposed an analytical approach to calculate the nearly singular integrals and could avoid the appearance of boundary-layer effect. We may wonder whether it is possible to develop a BIEM formulation which is free of boundaries-layer effect. Readers can find the answer in this thesis.

(4) Convergence rate is the main concern of BEM. It is no doubt that dual BEM is very versatile for boundary value problems (BVPs) with general geometries including circular holes, ellipse, square and crack boundaries as shown in Figure 1-1. Regarding to constant, linear and quadratic elements, the discretization scheme does not take the geometry into consideration. For problems with special geometries, one can propose the special function to approximate the geometry. Legendre and Chebyshev polynomials are suited to approximate the boundary densities on the regular and degenerate boundaries, respectively. Fourier series is specially tailored to problems with circular geometries. Bird and Steele [6-8] presented a Fourier series procedure to solve circular plate problems containing multiple circular holes in a similar way of Trefftz method by adopting the interior and exterior T-complete sets. The Fourier procedure is an extension of their earlier work for the Laplace equation [8]. The lateral displacement, slope, bending moment and shear force of plates subject to different boundary conditions (essential and natural boundary condition and so on) can be obtained by using the Bird and Steele's formulation [8]. Either the interior or exterior bases in the Trefftz method are embedded in degenerate kernels [32]. The relation between the Trefftz method and the method of fundamental solutions (MFS) was constructed by using the degenerate kernels by Chen's Group [32]. The main advantage by using Fourier series to expand the boundary function on circular boundaries is that no mesh generation is required. Caulk and Barone [12-15] have solved the Laplace problem in two-dimensional region with circular holes by using the special boundary integral equations. In their approach, the boundary potential and

its normal derivative were both approximated by using Fourier series on each hole. Crouch and Mogilevskaya [36] utilized Somigliana's formula and Fourier series for elasticity problems with circular boundaries. Mogilevskaya and Crouch [65] have solved the problem of an infinite plane containing arbitrary number of circular inclusions based on the complex singular integral equation. In their analysis procedure, the unknown tractions are approximated by using complex Fourier series. However, for calculating an integral over a circular boundary, they didn't express the fundamental solution using the local polar coordinate. Another disadvantage is that the cavity can not be treated as a limiting case of inclusion [65]. Kress [48] has proved that expansion of degenerate kernel and Fourier series yield the exponential convergence instead of linear algebraic convergence using BEM. This thesis will take advantage of this expansion to deal with problems containing circular boundary using Fourier series in conjunction with degenerate kernel.

Since the fundamental solutions can be expanded into separable forms in the polar coordinate to avoid the singularity and hypersingularity, we focus on the problems with circular boundaries in this thesis. Once the fundamental solution can be separated in the other coordinate, *e.g.* Cartesian or elliptic coordinate; the same idea can be applied to solve for problems with different shapes of boundaries by considering corresponding special function to approximate the geometry without any difficulty. Recently, Chen's group [16,17,20,22,27-30,33,46,72,73] applied the null-field integral formulation, Fourier series and degenerate kernels to solve Laplace, Helmholtz and biharmonic problems with circular holes. Following the success of their idea, a semi-analytical approach is extended to solve the stress concentration for Laplace and Helmholtz equations with multiple circular holes and/or inclusions subject to the SH-wave in this thesis. Half-plane problems containing alluvial valleys, inclusions and cavities are our concern.

In this thesis, the stress concentration around holes of a beam under torsion or bending is one of our concerns. Chen and Weng [34] have introduced conformal mapping with a Laurent series expansion to analyze the Saint-Venant torsion problem. They determined the torsional rigidity of an eccentric bar containing different materials with an imperfect interface under torque. Because the conformal mapping is

limited to the doubly connected region, an increasing number of researchers have paid more attentions on special solutions. Recently, Honein *et al.* [44] have investigated the antiplane problem by using the Möbius transformation for two-holes problems. The effect of stress concentration due to different orientations was also conducted. Analytical solutions for the flexure of circular cylindrical beams with one eccentric circular cylindrical hole, according to the Saint-Venant theory [75,78], have been obtained in a few investigations. In 1991, Naghdi [68] has employed a special class of basis functions to solve the bending problem of a circular cylinder with $4N(N=1,2,3,...)$ circular cylindrical cavities in the axial direction. Bird and Steele [8] have revisited the bending problem with an arbitrary number and various location by using the Fourier series method. Comparing with the results of Naghdi [68] and those of Bird and Steele [8], the two approaches disagree by over ten percents. The grounds for the discrepancy have not yet been identified. However, the extension of above special solution to multiple circular holes may encounter difficulty. To develop a systematic method for solving the bending problems with circular boundaries is not trivial. According to the foregoing reasons, this thesis focuses on a systematic approach for problems containing multiple circular holes as well as inclusions.

Not only the Laplace problems, but also the Helmholtz problems with circular boundaries are our focus to solve by using the null-field integral equation approach in conjunction with degenerate kernels, Fourier series, vector decomposition and the adaptive observer frame. Half-plane problems with cavities, alluvial valleys, and inclusions subject to the SH-wave problems are solved by using our approach since they both satisfy the Helmholtz equation. Simple cases were solved in many studies, *i.e.* half-plane problem with cavities or the inclusions [50-56, 58-62, 79-81, 85-93, 95-98, 103, 104]. In order to verify the present formulation, problems containing multiple circular boundaries, cavities, alluvial valleys, canyons, and inclusions are tested in this thesis. According to the degenerate kernels, null-field integral formulation and Fourier series for problems with circular boundaries, a linear algebraic system is constructed by matching the interface conditions at the collocation points. The displacement and slope for the problems with circular boundaries can be obtained by using the boundary integral equations for the domain point. In the polar

coordinate system, the calculation of potential gradients in the normal and tangential directions for the stress components must be specially taken care. It is interesting that basin geography subject to the incident wave can also be solved by using the present method. Alluvial valley subject to the incident wave is decomposed into two parts, incident plane wave field and radiation field. The radiation boundary condition is the minus quantity of incident wave function for matching the boundary condition of total wave for cavity. The effect of harder and softer inclusions on the site response subject to the incident wave is discussed. Also, half-plane problems with a semi-circular canyon subject to the SH wave is solved and it can be seen as a limiting case of semi-circular alluvial problems by setting zero shear modulus. Previous results, *e.g.* the Trifunac's [80] analytical solution and other numerical data, are compared with. Finally, several examples including two inclusions, successive canyons and alluvial valleys, are presented to show the validity of the present method and some conclusions are made. The analytical solution of the Green's function [41] of annular case can also be derived using our approach. Since analytical solutions are not available for eccentric case, our semi-analytical method may provide a datum for other researcher's references.

1.2 Organization of the thesis

In this thesis, the null-field integral equations in conjunction with degenerate kernels and Fourier series are utilized to solve the torsion, bending, radiation and scattering problems with circular boundaries. We coined it the null-field integral equation approach. The comparison of conventional BEM and the present method is shown in Table 1-1. The organization of each chapter is summarized below.

In the chapter 2, we derive the unified formulation of null-field integral equation approach for boundary value problems. The degenerate kernels and Fourier series expansions are adopted in the null-field integral equation to solve boundary value problems with circular boundaries. The present method is treated as a "semi-analytical" solution since error only attributes to the truncation of Fourier series. Four gains of well-posed model, singularity free, boundary-layer effect free and

exponential convergence are our goals to achieve.

In the chapter 3, the application to the Laplace equation of torsion and bending problems with circular holes are considered. We emphasize on determining the torsional rigidity for torsion problems and the stress concentration for bending problems. For the torsion problem, the torsional rigidity is compared with the Caulk's [14] and Ling's data [57]. The result of torsion rigidity is improved over Ling's data. On the other hand, the discrepancy between Bird and Steele [6,8] and Naghdi [68] results in the bending problem is examined by using the present approach. It is found that the present method is more versatile to calculate the bending problem with arbitrary number of holes.

In the chapter 4, we focus on the applications to the exterior radiation and scattering problems with circular boundaries. Not only the cavities but also inclusions are considered. The stress concentration factor of the cavity under the half-plane is investigated. Besides, the surface amplitudes are considered for inclusion problems. Image concept and technique of decomposition are utilized for half-plane problems. Numerical examples were given to test our programs. The validity of the semi-analytical method is verified.

In the chapter 5, null-field approach is employed to derive the Green's function for annular problems subject to homogeneous Dirichlet boundary conditions. The kernel function and boundary density are expanded by using the degenerate kernel and Fourier series, respectively. A series-form Green's function is derived and plotted. The Poisson integral formula is extended to an annular case from a circle in the text book. Finally, we draw out some conclusions item by item and reveal some further topics in the chapter 6.

Chapter 2 Null-field integral equation formulation

Summary

In the thesis, the degenerate kernels and Fourier series expansions are adopted in the null-field integral equation to solve boundary value problems with circular boundaries. Bending problems of a circular beam with circular holes as well as the SH-wave impinging on the circular inclusions were studied. The main gain of using degenerate kernels in integral equations is free of calculating the principal values for singular integrals. An adaptive observer system is addressed to fully employ the property of degenerate kernels for circular boundaries in the polar coordinate. After moving the null-field point to the boundary and matching the boundary conditions, a linear algebraic system is obtained without boundary discretization. The unknown coefficients in the algebraic system can be easily determined. The present method is treated as a “semi-analytical” solution since error only attributes to the truncation of Fourier series. Three gains of singularity free, boundary-layer effect free and exponential convergence are achieved. It is more friendly for readers to understand in mathematics and to compute in numerical aspect. The Laplace problem of torsion and bending and Helmholtz problem of alluvial and inclusion subject to the incident SH-wave are studied in the following chapters. Extension to multiple alluvial and inclusions subject to SH-wave is also done. In this chapter, we focus on introducing the formulation of null-field integer equation in conjunction with degenerate kernels and Fourier series.

2.1 Dual boundary integral formulation for domain point

Consider the problem with N randomly distributed circular cavities and/or inclusions bounded in the domain Ω and enclosed with the boundaries, B_k ($k = 0, 1, 2, \dots, N$) as shown in Figure 2-1. We define

$$B = \bigcup_{k=0}^N B_k . \quad (2-1)$$

Suppose the materials of matrix and inclusions are elastic, isotropic and homogenous. Based on the mathematical physics, many engineering problems can be described by the equation as shown below:

$$\mathbb{L}\{u(x)\} = 0, \quad x \in \Omega, \quad (2-2)$$

where $u(x)$ is the potential function, Ω is the domain of interest and \mathbb{L} is the operator of Laplace or Helmholtz and problem as shown below

$$\mathbb{L} = \begin{cases} \nabla^2 & \text{:Laplace problem} \\ \nabla^2 + k^2 & \text{:Helmholtz problem} \end{cases}, \quad (2-2)$$

Based on the dual boundary integral formulation for the domain point can be derived from the third Green's identity [101], we have

$$2\pi u(x) = \int_B T(s, x) u(s) dB(s) - \int_B U(s, x) t(s) dB(s), \quad x \in \Omega, \quad (2-3)$$

$$2\pi \frac{\partial u(x)}{\partial n_x} = \int_B M(s, x) u(s) dB(s) - \int_B L(s, x) t(s) dB(s), \quad x \in \Omega, \quad (2-4)$$

where s and x are the source and field points, respectively, B is the boundary, n_x denotes the outward normal vector at field point x and the kernel function $U(x, s)$ is the fundamental solution which satisfies

$$\mathbb{L}\{U(x, s)\} = 2\pi\delta(x-s), \quad (2-5)$$

in which $\delta(x-s)$ denotes the Dirac-delta function. The other kernel functions, $T(s, x)$, $L(s, x)$ and $M(s, x)$, are defined by

$$T(s, x) \equiv \frac{\partial U(s, x)}{\partial n_s}, \quad L(s, x) \equiv \frac{\partial U(s, x)}{\partial n_x}, \quad M(s, x) \equiv \frac{\partial^2 U(s, x)}{\partial n_s \partial n_x}, \quad (2-6)$$

where n_s is the outward normal vector at the source point s . The null-field integral equations can be derived by collocating x outside the domain ($x \in \Omega^c$) as follows:

$$0 = \int_B T(s, x) u(s) dB(s) - \int_B U(s, x) t(s) dB(s), \quad x \in \Omega^c, \quad (2-9)$$

$$0 = \int_B M(s, x) u(s) dB(s) - \int_B L(s, x) t(s) dB(s), \quad x \in \Omega^c, \quad (2-10)$$

where Ω^c is the complementary domain. Note that the null-field integral equations are not singular since s and x never coincide. No matter the problem of Laplace or Helmholtz is employed to solve the problem. For simplicity, Eq. (2-9) is used to

analyze to solve the problem in the thesis although Eq. (2-10) also plays an important role in computational mechanics. In the real implementation, the collocation point in the null-field integral equation is located exactly on the boundary from Ω^c such that the kernel functions can be expressed in term of interior and exterior appropriate form of degenerate kernels. All the singular integrals disappear in the present formulation since that the potential across the boundary can be explicitly determined in both sides by using degenerate kernels.

2.2 Expansions of fundamental solution and boundary density

2.2.1 Degenerate kernels for the fundamental solution

By employing the separation technique for source point and field point, the kernel function $U(s, x)$ can be expanded in terms of degenerate kernel in a series form as shown below:

$$U(s, x) = \begin{cases} U^i(s, x) = \sum_{j=0}^{\infty} A_j(s) B_j(x), & |x| < |s| \\ U^e(s, x) = \sum_{j=0}^{\infty} A_j(x) B_j(s), & |x| > |s| \end{cases}, \quad (2-11)$$

where the superscripts “ i ” and “ e ” denote the interior and exterior cases of $U(s, x)$ kernel depending on the geometry as shown in Figure 2-2 for one, two and three dimensional cases. The other kernels in the boundary integral equations can be obtained by utilizing the operators of Eq. (2-6) with respect to the $U(s, x)$ kernel. Then, the kernel function with the superscript “ i ” is chosen while the field point is inside the circular region; otherwise, the kernels with the superscript “ e ” is chosen. The details of the degenerate kernels are shown in Section 3.2 and 4.2 for Laplace and Helmholtz equations, respectively.

2.2.2 Fourier series expansion for the boundary density

In order to fully describe the circular boundary, the present method employs the Fourier series to approximate the boundary potential and the normal derivative as

shown in

$$u(s) = a_0 + \sum_{n=1}^{\infty} (a_n \cos n\theta + b_n \sin n\theta), s \in B \quad (2-12)$$

$$t(s) = p_0 + \sum_{n=1}^{\infty} (p_n \cos n\theta + q_n \sin n\theta), s \in B \quad (2-13)$$

where a_0 , a_n , b_n , p_0 , p_n and q_n are the Fourier coefficients and θ is the polar angle which is equally discretized. In the real computation, the integrations can be easily calculated by employing the orthogonal property of Fourier series, and only the finite L terms are used in the summation. The present method is treated as a “semi-analytical” solution since error only attributes to the truncation of Fourier series.

2.3 Adaptive observer system

Consider a BVP with circular boundaries of arbitrary locations as shown in Figure 2-1. The rule of objectivity is obeyed since the boundary integral equations are frame indifferent. An adaptive observer system is addressed to fully employ the property of degenerate kernels for circular boundaries in the polar coordinate as shown in Figures 2-3 (a) and (b). For the integration, the origin of the observer system can be adaptively located on the center of the corresponding boundary contour. The dummy variable in the circular boundary integration is the angle (θ) instead of radial coordinate (R). By using the adaptive system, all the integrations can be easy to calculate.

2.4 Vector decomposition technique for the potential gradient in the hypersingular equation

The hypersingular integral equation in Eq. (2-4) is defined as the normal derivative of potential for the domain points (x), special treatment is considered here. For the stress concentration problem, potential gradient is utilized to calculate. Consider the nonconcentric case as shown in Figure 2-4, the true normal direction ($\bar{1}$) with respect to the collocation point x on the B_i boundary can be superimposed by using the

radial direction ($\bar{3}$) and angular direction ($\bar{4}$) on the B_j boundary. According to the concept of decomposition technique, the degenerate kernels for the higher-order singular equation as Eq. (2-10) are changed as :

$$L(s, x) = \begin{cases} L^i(R, \theta; \rho, \phi) = \frac{\partial U^i(R, \theta; \rho, \phi)}{\partial \rho} \cos(\zeta - \xi) \\ \quad + \frac{1}{\rho} \frac{\partial U^i(R, \theta; \rho, \phi)}{\partial \phi} \cos(\frac{\pi}{2} - \zeta + \xi), \quad R > \rho \\ L^e(R, \theta; \rho, \phi) = \frac{\partial U^e(R, \theta; \rho, \phi)}{\partial \rho} \cos(\zeta - \xi) \\ \quad + \frac{1}{\rho} \frac{\partial U^e(R, \theta; \rho, \phi)}{\partial \phi} \cos(\frac{\pi}{2} - \zeta + \xi), \quad \rho > R \end{cases} \quad (2-14)$$

$$M(s, x) = \begin{cases} M^i(R, \theta; \rho, \phi) = \frac{\partial T^i(R, \theta; \rho, \phi)}{\partial \rho} \cos(\zeta - \xi) \\ \quad + \frac{1}{\rho} \frac{\partial T^i(R, \theta; \rho, \phi)}{\partial \phi} \cos(\frac{\pi}{2} - \zeta + \xi), \quad R > \rho \\ M^e(R, \theta; \rho, \phi) = \frac{\partial T^e(R, \theta; \rho, \phi)}{\partial \rho} \cos(\zeta - \xi) \\ \quad + \frac{1}{\rho} \frac{\partial T^e(R, \theta; \rho, \phi)}{\partial \phi} \cos(\frac{\pi}{2} - \zeta + \xi), \quad \rho > R \end{cases} \quad (2-15)$$

where ζ and ξ are shown in Figure 2-4. For the special annular problem, the decomposition technique is free of special treatment.

2.5 Linear algebraic equation

In order to calculate the Fourier coefficients, $2L+1$ boundary nodes are needed. By moving the null-field point to the j th circular boundary for Eq. (2-9) and (2-10), we have

$$0 = \sum_{j=0}^N \int_{B_j} T(s, x) u(s) dB(s) - \sum_{j=0}^N \int_{B_j} U(s, x) t(s) dB(s), \quad x \in \mathcal{U}, \quad (2-16)$$

$$0 = \sum_{j=0}^N \int_{B_j} M(s, x) u(s) dB(s) - \sum_{j=0}^N \int_{B_j} L(s, x) t(s) dB(s), \quad x \in \mathcal{U}^c. \quad (2-17)$$

It is noted that the integration path is anticlockwise for the outer circle. Otherwise, it is clockwise. For the B_j integral of the circular boundary, the kernel of $U(s, x)$ is expressed in terms of degenerate kernel of Eq. (2-11), and $T(s, x)$, $L(s, x)$ and

$M(s, x)$ are respectively obtained by applying the differential operators defined in Eq. (2-6). The boundary densities $u(s)$ and $t(s)$ are substituted by using the Fourier series of Eqs. (2-12) and (2-13), respectively. In the B_j integration, we set the origin of the observer system to collocate at the center c_j to fully utilize the degenerate kernel and Fourier series. By moving the null-field point to B_j , a linear algebraic system is obtained

$$[\mathbf{U}]\{\mathbf{t}\} = [\mathbf{T}]\{\mathbf{u}\}, \quad (2-18)$$

$[\mathbf{U}]$ and $[\mathbf{T}]$ are the influence matrices with a dimension of $(N+1) \times (2L+1)$ by $(N+1) \times (2L+1)$, $\{\mathbf{u}\}$ and $\{\mathbf{t}\}$ denote the column vectors of Fourier coefficients with a dimension of $(N+1) \times (2L+1)$ by 1 in which those can be defined as follows:

$$[\mathbf{U}] = \begin{bmatrix} \mathbf{U}_{00} & \mathbf{U}_{01} & \cdots & \mathbf{U}_{0N} \\ \mathbf{U}_{10} & \mathbf{U}_{11} & \cdots & \mathbf{U}_{1N} \\ \vdots & \vdots & \ddots & \vdots \\ \mathbf{U}_{N0} & \mathbf{U}_{N1} & \cdots & \mathbf{U}_{NN} \end{bmatrix}, \quad [\mathbf{T}] = \begin{bmatrix} \mathbf{T}_{00} & \mathbf{T}_{01} & \cdots & \mathbf{T}_{0N} \\ \mathbf{T}_{10} & \mathbf{T}_{11} & \cdots & \mathbf{T}_{1N} \\ \vdots & \vdots & \ddots & \vdots \\ \mathbf{T}_{N0} & \mathbf{T}_{N1} & \cdots & \mathbf{T}_{NN} \end{bmatrix} \quad (2-19)$$

$$\{\mathbf{u}\} = \begin{bmatrix} \mathbf{u}_0 \\ \mathbf{u}_1 \\ \mathbf{u}_2 \\ \vdots \\ \mathbf{u}_N \end{bmatrix}, \quad \{\mathbf{t}\} = \begin{bmatrix} \mathbf{t}_0 \\ \mathbf{t}_1 \\ \mathbf{t}_2 \\ \vdots \\ \mathbf{t}_N \end{bmatrix} \quad (2-20)$$

where the vectors $\{\mathbf{u}\}$ and $\{\mathbf{t}\}$ are the Fourier coefficients and the first index “ j ” ($j = 0, 1, 2, \dots, N$) in $[\mathbf{U}_{jk}]$ and $[\mathbf{T}_{jk}]$ denotes the j th circle where the collocation point is located and the second index “ k ” ($k = 0, 1, 2, \dots, N$) denotes the k th circle with boundary data $\{\mathbf{u}_k\}$ and $\{\mathbf{t}_k\}$, L indicates the truncated terms of Fourier series. The coefficient matrix of the linear algebraic system is partitioned into blocks, and each off-diagonal block corresponds to the influence matrices between two different circular boundaries. The diagonal blocks are the influence matrices due to themselves in each individual circle. After uniformly collocating the points along the k th circular boundary, the submatrix can be written as

$$[\mathbf{U}_{jk}] = \begin{bmatrix} U_{jk}^{0c}(\phi_1) & U_{jk}^{1c}(\phi_1) & U_{jk}^{1s}(\phi_1) & \cdots & U_{jk}^{Lc}(\phi_1) & U_{jk}^{Ls}(\phi_1) \\ U_{jk}^{0c}(\phi_2) & U_{jk}^{1c}(\phi_2) & U_{jk}^{1s}(\phi_2) & \cdots & U_{jk}^{Lc}(\phi_2) & U_{jk}^{Ls}(\phi_2) \\ U_{jk}^{0c}(\phi_3) & U_{jk}^{1c}(\phi_3) & U_{jk}^{1s}(\phi_3) & \cdots & U_{jk}^{Mc}(\phi_3) & U_{jk}^{Ls}(\phi_3) \\ \vdots & \vdots & \vdots & \ddots & \vdots & \vdots \\ U_{jk}^{0c}(\phi_{2L}) & U_{jk}^{1c}(\phi_{2L}) & U_{jk}^{1s}(\phi_{2L}) & \cdots & U_{jk}^{Lc}(\phi_{2L}) & U_{jk}^{Ls}(\phi_{2L}) \\ U_{jk}^{0c}(\phi_{2L+1}) & U_{jk}^{1c}(\phi_{2L+1}) & U_{jk}^{1s}(\phi_{2L+1}) & \cdots & U_{jk}^{Lc}(\phi_{2L+1}) & U_{jk}^{Ls}(\phi_{2L+1}) \end{bmatrix}, \quad (2-21)$$

$$[\mathbf{T}_{jk}] = \begin{bmatrix} T_{jk}^{0c}(\phi_1) & T_{jk}^{1c}(\phi_1) & T_{jk}^{1s}(\phi_1) & \cdots & T_{jk}^{Lc}(\phi_1) & T_{jk}^{Ls}(\phi_1) \\ T_{jk}^{0c}(\phi_2) & T_{jk}^{1c}(\phi_2) & T_{jk}^{1s}(\phi_2) & \cdots & T_{jk}^{Lc}(\phi_2) & T_{jk}^{Ls}(\phi_2) \\ T_{jk}^{0c}(\phi_3) & T_{jk}^{1c}(\phi_3) & T_{jk}^{1s}(\phi_3) & \cdots & T_{jk}^{Lc}(\phi_3) & T_{jk}^{Ls}(\phi_3) \\ \vdots & \vdots & \vdots & \ddots & \vdots & \vdots \\ T_{jk}^{0c}(\phi_{2L}) & T_{jk}^{1c}(\phi_{2L}) & T_{jk}^{1s}(\phi_{2L}) & \cdots & T_{jk}^{Lc}(\phi_{2L}) & T_{jk}^{Ls}(\phi_{2L}) \\ T_{jk}^{0c}(\phi_{2L+1}) & T_{jk}^{1c}(\phi_{2L+1}) & T_{jk}^{1s}(\phi_{2L+1}) & \cdots & T_{jk}^{Lc}(\phi_{2L+1}) & T_{jk}^{Ls}(\phi_{2L+1}) \end{bmatrix}, \quad (2-22)$$

where ϕ_j , $j=1,2,\dots,2L+1$, are the angles of collocation along the circular boundary. Although both the matrices in Eqs. (2-21) and (2-22) are not sparse, it is found that the higher order harmonics is considered, the lower influence coefficients in numerical experiments is obtained. It is noted that the superscript “0s” in Eqs. (2-21) and (2-22) disappears since $\sin(0 \cdot \theta) = 0$. The element of $[\mathbf{U}_{jk}]$ and $[\mathbf{T}_{jk}]$ are defined respectively as

$$U_{jk}^{nc}(\phi_m) = \int_{B_k} U(s_k, x_m) \cos(n\theta_k) R_k d\theta_k, \quad n=0,1,2,\dots,L, \quad m=1,2,\dots,2L+1, \quad (2-23)$$

$$U_{jk}^{ns}(\phi_m) = \int_{B_k} U(s_k, x_m) \sin(n\theta_k) R_k d\theta_k, \quad n=1,2,\dots,L, \quad m=1,2,\dots,2L+1, \quad (2-24)$$

$$T_{jk}^{ns}(\phi_m) = \int_{B_k} T(s_k, x_m) \cos(n\theta_k) R_k d\theta_k, \quad n=0,1,2,\dots,L, \quad m=1,2,\dots,2L+1, \quad (2-25)$$

$$T_{jk}^{ns}(\phi_m) = \int_{B_k} T(s_k, x_m) \sin(n\theta_k) R_k d\theta_k, \quad n=1,2,\dots,L, \quad m=1,2,\dots,2L+1, \quad (2-26)$$

where k is no sum, $s_k = (R_k, \theta_k)$, and ϕ_m is the polar angle of the collocation point x_m . The analytical evaluation of the integrals for each element in the influence matrix is listed in the Appendixes and they are all non-singular. Besides, the limiting case to the boundary is also addressed. The continuous and jump behavior across the boundary is also described. The direction of contour integration should be taken care, *i.e.*, counterclockwise and clockwise directions are for the interior and exterior problems, respectively. By rearranging the known and unknown sets, the Fourier coefficients can be obtained.

2.6 Matching of interface conditions for problems of cavities and inclusions

Cavity problems

In order to match the traction free condition on the cavity boundary after decomposition of the original problem as shown below

$$0 = t_i^M = t^f + t^M, \quad (2-27)$$

where the “ t_i^M ” denotes the total field of matrix. The superscript “ f ” represents the external force where $t^f = t^i$ for the full-plane plane and $t^f = t^{i+r}$ for the half-plane plane. The superscript “ i ” and “ r ” are the incident and reflected waves and “ t^M ” denotes the radiation problem of matrix and needed to be solved. All the relations are shown in Appendix , and Eq. (2-18) can be rewritten as

$$[\mathbf{U}]\{-\mathbf{t}^{i+r}\} = [\mathbf{T}]\{\mathbf{u}^M\}, \quad (2-28)$$

Only the Fourier coefficients of boundary density $\{\mathbf{u}^M\}$ are unknown. By collocating $2L+1$ null-field points on each boundary, all the coefficients can be obtained. After obtaining the unknown Fourier coefficients, the field displacement can be obtain by employing Eq. (2-3).

Inclusion problems

According to the linear algebraic system, the two systems of matrix and inclusion yield

$$[\mathbf{U}^M]\{\mathbf{t}^M\} = [\mathbf{T}^M]\{\mathbf{u}^M\}. \quad (2-29)$$

$$[\mathbf{U}^I]\{\mathbf{t}^I\} = [\mathbf{T}^I]\{\mathbf{u}^I\} \quad (2-30)$$

where the superscripts “ M ” and “ I ” denote the systems of matrix and inclusion, respectively. By the image concept and the decomposition of superposition as the Section 4.3, the Eq. (2-29) can be rewritten as

$$[\mathbf{U}^M]\{\mathbf{t}_i^M - \mathbf{t}^{i+r}\} = [\mathbf{T}^M]\{\mathbf{u}_i^M - \mathbf{u}^{i+r}\}. \quad (2-31)$$

where the “ $\{\mathbf{t}_i^M\}$ ” denotes the “total” displacement field of “matrix” as shown in Appendix , After decomposition of the original problem, we have the two constraints of the continuity of displacement and equilibrium of traction along the

j th interface (B_j). We will employ the two constrains into the formulation as shown below:

$$\{\mathbf{u}_t^M\} = \{\mathbf{u}^I\} \quad \text{on } B_k, \quad (2-32)$$

$$[\boldsymbol{\mu}^M]\{\mathbf{t}_t^M\} = -[\boldsymbol{\mu}^I]\{\mathbf{t}^I\} \quad \text{on } B_k, \quad (2-33)$$

where $[\boldsymbol{\mu}^M]$ and $[\boldsymbol{\mu}^I]$ can be defined as follows:

$$[\boldsymbol{\mu}^M] = \begin{bmatrix} \mu^M & 0 & \cdots & 0 \\ 0 & \mu^M & \cdots & 0 \\ \vdots & \vdots & \ddots & \vdots \\ 0 & 0 & \cdots & \mu^M \end{bmatrix}, \quad [\boldsymbol{\mu}^I] = \begin{bmatrix} \mu^I & 0 & \cdots & 0 \\ 0 & \mu^I & \cdots & 0 \\ \vdots & \vdots & \ddots & \vdots \\ 0 & 0 & \cdots & \mu^I \end{bmatrix} \quad (2-34)$$

where μ^M and μ^I denote the shear modulus of the matrix and the k th inclusion, respectively. By assembling the matrices in Eqs. (2-30), (2-31), (2-32) and (2-33), we have

$$\begin{bmatrix} \mathbf{T}^M & -\mathbf{U}^M & \mathbf{0} & \mathbf{0} \\ \mathbf{0} & \mathbf{0} & \mathbf{T}^I & -\mathbf{U}^I \\ \mathbf{I} & \mathbf{0} & -\mathbf{I} & \mathbf{0} \\ \mathbf{0} & \boldsymbol{\mu}^M & \mathbf{0} & \boldsymbol{\mu}^I \end{bmatrix} \begin{bmatrix} \mathbf{u}_t^M \\ \mathbf{t}_t^M \\ \mathbf{u}^I \\ \mathbf{t}^I \end{bmatrix} = \begin{bmatrix} \mathbf{u}(\mathbf{x})^{i+r} \\ \mathbf{0} \\ \mathbf{0} \\ \mathbf{0} \end{bmatrix}, \quad (2-35)$$

where $[\mathbf{I}]$ is the identity matrix, and $\{\mathbf{u}(\mathbf{x})^{i+r}\}$ as shown below

$$\{\mathbf{u}(\mathbf{x})^{i+r}\} = \langle \mathbf{T}^M \quad -\mathbf{U}^M \rangle \begin{bmatrix} \mathbf{u}^i + \mathbf{u}^r \\ \mathbf{t}^i + \mathbf{t}^r \end{bmatrix}. \quad (2-36)$$

After obtaining the unknown Fourier coefficients, the origin of observer system is set to c_j in the B_j integration as shown in Figure 2-3 (b) to obtain the potential by employing Eq. (2-3). The flow chart of the present method is shown in Figure 2-5.

2.7 Concluding remarks

For the BVPs with circular boundaries, we have proposed a systematic null-field BIEM by using the null-field integral equation, degenerate kernels and Fourier series in an adaptive observer system. The method shows great generality and versatility for the problems for Laplace and Helmholtz with multiple circular holes or inclusions of arbitrary radii and positions. Several engineering problems with circular boundaries are solved by using the proposed approach will be elaborated on later in the following chapters.

Chapter 3 Application to Laplace problems

Summary

In this chapter, the application to torsion and bending problems with circular holes are considered. Both problems can be modeled by the Laplace equation. We emphasize on the torsional rigidity for torsion problem and the stress concentration for bending problem. For the torsion problem, the torsional rigidity is compared with the Caulk [14] and Ling's data [57]. On the other hand, the discrepancy between the data of Bird and Steele [8] and Naghdi's [68] results in the bending problem is examined by using the present approach. It is found that the present method is more general for calculating the torsion and bending problems with arbitrary number of holes and various radii and positions than other approach.

3.1 Introduction

The stress concentration around holes of a beam under torsion or bending plays an important role in promoting the design criteria for higher factors of safety. Those problems have been visited in a few investigations based on the Saint-Venant theory [75,78]. For a simple case, an analytical solution may be available. Since the analytical solution for more than two holes may encounter difficulty. In the past, multiply-connected problems have been carried out either by conformal mapping or by special technique approach. Muskhelishvili [67] has formulated the solution of composite torsion bar in the form of integral equation. He solved the problem of a circular bar reinforced by an eccentric inclusion by using conformal mapping. Chen and Weng [34] have also introduced conformal mapping with a Laurent series expansion to analyze the Saint-Venant torsion problem. They concerned with an eccentric bar of different materials with an imperfect interface under torque. Because the conformal mapping is limited to the doubly-connected region, an increasing number of researchers have paid more attentions on special techniques. However, the extension of above special techniques to multiple circular holes may encounter

difficulty. It is not trivial to develop a systematic method for solving the torsion problems with several holes. Several numerical approaches have been employed, *e.g.* complex variable boundary element method (CVBEM) by Chou [35] and Ang and Kang [3]. The CVBEM was primarily introduced by Hromadka and Lai [45] for solving the Laplace problems in an infinite domain. In 1997, Chou extended the work of Hromadka to problems with the multiply-connected domain. Recently, Ang and Kang [3] developed a general formulation for solving the second-order elliptic partial differential equation for a multiply-connected region in a different version of CVBEM. The Cauchy integral formulae are offered to solve the boundary value problem. By introducing the CVBEM, Chou [35] and Ang and Kang [3] have revisited the anti-plane problems with two circular holes whose centers lie on the x axis investigated by Honein *et al.* [44]. In 1991, Naghdi [68] employed a special class of basic function, which is a Saint-Venant flexure function suitable for the problem of the bending of a circular cylinder with $4N$ ($N = 1, 2, 3, \dots$) circular holes in the axial direction. Bird and Steele [8] used a Fourier series procedure to revisit the antiplane problems in the Honein's paper [44]. Also, they solved the bending problems which were solved by Naghdi [68]. According to the literature review, it is observed that exact solutions for boundary value problems are only limited for simple cases. Although Naghdi [68] has proposed a solution for bending problems with holes, it is limited for $4N$ ($N = 1, 2, 3, \dots$) holes. Therefore, proposing a systematic approach for solving BVP with various numbers of circular boundaries and arbitrary positions and radii is our goal in this chapter.

Following the success of anti-plane problems with circular holes [27], the null-field integral equation is utilized to solve both of the Saint-Venant torsion and bending problems with circular holes. The mathematical formulation is derived by using degenerate kernels for fundamental solutions and Fourier series for boundary densities. Then, it reduces to a linear algebraic equation by using collocation approach. Mogilevskaya and Crouch [65] have used the Galerkin method instead of collocation approach. Our approach can be extended to the Galerkin formulation only for the circular and annular cases. However, it may encounter difficulty for the eccentric example. Two requirements are needed: degenerate kernel expansion must be

available and distinction of interior and exterior expression must be separated. Therefore, the collocation angle of ϕ is not in the range 0 to 2π in our adaptive observer system. This is the reason why we can not formulate in terms of Galerkin formulation using orthogonal properties twice. Free of worrying about how to choose the collocation points, uniform collocation along the circular boundary yields a well-posed matrix. After determining the unknown Fourier coefficients, series solution for the torsion and bending functions are obtained. For the torsion problem, torsional rigidity is our main concern. For the bending problem, the location of maximum stress concentration factor (SCF) and the boundary-layer effect are addressed. Numerical examples are given to show the validity and efficiency of our approach.

3.2 Degenerate kernels of BIE formulation for Laplace problems

Both torsion and bending problems can be modeled by using the Laplace equation,

$$\nabla^2 u(x) = 0, \quad x \in \Omega \quad (3-1)$$

where ∇^2 and Ω are the Laplacian operator and the domain of interest, respectively. Based on the dual boundary integral formulation of the domain point [27], we have

$$2\pi u(x) = \int_B T(s, x) u(s) dB(s) - \int_B U(s, x) t(s) dB(s), \quad x \in \Omega, \quad (3-2)$$

$$2\pi \frac{\partial u(x)}{\partial n_x} = \int_B M(s, x) u(s) dB(s) - \int_B L(s, x) t(s) dB(s), \quad x \in \Omega, \quad (3-3)$$

where s and x are the source and field points, respectively, $t(s)$ is the directional derivative of $u(s)$ along the outer normal direction at s , and n_x is the outward normal vector at the field point x . The four kernel functions, $U(s, x)$, $T(s, x)$, $L(s, x)$ and $M(s, x)$, will be elaborated on later by using the degenerate kernel expansion. The kernel function, $U(s, x)$, is the fundamental solution which satisfies

$$\nabla^2 U(x, s) = 2\pi \delta(x - s), \quad (3-4)$$

where $\delta(x - s)$ denotes the Dirac-delta function. Then, we can obtain the fundamental solution as follows

$$U(s, x) = \ln r, \quad (3-5)$$

where r is the distance between s and x ($r \equiv |x-s|$). The other kernel functions, $T(s, x)$, $L(s, x)$ and $M(s, x)$, are defined by

$$T(s, x) \equiv \frac{\partial U(s, x)}{\partial n_s}, \quad L(s, x) \equiv \frac{\partial U(s, x)}{\partial n_x}, \quad M(s, x) \equiv \frac{\partial^2 U(s, x)}{\partial n_s \partial n_x}, \quad (3-6)$$

where n_s denotes the outward normal vector at the source point s . Comparison of formulation between the present method and conventional BEM is shown in Table 3-1. In the present method, we adopt the mathematical tools, degenerate kernels and Fourier series, for the purpose of analytical study. The combination of degenerate kernels and Fourier series plays the major role in handling problems with circular boundaries.

Based on the separable property, the kernel function $U(s, x)$ can be expanded into separable form by dividing the source point ($s = (R, \theta)$) and field point ($x = (\rho, \phi)$) in the polar coordinate

$$U(s, x) = \begin{cases} U^i(s, x) = \ln R - \sum_{m=1}^{\infty} \frac{1}{m} \left(\frac{\rho}{R}\right)^m \cos m(\theta - \phi), & R \geq \rho \\ U^e(s, x) = \ln \rho - \sum_{m=1}^{\infty} \frac{1}{m} \left(\frac{R}{\rho}\right)^m \cos m(\theta - \phi), & \rho > R \end{cases}, \quad (3-7)$$

where the superscripts “ i ” and “ e ” denote the interior ($R > \rho$) and exterior ($\rho > R$) cases, respectively. It is found that the leading term and the numerator term contain the larger argument such that log singularity and series convergence can be confirmed. After taking the normal derivative ($\partial/\partial R$) with respect to Eq. (3-7), the $T(s, x)$ kernel function yields

$$T(s, x) = \begin{cases} T^i(s, x) = \frac{1}{R} + \sum_{m=1}^{\infty} \left(\frac{\rho^m}{R^{m+1}}\right) \cos m(\theta - \phi), & R > \rho \\ T^e(s, x) = -\sum_{m=1}^{\infty} \left(\frac{R^{m-1}}{\rho^m}\right) \cos m(\theta - \phi), & \rho > R \end{cases}, \quad (3-8)$$

and the higher-order kernel functions, $L(s, x)$ and $M(s, x)$, are shown below:

$$L(s, x) = \begin{cases} L^i(s, x) = -\sum_{m=1}^{\infty} \left(\frac{\rho^{m-1}}{R^m}\right) \cos m(\theta - \phi), & R > \rho \\ L^e(s, x) = \frac{1}{\rho} + \sum_{m=1}^{\infty} \left(\frac{R^m}{\rho^{m+1}}\right) \cos m(\theta - \phi), & \rho > R \end{cases}, \quad (3-9)$$

$$M(s, x) = \begin{cases} M^i(s, x) = \sum_{m=1}^{\infty} \left(\frac{m\rho^{m-1}}{R^{m+1}} \right) \cos m(\theta - \phi), & R \geq \rho \\ M^e(s, x) = \sum_{m=1}^{\infty} \left(\frac{mR^{m-1}}{\rho^{m+1}} \right) \cos m(\theta - \phi), & \rho > R \end{cases}. \quad (3-10)$$

Since the potentials resulted from $T(s, x)$ and $L(s, x)$ are discontinuous cross the boundary, the potentials of $T(s, x)$ and $L(s, x)$ for $R \rightarrow \rho^+$ and $R \rightarrow \rho^-$ are different. This is the reason why $R = \rho$ is not included in the expression for the degenerate kernels of $T(s, x)$ and $L(s, x)$ in Eqs. (3-8) and (3-9). The analytical evaluation of the integrals for each element in the influence matrix is listed in the Appendix and they are all non-singular. Besides, the limiting case to the boundary is also addressed. The continuous and jump behavior across the boundary is also described. After using the Wronskian property of two bases for $T(s, x)$ (R^m and R^{-m})

$$W(R^m, R^{-m}) = 2mR, \quad (3-11)$$

the jump behavior is captured by

$$\int_0^{2\pi} (T^i(s, x) - T^e(s, x)) \cos(m\theta) R d\theta = 2\pi \cos(m\theta), \quad x \in B, \quad (3-12)$$

$$\int_0^{2\pi} (T^i(s, x) - T^e(s, x)) \sin(m\theta) R d\theta = 2\pi \sin(m\theta), \quad x \in B. \quad (3-13)$$

Jump behavior is well captured by Wronskian in similar way of two bases for 1-D rod case.

3.3 Torsion problem for a bar

3.3.1 Problem statements

What is given in Figure 3-1 is a circular bar weakened by N circular holes placed on a concentric ring of radius b . The radii of the outer circle and the inner holes are R and a , respectively. The circular bar twisted by couples applied at the ends is taken into consideration. Following the theory of Saint-Venant torsion [75,78,99], we assume the displacement field to be

$$u = -\alpha yz, \quad v = \alpha xz, \quad w = \alpha\varphi(x, y), \quad (3-14)$$

where α is the angle of twist per unit length along the z direction and φ is the warping function. According to the displacement field in Eq. (3-14), the strain components are

$$\varepsilon_x = \varepsilon_y = \varepsilon_z = \gamma_{xy} = 0, \quad (3-15)$$

$$\gamma_{xz} = \frac{\partial w}{\partial x} + \frac{\partial u}{\partial z} = \alpha\left(\frac{\partial \varphi}{\partial x} - y\right), \quad (3-16)$$

$$\gamma_{yz} = \frac{\partial w}{\partial y} + \frac{\partial v}{\partial z} = \alpha\left(\frac{\partial \varphi}{\partial y} + x\right), \quad (3-17)$$

and their corresponding components of stress are

$$\sigma_x = \sigma_y = \sigma_z = \sigma_{xy} = 0, \quad (3-18)$$

$$\sigma_{xz} = \mu\alpha\left(\frac{\partial \varphi}{\partial x} - y\right), \quad \sigma_{yz} = \mu\alpha\left(\frac{\partial \varphi}{\partial y} + x\right), \quad (3-19)$$

where μ is the shear modulus. There is no distortion in the planes of cross sections since $\varepsilon_x = \varepsilon_y = \varepsilon_z = \gamma_{xy} = 0$. We have the state of pure shear at each point defined by the stress components σ_{xz} and σ_{yz} . The warping function φ must satisfy the equilibrium equation

$$\frac{\partial^2 \varphi}{\partial x^2} + \frac{\partial^2 \varphi}{\partial y^2} = 0 \quad \text{in } \Omega, \quad (3-20)$$

where the body force is neglected and Ω is the domain. Since there are no external forces on the cylindrical surface, we have $t_x = t_y = t_z = 0$. By substituting the normal vector, the only zero t_z becomes

$$t_z = \sigma_{xz}n_x + \sigma_{yz}n_y = 0 \quad \text{on } B. \quad (3-21)$$

where B is the boundary. By substituting (3-11) into (3-13) and rearranging the terms, the boundary condition is

$$\frac{\partial \varphi}{\partial x}n_x + \frac{\partial \varphi}{\partial y}n_y = yn_x - xn_y = \nabla \varphi \cdot \mathbf{n} = \frac{\partial \varphi}{\partial \mathbf{n}} \quad \text{on } B, \quad (3-22)$$

In Figure 3-1, we introduce the expressions for the position vector (x_k, y_k) of the boundary point on the k th circular hole

$$x_k = a \cos \theta_k + b \cos\left(\frac{2\pi k}{N}\right), \quad k = 1, 2, \dots, N, \quad 0 < \theta_k < 2\pi, \quad (3-23)$$

$$y_k = a \sin \theta_k + b \sin\left(\frac{2\pi k}{N}\right), \quad k = 1, 2, \dots, N, \quad 0 < \theta_k < 2\pi, \quad (3-24)$$

and the unit outward normal vector $\mathbf{n} = (n_x, n_y) = (-\cos \theta, -\sin \theta)$ for the inner

circular boundaries, we have

$$\frac{\partial \varphi}{\partial \mathbf{n}} = b \cos\left(\frac{2\pi k}{N}\right) \sin \theta_k - b \sin\left(\frac{2\pi k}{N}\right) \cos \theta_k \quad \text{on } B_k, \quad (3-25)$$

where B_k ($k = 1, 2, \dots, N$) is the k th boundary of the inner hole, θ_k is the polar angle with respect to the origin of the k th hole. For the outer boundary, the traction-free condition is specified. Thus, the problem of torsion is reduced to find the warping function φ which satisfies the Laplace equation of Eq. (3-20) and the Neumann boundary conditions of Eq. (3-25) for the inner boundary and zero traction on the outer boundary.

3.3.2 Illustrative examples and discussions

Based on the formulation described in Chapter 2, we demonstrate its validity in solving torsion problems. In this section, we deal with the torsion problems which have been solved by Caulk in 1983 [14]. The torsional rigidity of each example is calculated after obtaining the unknown Fourier coefficients.

Case 1: A circular bar with an eccentric hole

A circular bar of radius R with an eccentric circular holes removed is under torque T at the end. The torsional rigidity G of cross section can be expressed by

$$\frac{G}{\mu} = \int_A (x^2 + y^2) dA - \sum_{k=1}^N \int_{B_k} \varphi \frac{\partial \varphi}{\partial \mathbf{n}} dB_k, \quad (3-26)$$

The exact solution derived by Muskhelishvili [67] is shown below

$$G = \mu_2 (I - I') - \mu_2 \pi l^2 r_1^2 - 2\mu_2 \pi l^2 \rho_1^2 \sum_{k=1}^{\infty} \frac{\alpha^k}{(1 - a^2 \rho_1^2 \alpha^k)^2}, \quad (3-27)$$

where all of notations in Eq. (3-27) follows the reference [67], and they aren't the same with the thesis. Our results are better than those of Caulk obtained by BIE when the hole is closely spaced as shown in Table 3-2.

Case 2: A circular bar with multiple circular holes of equal angles

Consider a circular bar weakened by N circular holes placed on a concentric ring of radius b under torque T at the end. The radii of the outer circle and the inner holes

are R and a , respectively. The boundary curve of kth inner hole is described by using the parametric form of (x_k, y_k) in Eqs. (3-23) and (3-24). What is brought out is the problem subject to zero traction on the outer boundary and Neumann boundary condition defined in Eq. (3-25) on all the inner circles. Twenty-one collocating points are selected on all the circular boundaries in the numerical implementation. Results obtained by using the present method for the problem of two, three and four holes are listed in Table 3-3. After comparison, our results agree well with Caulk's datas obtained by using special BIE formulation.

Case 3: Ling's examples [57]

Table 3-4 shows a comparison of the torsional rigidities of three cases with different geometries of circular holes computed from the present method, BIE formulation [14] and the first-order approach [14]. We have not only calculated the torsional rigidity but also tested the rate of convergence of Fourier terms of the case with seven holes as shown in Figure 3-2. The present solutions show improvement over Ling's results in every case. The large difference in the second example in Table 3-4 may ascribe to the Ling's lengthy calculation in error as pointed out by Caulk [14].

3.4 Bending problem for a cantilever beam

3.4.1 Problem statements

Consider a beam with a circular section weakened by four circular holes placed on a concentric ring of radius b as show in Figure 3-3. The radii of outer circle and inner holes are R and a , respectively. The beam is subject to a shear force Q at the free end, and the boundary conditions of outer circle and inner holes are traction free. Following the theory of Saint-Venant bending [99], we assume the stress to be

$$\sigma_{xx} = \sigma_{yy} = \sigma_{xy} \equiv 0, \quad \sigma_{zz} = -\frac{Q}{I_y} x(l-z), \quad (3-28)$$

where I_y is the moment of inertia of cross section for the y -axis. The other two stress components are assumed as

$$\sigma_{zx} = \alpha\mu \left(\frac{\partial\varphi}{\partial x} + y \right) - \frac{Q}{2(1+\nu)I_y} \left[\frac{\partial\psi}{\partial x} + \frac{1}{2}\nu x^2 + \left(1 - \frac{1}{2}\nu\right)y^2 \right], \quad (3-29)$$

$$\sigma_{zy} = \alpha\mu \left(\frac{\partial\varphi}{\partial y} + x \right) - \frac{Q}{2(1+\nu)I_y} \left[\frac{\partial\psi}{\partial y} + (2+\nu)xy \right], \quad (3-30)$$

where $\varphi(x, y)$ and $\psi(x, y)$ are the warping function and bending function of the beam, respectively, α is the angle of twist per unit length, and μ is the shear modulus. Since the $\varphi(x, y)$ and $\psi(x, y)$ in the Saint-Venant bending problem satisfies the two Laplace equations subject to the Neumann boundary condition, we have:

$$\nabla^2\varphi(x, y) = \frac{\partial^2\varphi}{\partial x^2} + \frac{\partial^2\varphi}{\partial y^2} = 0 \quad \text{in } \Omega, \quad (3-31)$$

$$\frac{\partial\varphi}{\partial n} = y \cos(n, x) - x \cos(n, y), \quad x, y \in B_k, \quad (3-32)$$

and

$$\nabla^2\psi(x, y) = \frac{\partial^2\psi}{\partial x^2} + \frac{\partial^2\psi}{\partial y^2} = 0 \quad \text{in } \Omega, \quad (3-33)$$

$$\frac{\partial\psi}{\partial n} = - \left[\frac{1}{2}\nu x^2 + \left(1 - \frac{1}{2}\nu\right)y^2 \right] \cos(n, x) - (2+\nu)xy \cos(n, y), \quad x, y \in B_k, \quad (3-34)$$

where Ω is the domain of interest, n is the outward normal vector of each boundary, and B_k is the k th circular boundary. In Figure 3-3, we define the position vector (x_k, y_k) of the boundary point on the i th circular boundary as

$$x_k = R_k \sin \theta_k + x_k, \quad k = 0, 1, 2, 3, 4, \quad 0 < \theta_k < 2\pi \quad (3-35)$$

$$y_k = -R_k \cos \theta_k + y_k, \quad k = 0, 1, 2, 3, 4, \quad 0 < \theta_k < 2\pi \quad (3-36)$$

where

$$R_0 = R \quad \text{and} \quad R_j = a, \quad j = 1, 2, 3, 4 \quad (3-37)$$

and θ_k is the polar angle with respect to the origin of the k th hole. The coordinate of (x_k, y_k) is for the center of the k th eccentric circle, and the eccentricity is zero for the outer circle. By substituting Eqs. (3-35) and (3-36) into Eq. (3-24), the boundary condition is specified. To find $\varphi(x, y)$ function for torsion problems was solved in the previous sections. For the simple case of bending only, we can assume constant $\alpha\mu$ and $\psi(x, y)$ to be zero. Following the definition of stress concentration by Naghdi [68], we have

$$Sc = \frac{\sigma_{zx} A}{Q}, \quad (3-38)$$

where A is the cross-section area of the beam. The shear stress σ_{zx} in Eq. (3-38) is

obtained from Eq. (3-29). Thus, the bending problem is reduced to find the bending function $\psi(x, y)$ which satisfies the Laplace equation of Eq. (3-33) and the Neumann boundary condition of Eq. (3-34) on each boundary.

3.4.2 Illustrative examples and discussions

Based on the formulation described in Chapter 2, we demonstrate its validity in solving bending problems. In the section, we deal with the bending problems with $4N$ circular holes which have been solved by Naghdi in 1991 [68] and two holes with various distances which have been solved by Bird and Steele [8].

Case 1: Four circular holes [8,68]

In order to check the validity of the present formulation, the beam problems [68] with four holes symmetrically located with respect to the x and y axis were revisited. All the numerical results were obtained by using ten terms of Fourier series ($L = 10$). We set the value of Poisson's ratio $\nu = 0.3$ and $R = 1$. In Figures 3-4 (a), (b), (d) and (e), the values of the stress concentration Sc along AB and CD (as Figure 3-1) are plotted versus the position $\bar{Y}_1 = 17Y_1/AB$, and $\bar{Y}_2 = 17Y_2/CD$, respectively. Figures 3-4 (c) and (f) show the stress concentration Sc along OT , and the $\xi_1 = 18 \times OT$ for the case of $b = 0.5$, $\bar{\theta} = \pi/4$ and $a = 0.1$. Our numerical results are well compared with those of Naghdi's data [68]. In order to find the stress concentration, we plot the stress around the hole where these numerical results indicate that Sc reaches maximum near point B as shown in Figure 3-5. Figures 3-4 (a) and (b) show the maximum value of Sc occurs at the point B and the point C respectively, where are on the boundaries of inner holes. For the Sc distribution along OT , the maximum value of Sc occurs at the position near the center of the two upper holes. Good agreement is made after comparing with Naghdi's results [68]. In the literature, Naghdi [68] and Bird and Steele [8] also calculated the stress concentration factor at the point B for $a = 0.12$ with various values of b . Bird and Steele [8] stated that the deviation by Naghdi's data is 11%. The grounds for this discrepancy were not identified in their paper. Our numerical results are more

agreeable to the Naghdi's data as shown in Figures 3-6 and 3-7, where Figure 3-7 was not provided by Bird and Steele [8]. In order to examine the boundary-layer effect at the present formulation, Figure 3-8 shows the Sc distribution close to the boundary. According to the convergence test in Figure 3-9, only eight terms ($L=8$) is sufficient in real implementation. In Figure 3-10, contour plots are shown for $b=0.4$ and $a=0.12$ with various orientations of $\bar{\theta}=\pi/8$, $\bar{\theta}=\pi/4$ and $\bar{\theta}=3\pi/8$ and it is anti-symmetric with respect to the horizontal axis.

Case 2: Two circular holes [6,8]

Consider a circular beam with two circular holes under bending as shown in Figure 3-11. One of the holes is concentric, and the other lies on the x -axis. In order to compare with the Bird and Steele's result, we assume $R=16$ and $a=1$, respectively. All the numerical results are also obtained by using ten terms of Fourier series ($L=10$). The stress concentration at the point P versus $D/2a$ (D is the nearest distance between the two holes) is shown in Figure 3-12. The stress concentration is expected to approach the case of a single hole in the center of beam cross section when $D/2a$ becomes large. The contour of stress concentration for the case of $D/2a=0.0625$ is shown in Figure 3-13. Our numerical results are well compared with the Bird and Steele's data.

3.5 Concluding remarks

The torsion problems of circular shaft weakened by several holes have been successfully solved by using the present formulation. Our solutions match well with the exact solution and other BIE solutions for the three Caulk's cases [14]. Only forty-one collocation points were uniformly distributed on each boundary to obtain more accurate results of torsional rigidity with error less than 1% after comparing with the known exact solution. Regardless of the number of circles, the proposed method shows great accuracy and generality. Through the demonstration of several examples, our method was successfully applied to cases of multiple holes.

For the bending problems with circular holes, an advantage of the present method

over the Naghdi's approach [68] is that the extension to multiple circular holes of arbitrary radii and positions is flexible and straightforward. Results obtained by using the present approach matched well with those of Naghdi's although Bird and Steele's data seems to deviate. Other gain of the present method over BEM is free of boundary-layer effect and exponential convergence. Although only two and four holes were tested to compare with Naghdi's [68] and Bird and Steele's results [8], our general-purpose program can solve problems with circular holes of arbitrary number and various positions of holes. Furthermore, our method presented here can be used to solve engineering problems which satisfy the Laplace operator.

Chapter 4 Application to exterior Helmholtz problems

Summary

In this chapter, we extend the unified formulation to the exterior Helmholtz problems with circular boundaries. Earthquake analysis for the site response of alluvial valley or canyon subject to the incident SH-wave is the main concern. Not only the cavities but also inclusions are considered. Stress concentration factor of the cavity under the ground surface is studied. Besides, the surface amplitudes are examined for the inclusion problems. Image concept and technique of decomposition are utilized for half-plane problems. Numerical examples are given to test our program. The validity of the semi-analytical method is verified. Our advantages, well-posed model, principal value free, elimination of boundary layer effect and exponential convergence, by using the present method are achieved.

4.1 Introduction

One of the major concerns of engineering seismology is to understand and explain vibrational response of the soil excited by earthquakes. The problem of the scattering and diffraction of SH-waves by a two-dimensional arbitrary number and location of cavities and inclusions in full and half-planes is revisited in this chapter by using our unified formulation. In 1971, Trifunac [79] has solved the problem of a single semi-circular alluvial valley subject to SH-wave. Later, Pao and Mao [70] have published a book on the stress concentration in 1972. In 1973, Trifunac [80] has also derived the closed-form solution of a single semi-circular canyon subject to the SH-wave. The earliest reference to a closed-form solution of the scattering and diffraction of the incident SH-wave by an underground inclusion exists in an article concerning an underground circular tunnel by Lee and Trifunac [55]. In order to extend to arbitrary shape inclusion problems, Lee and Manoogian [53] have used the weighted residual method to revisit the problem of scattering and diffraction of

SH-wave with respect to an underground cavity of arbitrary shape in a two-dimensional elastic half-plane. In the following years, they extended to the half-plane problem with a inclusion of arbitrary shape [61,62]. According to the literature review, it is observed that exact solutions for boundary value problems are only limited for simple cases, *e.g.* half-plane with a semi-circular canyon, a cavity under half-plane, an inclusion under half-plane. Therefore, proposing a systematic approach for solving exterior Helmholtz problems with circular boundaries of various numbers, positions and radii is our goal in this chapter. Our approach can deal with a cavity problem as a limiting case of an inclusion problem with zero shear modulus.

In this chapter, the boundary integral equation method (BIEM) is utilized to solve the half-plane radiation and scattering problems with circular boundaries. To fully utilize the geometry of circular boundary, not only Fourier series for boundary densities as previously used by many researchers but also the degenerate kernel for fundamental solutions in the present formulation is incorporated into the null-field integral equation. The key idea is that we can push the null-field point exactly on the real boundary by using appropriate degenerates kernel in real computation. All the improper boundary integrals are free of calculating the principal values (Cauchy and Hadamard) in place of series sum. In integrating each circular boundary for the null-field equation, the adaptive observer system of polar coordinate is considered to fully employ the property of degenerate kernel. For the hypersingular equation, vector decomposition for the radial and tangential gradients is carefully considered, especially in the nonfocal case. A scattering problem subject to the incident wave is decomposed into two parts, incident plane wave field and radiation field. The radiation boundary condition is the minus quantity of incident wave function for matching the boundary condition of total wave for cavity. Not only the stress concentration of the cavity is addressed, but also the surface displacements of alluvial valley and inclusion problems are solved in this chapter.

4.2 Degenerate kernels of BIE formulation for the Helmholtz problem

The governing equation of the incident SH-wave problem is the Helmholtz equation as shown below

$$(\nabla^2 + k^2)u(x) = 0, \quad x \in \Omega \quad (4-1)$$

where ∇^2 , k and Ω are the Laplacian operator, the wave number, and the domain of interest, respectively. Based on the dual boundary integral formulation of the domain point [101], we have

$$2\pi u(x) = \int_B T(s, x)u(s)dB(s) - \int_B U(s, x)t(s)dB(s), \quad x \in \Omega, \quad (4-2)$$

$$2\pi \frac{\partial u(x)}{\partial n_x} = \int_B M(s, x)u(s)dB(s) - \int_B L(s, x)t(s)dB(s), \quad x \in \Omega, \quad (4-3)$$

where s and x are the source and field points, respectively, $t(s)$ is the directional derivative of $u(s)$ along the outer normal direction at s , and n_x is the outward normal vector at the field point x . The $U(s, x)$, $T(s, x)$, $L(s, x)$ and $M(s, x)$ represent the four kernel functions which will be elaborated on later by using the degenerate kernel expansion. The kernel function, $U(s, x)$, is the fundamental solution which satisfies

$$(\nabla^2 + k^2)U(x, s) = 2\pi\delta(x - s), \quad (4-4)$$

where $\delta(x - s)$ denotes the Dirac-delta function. Then, we can obtain the fundamental solution as follows

$$U(s, x) = \frac{-i\pi H_0^{(1)}(kr)}{2}, \quad (4-5)$$

$$T(s, x) = \frac{\partial U(s, x)}{\partial n_s}, \quad L(s, x) = \frac{\partial U(s, x)}{\partial n_x}, \quad M(s, x) = \frac{\partial^2 U(s, x)}{\partial n_x \partial n_s}, \quad (4-6)$$

where $H_n^{(1)}(kr)$ is the n th order Hankel function of the first kind, $r \equiv |s - x|$, n_s denotes the outward normal vector at the source point s . In the present method, we adopt the mathematical tools, degenerate kernels, for the purpose of analytical study. The combination of degenerate kernels and Fourier series plays the major role in handling problems with circular boundaries. Based on the separable property, the kernel function $U(s, x)$, $T(s, x)$, $L(s, x)$ and $M(s, x)$ can be expanded into separable form by dividing the source point ($s = (R, \theta)$) and field point ($x = (\rho, \phi)$) in the polar coordinate [25].

$$U(s, x) = \begin{cases} U^i(s, x) = \frac{-\pi i}{2} \sum_{m=0}^{\infty} \varepsilon_m J_m(k\rho) H_m^{(1)}(kR) \cos(m(\theta - \phi)), R \geq \rho \\ U^e(s, x) = \frac{-\pi i}{2} \sum_{m=0}^{\infty} \varepsilon_m H_m^{(1)}(k\rho) J_m(kR) \cos(m(\theta - \phi)), \rho > R \end{cases}, \quad (4-7)$$

$$T(s, x) = \begin{cases} T^i(s, x) = \frac{-\pi k i}{2} \sum_{m=0}^{\infty} \varepsilon_m J_m(k\rho) H_m'^{(1)}(kR) \cos(m(\theta - \phi)), R > \rho \\ T^e(s, x) = \frac{-\pi k i}{2} \sum_{m=0}^{\infty} \varepsilon_m H_m^{(1)}(k\rho) J_m'(kR) \cos(m(\theta - \phi)), \rho > R \end{cases}, \quad (4-8)$$

$$L(s, x) = \begin{cases} L^i(s, x) = \frac{-\pi k i}{2} \sum_{m=0}^{\infty} \varepsilon_m J_m'(k\rho) H_m^{(1)}(kR) \cos(m(\theta - \phi)), R > \rho \\ L^e(s, x) = \frac{-\pi k i}{2} \sum_{m=0}^{\infty} \varepsilon_m H_m'^{(1)}(k\rho) J_m(kR) \cos(m(\theta - \phi)), \rho > R \end{cases}, \quad (4-9)$$

$$M(s, x) = \begin{cases} M^i(s, x) = \frac{-\pi k^2 i}{2} \sum_{m=0}^{\infty} \varepsilon_m J_m'(k\rho) H_m'^{(1)}(kR) \cos(m(\theta - \phi)), R \geq \rho \\ M^e(s, x) = \frac{-\pi k^2 i}{2} \sum_{m=0}^{\infty} \varepsilon_m H_m'^{(1)}(k\rho) J_m'(kR) \cos(m(\theta - \phi)), \rho > R \end{cases}, \quad (4-10)$$

where $i^2 = -1$, the superscripts “ i ” and “ e ” denote the interior and exterior cases for the expressions of kernel, respectively, and ε_m is the Neumann factor

$$\varepsilon_m = \begin{cases} 1, & m = 0 \\ 2, & m = 1, 2, \dots, \infty \end{cases}. \quad (4-11)$$

It is noted that the larger argument is imbedded in the complex Hankel function (H) instead of real Bessel function (J) to ensure the $H_0(kr)$ singularity and series convergence. Since the potential resulted from $T(s, x)$ and $L(s, x)$ kernels are discontinuous cross the boundary, the potentials of $T(s, x)$ for $R \rightarrow \rho^+$ and $R \rightarrow \rho^-$ are different. This is the reason why $R = \rho$ is not included in expressional degenerate kernels of $T(s, x)$ and $L(s, x)$ in Eqs. (4-8) and (4-9). The analytical evaluation of the integrals for each element in the influence matrix is listed in the Appendix and they are all non-singular. Besides, the limiting case to the boundary is also addressed. The continuous and jump behavior across the boundary is also described. After using the Wronskian property of J_m and Y_m

$$\begin{aligned} W(J_m(kR), Y_m(kR)) &= Y_m'(kR) J_m(kR) - Y_m(kR) J_m'(kR) \\ &= \frac{2}{\pi k R}, \end{aligned} \quad (4-12)$$

the jump behavior is well captured by

$$\begin{aligned}
& \int_0^{2\pi} (T^i(s, x) - T^e(s, x)) \cos(n\theta) R d\theta \\
& = kR\pi^2 J_n(kR) [Y'_n(kR) - iJ'_n(kR)] \cos(n\phi) \\
& \quad - kR\pi^2 J'_n(kR) [Y_n(kR) - iJ_n(kR)] \cos(n\phi) \\
& = 2\pi \cos(n\phi),
\end{aligned} \tag{4-13}$$

$$\begin{aligned}
& \int_0^{2\pi} (T^i(s, x) - T^e(s, x)) \sin(n\theta) R d\theta \\
& = kR\pi^2 J_n(kR) [Y'_n(kR) - iJ'_n(kR)] \sin(n\phi) \\
& \quad - kR\pi^2 J'_n(kR) [Y_n(kR) - iJ_n(kR)] \sin(n\phi) \\
& = 2\pi \sin(n\phi),
\end{aligned} \tag{4-14}$$

The above equation is similar to the Wronskian of two bases for 1-D rod case.

4.3 Image technique for solving scattering problems of half-plane

Image concept for half-plane problems

For the half-plane problem with a circular cavity and/or inclusion as shown in Appendixes and , we extend the problem into a full plane with the scatter by using image concept such that our formulation can be applied. By applying the concept of even function, the symmetry condition is utilized to satisfy the traction free ($t = 0$) condition on the ground surface. We merge the half-plane domain into the full-plane problem by adding with the reflective wave. To solve the problem, the decomposition technique is employed by introducing two plane waves, one is incident and the other is reflective, instead of only one incident wave. After taking the free body of full-plane problem through the ground surface, we obtain the desired solution which satisfies the Helmholtz equation and all the boundary conditions in the half-plane domain.

Decomposition of scattering problem into incident wave field and radiation problems

For the scattering problem subject to the incident wave, this problem can be decomposed into two parts. One is the incident wave field and another is the radiation field as shown in Appendixes and . The relations between two parts are shown

below

$$u_t^M = u^i + u^r + u^M, \quad (4-15)$$

$$t_t^M = t^i + t^r + t^M, \quad (4-16)$$

where the “ t_t^M ” denotes the total field of matrix including radiation and scattering. The subscripts “ i ” and “ r ” are the incident and reflected waves and the “ t^M ” denotes the radiation part of matrix and needs to be solved. To match the boundary condition for the cavity case, the total traction is defined as $t_t^M = 0$. For the inclusion case, we have the two constraints of the continuity of displacement and equilibrium of traction along the k th interface ($B_k, k = 1, \dots, N$) as shown below:

$$u_t^M = u^I \text{ on } B_k, \quad (4-17)$$

$$\mu^M t_t^M = -\mu^I t^I \text{ on } B_k. \quad (4-18)$$

The radiation parts of matrix (u^M and t^M) and inclusion (u^I and t^I) can be solved by employing our method.

4.4 Half-plane problems with a cavity subject to the incident SH-wave

4.4.1 Problem statement

The anti-plane motion model to be analyzed is shown in Figure 4-1. Consider a half-plane problem with a circular cavity of radius a . The governing equation of the incident SH-wave problem is the Helmholtz equation

$$(\nabla^2 + k^2)w(x) = 0, \quad x \in \Omega, \quad (4-19)$$

where ∇^2 , k and Ω are the Laplacian operator, the wave number, and the domain of interest, respectively. The displacement field of the SH-wave is defined as

$$u = v = 0, \quad w = w(x, y), \quad (4-20)$$

where w is the only nonvanishing component of displacement with respect to the Cartesian coordinate which is a function of x and y . For a linear elastic body, the

stress components are [99]

$$\sigma_{13} = \sigma_{31} = \mu \frac{\partial w}{\partial x}, \quad (4-21)$$

$$\sigma_{23} = \sigma_{32} = \mu \frac{\partial w}{\partial y}, \quad (4-22)$$

where μ is the shear modulus. The incident excitation of the half-plane problem, w^i , is defined as a steady-state plane SH-wave, and motion in the z direction. It may be expressed as follows

$$w^i = W_0 e^{ik(x \sin \gamma + y \cos \gamma)}, \quad (4-23)$$

where W_0 is the constant amplitude. By using the image concept and the decomposition of superposition as shown in Appendix , the total stress field in the medium is decomposed into

$$\sigma_{31}^t = \sigma_{31}^M + \sigma_{31}^i + \sigma_{31}^r, \quad (4-24)$$

$$\sigma_{32}^t = \sigma_{32}^M + \sigma_{32}^i + \sigma_{32}^r, \quad (4-25)$$

and the total displacement can be given as

$$w^t = w^M + w^i + w^r, \quad (4-26)$$

where w^i , w^r and w^M are the displacements due to the incident, reflected and radiation field of matrix. Only the radiation displacement “ w^M ” need to be solved after decomposition. In order to satisfy the traction free condition on the cavity, the traction is in equilibrium as shown below

$$0 = t^M + t^i + t^r, \quad (4-27)$$

Therefore, the scattering problem is reduced to find the displacement w^M which satisfies the Helmholtz equation and the boundary conditions. The shear stress components, σ_{rz} and $\sigma_{\theta z}$, can be superimposed by using σ_{31} and σ_{32} as shown below:

$$\sigma_{rz} = \mu \frac{\partial w}{\partial n}, \quad (4-28)$$

$$\sigma_{\theta z} = \mu \frac{\partial w}{\partial t}, \quad (4-29)$$

where n and t are the normal and tangent directions, respectively. Before determining σ_{rz} and $\sigma_{\theta z}$ of the interior point, we calculate σ_{31} and σ_{32} by

implementing the hypersingular equation in the real computation. For calculating shear stress $\sigma_{\theta z}$ on the boundary, the same procedure of vector decomposition is required, and the nondimensional stress $\sigma_{\theta z}^*$ is defined as:

$$\sigma_{\theta z}^* = \left| \frac{\sigma_{\theta z}}{\sigma_0} \right|, \quad (4-30)$$

where $\sigma_0 = \mu k W_0$ is the amplitude of incident wave.

4.4.2 Illustrative examples and discussions

In order to check the validity of the present formulation, the limiting case of incident SH-wave reduces to the static case of Honein *et al.* [44] is conducted. For the incident SH-wave problem, one cavity in the infinite plane subject to SH-wave is solved and is compared with the Pao and Mow's analytical solution [70]. Lin and Liu's half-plane problems with a cavity are also revisited [57]. All the numerical results are given below by using ten terms of Fourier series ($L = 10$).

Case1: Two circular cavities lie on the y-axis

Figures 2 (a) and (b) shows the geometry of the two circles whose radii are $a_1 = 1$ and $a_2 = 2$. For the static case, the displacement field of the anti-plane deformation is defined as:

$$w^\infty = \frac{\tau^\infty y}{\mu}. \quad (4-31)$$

In the dynamic case with traction free condition on the circular boundaries, we assume an incident SH-wave with amplitude of linear function in the y direction as:

$$w^i = \frac{\tau^\infty y}{\mu} e^{ikx}. \quad (4-32)$$

When k approaches zero, the problem is reduced to a static case where Honein *et al.*'s solution can be compared with for $D = 2, 0.1$ and 0.01 . Figures 2 (e) and (f) show the graph of the stress $\sigma_{\theta z}$ around the boundary of smaller circle for various distances, D , between the two circles. Our numerical results are well compared with the data of Honein *et al.*'s data [44] when k approaches zero ($k = 0.001$) by using

ten Fourier terms ($L = 10$).

Case2: A circular cylinder cavity in an infinite plane

Consider a circular cylinder with a radius “ a ” as shown in Figure 4-3 (a). An incident SH-wave is defined by

$$u_x = 0, u_y = 0, u_z = W_0 e^{ikx}, \quad (4-33)$$

Figures 4-3 (b) and (c) show the graph of the $\sigma_{\theta z}$ along the circular boundary for various wave numbers $ka = 0.1, 1.0$ and 2.0 . It is worth noting that our data agree well with the analytical solution of Pao and Mow’s data [70].

Case3: Half-plane problems with a circular cavity

Consider the scattering problem of SH-wave around a circular cavity in half-plane as shown in Figure 4-1. The boundary conditions are traction free on the circular boundary and ground surface. Figures 4-4 (e) to (h) are the Lin and Liu’s data [89] which show the graph of the $\sigma_{\theta z}^*$ around the circular cavity. In the case of $\gamma = \pi/4$ and $h/R = 1.5$, the maximum value of $\sigma_{\theta z}^*$ is 3.75 on $\theta = 90^\circ$, while the maximum value of $\sigma_{\theta z}^*$ is 2.16 on $\theta = 0^\circ$ and 180° for the case of $\gamma = \pi/4$ and $h/R = 12$. Before solving the half-plane problem, an image method is employed to extend the half-plane to full-plane with two holes by using the symmetry condition as shown in Appendix . Therefore, the developed program of our formulation can be easily incorporated to obtain the solution. Our numerical results are compared with the data of Lin and Liu’s data [89], good agreement is obtained. By setting $\gamma = 0^\circ, h/a = 100$ for the half-plane problem, the limiting case of a single cavity in the full plane is obtained due to the far distance between the ground surface and circle. After comparing the Figure 4-4 (i) with Figure 4-3 (c), good agreement is also obtained.

4.5 Half-plane problems with inclusions subject to the incident SH-wave

4.5.1 Problem statement

Half-plane problems with alluvial or inclusions to be analyzed is shown in Figures 4-5, 20, 25 and 31. The matrix and alluvial are assumed to be elastic, isotropic and homogenous, and the interface between the alluvial and matrix is assumed to be perfect. The governing equation of the anti-plane SH-wave harmonic motion is

$$\mu \nabla^2 w(x) + \rho \omega^2 w(x) = 0, \quad x \in \Omega \quad (4-34)$$

where μ , ρ and ω are the material properties of shear modulus, the density and the frequency, ∇^2 and Ω are the Laplacian operator and the domain of interest, respectively. The anti-plane displacement field of the anti-plane is defined as

$$u = v = 0, \quad w = w(x, y), \quad (4-35)$$

where w is the only nonvanishing component of displacement with respect to the Cartesian coordinate which is a function of x and y . The traction free boundary condition at the ground surface of the half-plane is defined as follows

$$\tau_{yz} = \mu \frac{\partial w}{\partial y} = 0, \quad y = 0, \quad (4-36)$$

or can be represented in the polar coordinate as

$$\tau_\theta = \frac{\mu}{r} \frac{\partial w}{\partial \theta} = 0, \quad \theta = 0 \text{ and } \pi. \quad (4-37)$$

The incident excitation of the half-plane, w^i , is defined as a steady-state plane SH-wave, and motion in the z direction. It is expressed as shown below:

$$w^i = W_0 e^{ik(x \sin \gamma + y \cos \gamma)}, \quad (4-38)$$

where W_0 is the constant amplitude. By using the image concept and the decomposition of superposition as shown in Appendix , the problem can be extended to a full-plane problem with two inclusions. In order to satisfy the traction free condition on the surface, the reflective wave is chosen to satisfy the symmetry condition as

$$w^r = W_0 e^{ik(x \sin \gamma - y \cos \gamma)}. \quad (4-39)$$

Assuming the perfect bounding between the matrix and inclusion, the continuity of displacement in the interface is given by

$$w^i + w^r + w^M - w^I = 0, \quad (4-40)$$

and the equilibrium of traction is shown below

$$\begin{aligned} & \mu^M \left[\frac{\partial w^{i+r}}{\partial r} \mathbf{n}_r^M + \frac{1}{r} \frac{\partial w^{i+r}}{\partial \theta} \mathbf{n}_\theta^M + \frac{\partial w^M}{\partial r} \mathbf{n}_r^M + \frac{1}{r} \frac{\partial w^M}{\partial \theta} \mathbf{n}_\theta^M \right] \\ & + \mu^I \left[\frac{\partial w^I}{\partial r} \mathbf{n}_r^I + \frac{1}{r} \frac{\partial w^I}{\partial \theta} \mathbf{n}_\theta^I \right] = 0 \end{aligned} \quad (4-41)$$

where w^i , w^r , w^M and w^I are the displacements due to the incident, reflecting, radiation of the matrix and inclusion, respectively. The unit normal vectors of $\mathbf{n}^M = n_r^M \mathbf{e}_r + n_\theta^M \mathbf{e}_\theta$ and $\mathbf{n}^I = n_r^I \mathbf{e}_r + n_\theta^I \mathbf{e}_\theta$ are the outward vectors for the boundaries of the matrix and the inclusion, respectively. Therefore, the incident SH-wave problem is reduced to find the displacement w^M and w^I which satisfies the Helmholtz equation and the two interface conditions. The total displacement field of matrix can be obtained by

$$w_t^M = w^i + w^r + w^M, \quad (4-42)$$

where the displacement field within the inclusion is defined as w^I . Assuming perfect bounding between the matrix and inclusion, the continuity of displacement ($w_t^M(x) = w^I(x)$) and traction equilibrium ($\mu^M t_t^M(x) = -\mu^I t^I(x)$) are satisfied on the interface boundary. In order to check the validity of the formulation, the Manoogian [61] and Trifunac's [79] problem with an alluvial valley is revisited. We follow the same parameter, η , for comparison purpose. The dimensionless frequency η is defined as shown below:

$$\eta = \frac{2a}{\lambda} = \frac{k^M a}{\pi} = \frac{\omega a}{\pi c^M}, \quad (4-43)$$

where a is the half-width of the alluvial valley, ω is the angular frequency, k^M and c^M are the shear wave number and the velocity of shear wave for the matrix wedium, and the shear wave number k is defined as

$$k = \frac{\omega}{c}. \quad (4-44)$$

Substituting Eq. (4-43) into Eq. (4-44), the wave number of matrix field is rewritten as

$$k^M = \frac{\pi \eta}{a}, \quad (4-45)$$

and the shear wave number for the inclusion field is obtained by

$$\frac{k^I}{k^M} = \frac{c^M}{c^I} = \left(\frac{\mu^M}{\mu^I} \cdot \frac{\rho^I}{\rho^M} \right)^{1/2}. \quad (4-46)$$

Equation (4-46) indicates that various mediums yield different wave numbers. The surface amplitude is an important index for the earthquake engineering. If the amplitude of incident plane SH-wave is one, the responses at different locations represent amplifications of the incident wave. The resultant motion is defined by the modulus

$$Amplitude = \sqrt{\text{Re}^2(w) + \text{Im}^2(w)}, \quad (4-47)$$

where $\text{Re}(w)$ and $\text{Im}(w)$ are the real and imaginary parts of total displacement, respectively. For both the alluvial valley and inclusion under the ground surface, observation points are located on the free surface in the range of $-1 < x/a < 1$. Therefore, the observation point locates on the matrix for inclusion under the ground surface, while the observation is on the inclusion for the alluvial valley problem.

4.5.2 Illustrative examples and discussions

In the section, we revisit the same problems of Lee and Manoogian [62], Trifunac [79] and Tsaur *et al.* [103] for the alluvial problem. The half-plane medium subject to SH-wave with an inclusion under the ground surface as previously solved by Lee and Manoogian and Tsaur *et al.* are also revisited. In order to check the accuracy of the present method, the limiting case is conducted. All the numerical results are given below by using ten terms of Fourier series.

Case 1: Half-plane problem with an alluvial valley subject to the SH-wave

In the following examples, we choose the same parameters $h/a = 1.0$, $\mu^I / \mu^M = 1/6$ and $\rho^I / \rho^M = 2/3$ which were previously adopted in the Ph. D dissertation of Manoogian [61]. Figures 4-6 to 4-9 show the surface amplitudes for various parameters of η . In each figure, four various incident angles ($\gamma = 0^\circ, 30^\circ, 60^\circ$ and 90°) are considered. The figures show the displacement amplitude on the ground surface only. Displacements are plotted with respect to the dimensionless distance

x/a for a specified parameter η . In order to verify the limiting case of the general program, we set $\mu^I / \mu^M = 10^{-8}$ to reduce to four canyon cases of η (0.5, 1.0, 1.5 and 2.0). In Figures 4-10 to 4-13, good agreements are obtained after comparing with Lee and Manoogian's results [53] for various frequency parameters of η for the semi-circular canyon case. Another limiting case of the rigid alluvial is also of interest in the foundation engineering. For example, rigid footing is a popular model in geotechnical engineering. By setting μ^I / μ^M to be infinity, the limiting case of rigid inclusion can be obtained. Figure 4-14 plots the surface displacement by setting $\mu^I / \mu^M = 10^4$ and $\eta = 2$ in the real computation. In the range of $x/a = -1$ to 1, the amplification is a constant as expected, because it is undeformed due to the rigid alluvial.

Figures 4-15 to 4-17 show the surface displacement for $\eta = 0.25, \dots, 2.50$, for various values of ρ^I / ρ^M and c^I / c^M , subject to the vertically incident SH-wave ($\gamma = 0^\circ$) whose amplitude is one. The point $x/a = 1$ corresponds to the edge of the alluvial valley, and the position of $x/a = 0$, shows the center of alluvial valley. Since all displacement amplitudes are symmetric about the center, for the vertically incident SH-wave, only the positive x/a axis is illustrated. In Figures 4-15 and 4-16, they show the effect of c^I / c^M on the surface amplitudes. The soft-basin effect of high amplitude is observed in this study. Figure 4-17 is an example of harder material in the alluvial valley and softer matrix. It is found that the surface amplitude is two as expected when η is small. For the far field response, the surface amplitude is found to be two since the perturbation due to the alluvial/inclusion is small. Figure 4-18 compares the surface displacement amplitude for the vertical and horizontal incidence wave versus the dimensionless frequency η at $x/a = 0.8$, while Figure 4-19 shows the same comparison for $x/a = -0.8$. Good agreement is made after comparing with Trifunac's [79] results.

Case 2: Half-plane problem with two alluvial valleys subject to the SH-wave

Two semi-circular alluvial valleys subject to the incident SH-wave of γ angle are shown in Figure 4-20. Figures 4-21 and 4-22 show the surface displacements versus x/a for various incident angles with $\mu^I / \mu^M = 1/6$ and $\rho^I / \rho^M = 2/3$ subject to

four cases of η (0.5, 1.0, 1.5 and 2.0). By setting $\mu^I / \mu^M = 10^{-8}$, the limiting case of successive canyons is obtained as shown in Figures 4-23 and 4-24. Tsaur *et al.* [103] and Fang [93] have both calculated the problem of two semi-cylindrical alluvial valleys for the incident SH-wave. Tsaur *et al.* [103] pointed out that the deviation by Fang [93] is that Fang improperly used the orthogonal property. Good agreement is made after comparing with the results of Tsaur *et al.* [103]. For the incident angle of zero-degree, the surface displacement amplitude is symmetric. By increasing the incident angle, the displacement amplitude is gradually smaller in the back side of the alluvial valley or canyon due to the shield effect of two alluvial valleys or canyons. As the incident angle approaches ninety-degrees, the surface displacement amplitudes are all smaller than the “free field” in the back of the second alluvial. It indicates that two alluvial valleys can be the wave trap for the incident wave.

Case 3: An inclusion under the ground surface subject to the SH-wave

A circular inclusion under the ground surface subject to the incident SH-wave of incident angle of γ is shown in Figure 4-25. The surface displacement amplitude of Eq. (4-42) versus x/a is plotted in Figures 4-26 and 4-27 for various incident angles with $\mu^I / \mu^M = 1/6, \rho^I / \rho^M = 2/3$. Figure 4-26 shows the comparison with the Tsaur's data [102] and Manoogian and Lee's [62] result for the nondimensional frequency $\eta = 2$. The surface displacements of the present method match well with the Tsaur's data, but it deviates to Lee and Manoogian and Lee's [62] result. The discrepancy was explained by Manoogian [60] due to the precision limit in the FORTRAN code ten years ago. In order to verify the limiting case of the general program, we set $\mu^I / \mu^M = 10^{-8}$ for four cavities cases of η (0.5, 1.0, 1.5 and 2.0). Good agreement is made after comparing with the results of the cavity cases of Lee and Manoogian [53,61]. The comparisons are shown in Figures 4-28 and 4-29 for different distances (h) from the cavity to the ground surface of the half-plane. Another limiting case of the rigid inclusion is of interest for the foundation engineering. By setting μ^I / μ^M to infinity, the limiting case of rigid inclusion can be obtained. Figure 4-30 shows the surface displacement when we set $\mu^I / \mu^M = 10^4$ and $\eta = 2$ in the real computation.

Case 4: Half-plane problem with two inclusions subject to the SH-wave

In order to verify that the present approach can be extended to handle arbitrary number and various positions of circular inclusions, we consider the problem with two inclusions under the ground surface subject to SH-wave as shown in Figure 4-31. Figure 4-32 shows the surface amplitude of the two-inclusions problem with $\mu^I / \mu^M = 1/6, \rho^I / \rho^M = 2/3$ for four cases of η (0.1, 0.25, 0.75 and 1.25). For the limiting case, the two inclusions problem reduces to two cavities problem when we set $\mu^I / \mu^M = 10^{-8}$. Good agreements are obtained after comparing with the results of two- cavities problem of Jiang *et al.* [95] as shown in Figure 4-33.

All the figures show that amplitude profiles are relatively simple for the lower frequency incident waves and become complicated with higher peak amplitudes for the higher one. Surface responses are symmetrical for vertically incident SH-wave as the angle of incidence increases towards ninety degrees. Amplitudes tend to be somewhat larger and profiles are more complicated for the place in front of the first inclusion ($x/a < -1$). This is due to the interference of incident, reflected, and scattering waves near the inclusion.

Consequently, we have high confidence in the results of the present method after testing the program through several examples.

4.6 Concluding remarks

The first attempt to employ degenerate kernel in BIEM for problems with circular boundaries subject to the SH-wave was achieved. Not only cavity but also inclusion problems were treated. We have proposed a BIEM formulation by using degenerate kernels, null-field integral equation and Fourier series in companion with adaptive observer systems and vector decomposition. This method is a semi-analytical approach for problems with circular boundaries since only truncation error in the Fourier series is involved. Good agreements are obtained after comparing with previous results. The stress concentration factor of cavity case and the surface motion of half-plane problem with inclusions were determined. Parameter study on the

surface amplitudes was also addressed. Successive canyons and/or alluvial valleys as well as several inclusions beneath the ground surface were considered. The analysis of amplification and interference effects for valley and inclusions subject to SH-waves may explain the ground motion either observed or recorded during earthquake. The method shows great generality and versatility for the problems with multiple circular cavities and inclusions of arbitrary radii and positions.

Chapter 5 Derivation of Green's function and Poisson integral formula for annular Laplace problems

Summary

Null-field approach is employed to derive the Green's function for annular Dirichlet problems of the Laplace equation. Kernel functions and boundary densities are expanded by using the degenerate kernel and Fourier series, respectively. Series-form Green's function is derived and plotted. The Poisson integral formula is extended to an annular case from a circle. The Green's function of an exterior problem bounded by a circle is found to be the limiting case of the present solution.

5.1 Introduction

Green's function has been studied and applied in many fields by mathematicians as well as engineers [47,63]. According to the superposition principle, it can solve problems with distributed loading. The main difference between the fundamental solution (free-space Green's function) and Green's function is that it not only satisfies the governing equation with a concentrated source but also matches the boundary condition of the bounded domain. Poisson integral formula was constructed after the special Green's function is obtained. It is well known that the kernel function in the Poisson integral formula is the normal derivative of the Green's function for the Dirichlet problem of a circle. In deriving the Green's function, Thompson [77] proposed the concept of reciprocal radii to find the image source to satisfy the homogeneous Dirichlet boundary condition. Sommerfeld [74] and Greenberg [41] both utilized the concept of reciprocal radii of Thompson [77] to drive the Poisson integral formula. On the other hand, Chen and Wu [31] proposed an alternative way to find the location of image through the degenerate kernel. For problems with a complicated domain, a closed-form Green's function as well as series form is not easy to obtain. Analytical Green's functions have been presented for only a few configurations in two-dimensional problems using the theory of complex variable. Numerical Green's functions have received attention from BEM researchers by Telles *et al.* [76]. Melnikov [64] used the method of modified potential (MMP) to calculate

the Green's function of eccentric ring and half-plane problems with a circular boundary. Boley [9] analytically constructed the Green's function by using successive approximation. Adewale [2] proposed an analytical solution for an annular plate subjected to a concentrated load which also belongs to one kind of Green's function for the biharmonic operator.

In this chapter, we focus on the null-field approach to determine the Green's function for the annular Laplace problem. Based on the obtained Green's function, the extended Poisson formula for the annular problem subject to Dirichlet boundary conditions can be constructed.

5.2 Derivation of the Green's function for annular Laplace problems

5.2.1 Problem statement and null-field approach to construct the Green's function

For two-dimensional annular problems as shown in Figure 5-1, the Green's function satisfies

$$\nabla^2 G(x, \xi) = \delta(x - \xi), \quad x \in \Omega, \quad (5-1)$$

where Ω is the domain and $\delta(x - \xi)$ denotes the Dirac-delta function for the source at ξ . For simplicity, this Green's function is subject to the Dirichlet boundary condition

$$G(x, \xi) = 0, \quad x \in B, \quad (5-2)$$

where B is the boundary. In order to employ the Green's third identity as follows

$$\iint_D \left[u(x) \nabla^2 v(x) - v(x) \nabla^2 u(x) \right] dD(x) = \int_B \left[u(x) \frac{\partial v(x)}{\partial n} - v(x) \frac{\partial u(x)}{\partial n} \right] dB(x). \quad (5-3)$$

we need two systems, $u(x)$ and $v(x)$. By choosing $u(x)$ as $G(x, \xi)$ and setting $v(x)$ as the fundamental solution $U(x, s)$ such that

$$\nabla^2 U(x, s) = 2\pi \delta(x - s), \quad x \in \Omega, \quad (5-4)$$

we can obtain the fundamental solution as follows

$$U(s, x) = \ln r, \quad (5-5)$$

where r is the distance between s and x ($r \equiv |x - s|$). After exchanging with the

variables x and s , we have

$$2\pi G(x, \xi) = \int_B T(s, x) G(s, \xi) dB(s) - \int_B U(s, x) \frac{\partial G(s, \xi)}{\partial n_s} dB(s) + U(\xi, x), \quad (5-6)$$

where $T(s, x)$, is defined by

$$T(s, x) \equiv \frac{\partial U(s, x)}{\partial n_s}, \quad (5-7)$$

in which n_s denotes the outward normal vector at the source point s . To solve the above equation, we utilize the null-field integral equation to analytically derive the Green's function. To solve the unknown boundary density t for the annular Dirchlet problems, the field point x is located outside the domain to yield the null-field integral equation as shown below:

$$0 = \int_B T(s, x) G(s, \xi) dB(s) - \int_B U(s, x) \frac{\partial G(s, \xi)}{\partial n_s} dB(s) + U(\xi, x), \quad x \in \Omega^c, \quad (5-8)$$

where Ω^c is the complementary domain. By using the degenerate kernels, the BIE for the “boundary point” can be easily derived through the null-field integral equation by exactly collocating x on B in Eq. (5-8) [28].

5.2.2 Expansions of kernel and boundary density

Based on the separable property, the kernel function $U(s, x)$ can be expanded into series form by separating the field point (ρ, ϕ) and source point (R, θ) in the polar coordinate:

$$U(s, x) = \begin{cases} U^i(R, \theta; \rho, \phi) = \ln R - \sum_{m=1}^{\infty} \frac{1}{m} \left(\frac{\rho}{R} \right)^m \cos m(\theta - \phi), & R \geq \rho \\ U^e(R, \theta; \rho, \phi) = \ln \rho - \sum_{m=1}^{\infty} \frac{1}{m} \left(\frac{R}{\rho} \right)^m \cos m(\theta - \phi), & \rho > R \end{cases}, \quad (5-9)$$

It is noted that the leading term and the numerator in the above expansion involve the larger argument to ensure the log singularity and the series convergence, respectively. According to the definition of $T(s, x)$, we have

$$T(s, x) = \begin{cases} T^i(R, \theta; \rho, \phi) = \frac{1}{R} + \sum_{m=1}^{\infty} \left(\frac{\rho^m}{R^{m+1}} \right) \cos m(\theta - \phi), & R > \rho \\ T^e(R, \theta; \rho, \phi) = -\sum_{m=1}^{\infty} \left(\frac{R^{m-1}}{\rho^m} \right) \cos m(\theta - \phi), & \rho > R \end{cases}, \quad (5-10)$$

The boundary densities for the annular Dirichlet problem can be represented by using the Fourier series as shown below:

$$G(s, \xi) = 0, \quad s \in B_1 \text{ and } B_2, \quad (5-11)$$

$$\frac{\partial G(s, \xi)}{\partial n_s} = \begin{cases} p_0 + \sum_{m=1}^{\infty} (p_m \cos m\theta + q_m \sin m\theta), & s \in B_1 \\ \bar{p}_0 + \sum_{m=1}^{\infty} (\bar{p}_m \cos m\theta + \bar{q}_m \sin m\theta), & s \in B_2 \end{cases}, \quad (5-12)$$

where B_1 and B_2 denoted the inner and outer boundary of circles, respectively.

5.3 Series representation for the Green's function of an annular case

For the annular case subject to the Dirichlet boundary condition, the unknown Fourier series can be analytically derived. By collocating x on (b^+, ϕ) and (a^-, ϕ) in Eq (5-8), the null-field equations yield

$$\begin{aligned} 0 &= (1 - 2\pi b p_0 - 2\pi a \bar{p}_0) \ln b \\ &- \sum_{m=1}^{\infty} \frac{1}{m} \left\{ \left[b\pi p_m + a\pi \left(\frac{a}{b} \right)^m \bar{p}_m + \left(\frac{R_\xi}{b} \right)^m \cos m\theta_\xi \right] \cos m\phi + \left[b\pi q_m + a\pi \left(\frac{a}{b} \right)^m \bar{q}_m + \left(\frac{R_\xi}{b} \right)^m \sin m\theta_\xi \right] \sin m\phi \right\} \\ &, x \rightarrow (b^+, \phi), \end{aligned} \quad (5-13)$$

$$\begin{aligned} 0 &= (\ln R_\xi - 2\pi b \ln b p_0 - 2\pi a \ln a \bar{p}_0) \\ &- \sum_{m=1}^{\infty} \frac{1}{m} \left\{ \left[b\pi \left(\frac{a}{b} \right)^m p_m + a\pi \bar{p}_m + \left(\frac{a}{R_\xi} \right)^m \cos m\theta_\xi \right] \cos m\phi + \left[b\pi \left(\frac{a}{b} \right)^m q_m + a\pi \bar{q}_m + \left(\frac{a}{R_\xi} \right)^m \sin m\theta_\xi \right] \sin m\phi \right\} \\ &, x \rightarrow (a^-, \phi). \end{aligned} \quad (5-14)$$

The unknown Fourier series coefficient can be obtained as

$$\begin{Bmatrix} p_0 \\ \bar{p}_0 \end{Bmatrix} = \begin{Bmatrix} \frac{\ln a - \ln R_\xi}{2\pi b(\ln a - \ln b)} \\ \frac{\ln b - \ln R_\xi}{2\pi a(\ln b - \ln a)} \end{Bmatrix}, \quad (5-15)$$

$$\begin{Bmatrix} p_m \\ \bar{p}_m \end{Bmatrix} = \begin{Bmatrix} \frac{b^{m-1} \cos m\theta_\xi \left[b^m \left(\frac{R_\xi}{b} \right)^m - a^m \left(\frac{a}{R_\xi} \right)^m \right]}{(b^{2m} - a^{2m})\pi} \\ \frac{b^m \cos m\theta_\xi \left[b^m \left(\frac{a}{R_\xi} \right)^m - a^m \left(\frac{R_\xi}{b} \right)^m \right]}{a(b^{2m} - a^{2m})\pi} \end{Bmatrix}, \quad (5-16)$$

$$\begin{Bmatrix} q_m \\ \bar{q}_m \end{Bmatrix} = \begin{Bmatrix} \frac{b^{m-1} \sin m\theta_\xi \left[b^m \left(\frac{R_\xi}{b} \right)^m - a^m \left(\frac{a}{R_\xi} \right)^m \right]}{(b^{2m} - a^{2m})\pi} \\ \frac{b^m \sin m\theta_\xi \left[b^m \left(\frac{a}{R_\xi} \right)^m - a^m \left(\frac{R_\xi}{b} \right)^m \right]}{a(b^{2m} - a^{2m})\pi} \end{Bmatrix}. \quad (5-17)$$

By substituting all the boundary densities into the integral representation for the domain point, we have the series-form Green's function as shown below:

$$G(x, \xi) = -(b \ln b p_0 + a \ln \rho \bar{p}_0) + \sum_{m=1}^{\infty} \frac{1}{2m} \left[\left(b \left(\frac{\rho}{b} \right)^m p_m + a \left(\frac{a}{\rho} \right)^m \bar{p}_m \right) \cos m\phi + \left(b \left(\frac{\rho}{b} \right)^m q_m + a \left(\frac{a}{\rho} \right)^m \bar{q}_m \right) \sin m\phi \right] + \frac{\ln|x - \xi|}{2\pi}. \quad (5-18)$$

If we also expand the \ln function and collect the terms, we have

$$G(x, \xi) = - \left(b \ln b p_0 + a \ln \rho \bar{p}_0 - \frac{\ln R_\xi}{2\pi} \right) + \sum_{m=1}^{\infty} \frac{1}{2m} \left[\left(b \left(\frac{\rho}{b} \right)^m p_m + a \left(\frac{a}{\rho} \right)^m \bar{p}_m - \left(\frac{\rho}{R_\xi} \right)^m \frac{\cos m\theta_\xi}{\pi} \right) \cos m\phi + \left(b \left(\frac{\rho}{b} \right)^m q_m + a \left(\frac{a}{\rho} \right)^m \bar{q}_m - \left(\frac{\rho}{R_\xi} \right)^m \frac{\sin m\theta_\xi}{\pi} \right) \sin m\phi \right], \quad a \leq \rho \leq R_\xi \quad (5-19)$$

$$G(x, \xi) = - \left(b \ln b p_0 + a \ln \rho \bar{p}_0 - \frac{\ln \rho}{2\pi} \right) + \sum_{m=1}^{\infty} \frac{1}{2m} \left[\left(b \left(\frac{\rho}{b} \right)^m p_m + a \left(\frac{a}{\rho} \right)^m \bar{p}_m - \left(\frac{R_\xi}{\rho} \right)^m \frac{\cos m\theta_\xi}{\pi} \right) \cos m\phi + \left(b \left(\frac{\rho}{b} \right)^m q_m + a \left(\frac{a}{\rho} \right)^m \bar{q}_m - \left(\frac{R_\xi}{\rho} \right)^m \frac{\sin m\theta_\xi}{\pi} \right) \sin m\phi \right], \quad R_\xi \leq \rho \leq b \quad (5-20)$$

Two limiting cases are our concern. One is the interior case of a to be zero and the other is the exterior case of b to be infinity. Our results are shown in Table 5-2 to compare with previous results by Chen and Wu [31] as shown in Table 5-1. By taking limit of b to infinity and replacing R_ξ to R , Eqs. (5-21) and (5-22) are reduced to the exterior case [31] as shown in Table 5-1. The detailed proof is shown in Appendix

. Equations (5-21) and (5-22) can not be reduced to the interior case [31] due to the inconsistency of potential at the center for the limiting case of a to be near zero. For clarity, we perform two experiments by setting $(a=1, b=10^7, L=20, \xi=(1.25, 0^\circ))$ and $(a=0.001, b=1, L=20, \xi=(0.8, 0^\circ))$. Both figures agree our analytical prediction after comparing with those of Chen and Wu [31] as shown in Figure 5-2.

Now we move to solve the solution $w(x)$ as shown in Figure 5-1(b) for the following partial differential equation,

$$\nabla^2 w(x) = 0, \quad x \in \Omega, \quad (5-21)$$

subject to the following Dirichlet boundary condition

$$w(x) = f(\theta), \quad x \in B_1, \quad (5-22)$$

$$w(x) = g(\theta), \quad x \in B_2, \quad (5-23)$$

To extend the Poisson integral formula to an annular case for Eq. (5-21) subject to BCs of Eqs. (5-22) and (5-23), we have

$$2\pi w(x) = \int_{B_1+B_2} \frac{\partial G(s, x)}{\partial n_s} w(s) dB(s), \quad (5-24)$$

where $G(s, x)$ is the derived Green's function of Eq. (5-18). Equation (5-24) indicates the representation for the solution in terms of extended Poisson integral formula. Although the series-form Green's function for an annular case is derived analytically in the section, general Green's functions can be solved by a semi-analytical approach as shown in the chapter 2 except the addition of $U(x, \xi)$ term, a semi-analytical solution is shown in Figure 5-3 (b). It must be noted that $\partial/\partial n_s$ is $\partial/\partial R$ and $-\partial/\partial R$ for exterior and interior circles, respectively.

5.4 An illustrative example and discussions

Annular case (analytical solution and semi-analytical solution)

To avoid the degenerate scale [26], we design the radii of inner and outer boundaries

are 4 and 10. The source of the Green's function is located on $\xi = (0, 7.5)$. For the annular Green's function, both the analytical solution and the semi-analytical results are shown in Figure 5-3. The analytical solution is obtained by truncating Fourier series of fifty terms in real implementation. By collocating null-field points along the inner and outer boundaries with the same number of Fourier coefficients, the semi-analytical solution of Chapter 2 can be obtained. Good agreement is made to verify the validity of the program since it matches well with the analytical solution.

5.5 Concluding remarks

For the annular problem, we have proposed an analytical solution to construct the Green's function by using degenerate kernels and Fourier series. The series-form Green's function for the annular Dirichlet problem was derived which can extend the Poisson integral formula from a circle to an annular case. It is interesting to find that the Green's function of exterior problem bounded by a circle can be treated as a limiting case of our solution. We also proposed a semi-analytical solution for comparison purpose. The semi-analytical method can be extended to construct the Green's function of eccentric case. Since analytical solutions are not available, our semi-analytical results may provide a datum for other researchers' references.

Chapter 6 Conclusions and further research

6.1 Conclusions

The thesis is concerned with the semi-analytical solution of Laplace and Helmholtz equations in planar domain that are bounded by a finite number of circular holes and/or inclusions. The approach is via the null-field integral equations emphasizing on the two issues of avoiding the need of CPV and HPV and illuminating the boundary-layer effect. The key idea is to approximate the unknowns via truncated Fourier series on the circular boundaries and the kernels of the integral operators, that is, the fundamental solution by truncating the addition theorem to have the degenerate kernels. Based on the proposed formulation for solving the problems involving circular boundaries in different branches of engineering applications, some concluding remarks are itemized as follows:

1. A systematic way to solve the Laplace and Helmholtz problems with circular boundaries was proposed successfully in this thesis by using the null-field integral equation in conjunction with degenerate kernels and Fourier series. Problems involving infinite, semi-infinite and bounded domains with circular boundaries were examined to check the accuracy of the present formulation
2. Boundary integrals along the circular contour are performed analytically. The present method is seen as a “semi-analytical” approach since error purely ascribes to the truncated Fourier series. Convergence study using different numbers of Fourier series was also done.
3. In calculating the potential gradient using hypersingular formulation, adaptive observer system and vector decomposition technique were employed to efficiently solve the problems.
4. A torsion bar with multiple cavities was studied by using the present formulation.

Our solutions match well with the exact solution and other solutions by using the boundary integral equation for the Caulk and Ling's cases. For the bending problem, we also consider a cantilever beam with multiple cavities. The discrepancy between Naghdi's solution and Bird and Steele's data was examined. Our results agree the Naghdi's data better than Bird and Steele's results.

5. In the exterior Helmholtz problem, the stress concentration factor of the cavity was solved. Not only the infinite plane cases but also half-plane problems subject an incident SH-wave was considered. Image concept and technique of decomposition are utilized to transform half-plane problems to full-plane cases such that our formulation can solve. Numerical results are obtained and compared well with previous results by others.
6. We extended the cavity problem to inclusion problem. Basin problem is also our concern. The effect of softer and harder material of alluvial, on the amplification of amplitude for alluvial valleys was also studied. The results of the inclusion case show the superiority of our method over the Manoogian's data after comparing with the limiting cases and Tsaur's results.
7. When the wave number k approaches zero, the Helmholtz problem can be reduced to the Laplace problem. Laplace problem can be treated as a special case of the Helmholtz problem.
8. Our approach can deal with the cavity problem as a limiting of inclusion problem with zero shear modulus. On the hand, rigid footing can also be considered using higher values of shear modulus.
9. A general-purpose program for solving engineering problems involving the Laplace and Helmholtz problems with multiple circular cavities or inclusions of various radii and arbitrary positions was developed. Its possible applications in engineering are very broad, and are not limited by the topic in the thesis.

6.2 Further research

In this thesis, our formulation has been applied to solve the problem with circular boundaries by using the separate form of fundamental solutions and Fourier series expansions for boundary densities in the null-field integral equation. However, there are several researches which can be conducted.

1. In the thesis, the degenerate kernels are expanded in the polar coordinate and only problems with circular boundaries can be solved. For the general boundary, *e.g.* elliptical hole, it is obvious that our method can be directly applied once the kernel functions can be expanded to separate form in the elliptical coordinate.
2. Following the success of applications in two-dimensional problems, it is straightforward to extend this concept to 3-D problems with spherical inclusions and/or cavities using the corresponding 3-D degenerate kernel functions for fundamental solutions and spherical harmonic expansions for boundary densities.
3. The fundamental solution was expanded to degenerate kernels with respect to the single center by separable technique. Hence, an adaptive observer system was required to fully capture the geometry of each circle. The bi-observer expansion technique for the two point function of source and field systems may be suitable for the eccentric case in a more straightforward way free of adaptive observer system.
4. For problems with straight boundaries, our method can also be applied by changing the dummy variable θ into R , and Legendre and Chebyshev polynomials are suited to approximate the boundary densities on the regular and degenerate straight boundaries, respectively, to employ the orthogonal property of integration. How to keep the orthogonal property is the main challenge.
5. The present method has determined the torsional rigidity of a bar with circular holes. Following the success of this thesis, extending to the problem of torsional

rigidity of a bar with inclusions can be considered as a forum in the future.

6. The extension to hill scattering can be studied by using the present approach in conjunction with the multi-domain technique by decomposing the original problem into one interior problem of circular domain and a half-plane problem with a semi-circular canyon.
7. Although annular Green's functions were solved analytically and numerically in this thesis, the semi-analytical solution for the Green's function of eccentric case, mixed BC and multi-medium can be easily solved using our approach. Our semi-analytical results may provide a datum for other researcher's references.

References

- [1] Achenbach, J.D., Kechter, G.E. and Xu, Y.-L., 1988, Off-boundary approach to the boundary element method, *Computer Methods in Applied Mechanics and Engineering*, Vol. 70, pp. 191-201.
- [2] Adewale, A.O., 2006, Isotropic clamped-free thin annular plate subjected to a concentrated load, *ASME Journal of Applied Mechanics*, Vol. 73(4), pp.658-663.
- [3] Ang, W.T. and Kang, I., 2000, A complex variable boundary element method for elliptic partial differential equations in a multiply-connected region, *International Journal of Computer Mathematics*, Vol. 75, pp. 515-525.
- [4] Barone, M.R. and Caulk, D.A., 1985, Special boundary integral equations for approximate solution of potential problems in three-dimensional regions with slender cavities of circular cross-section, *IMA Journal of Applied Mathematics*, Vol. 35, pp. 311-325.
- [5] Barone, M.R. and Caulk, D.A., 2000, Analysis of liquid metal flow in die casting, *International Journal of Engineering Science*, Vol. 38, pp. 1279-1302.
- [6] Bird, M.D., 1992, A Fourier series method for determining the interaction of circular in homogeneities in harmonic and biharmonic problems, Ph.D. Dissertation, *Department of Mechanical Engineering*, Stanford University, USA.
- [7] Bird, M.D. and Steele, C.R., 1991, Separated solution procedure for bending of circular plates with circular holes, *ASME Applied Mechanics Reviews*, Vol. 44, pp. 27-35.
- [8] Bird, M.D. and Steele, C.R., 1992, A solution procedure for Laplace equation on multiply-connected circular domains, *ASME Journal of Applied Mechanics*, Vol. 59, pp. 398-404.
- [9] Boley B.A., 1956, A method for the construction of Green's functions, *Quarterly of Applied Mathematics*, Vo. 14, pp. 249-257.
- [10] Burton, A.J. and Miller, G.F., 1971, The application of integral equation methods to numerical solution of some exterior boundary value problems,

Proceedings of The Royal Society, Vol. A 323, pp. 201-210.

- [11] Cao, H., 1990, Scattering and difference of incident plane SH, P and SV waves by circular canyons with variable depth-to width ratios, Ph.D. Dissertation, *Department of Civil Engineering of University*, Southern California, USA.
- [12] Caulk, D.A., 1983, Analysis of steady heat conduction in regions with circular holes by a special boundary integral method, *IMA Journal of Applied Mathematics*, Vol. 30, pp. 231-246.
- [13] Caulk, D.A., 1983, Steady heat conduction from an infinite row of holes in a half-space or a uniform slab, *International Journal of Heat and Mass Transfer*, Vol. 26, pp. 1509-1513.
- [14] Caulk, D.A., 1983, Analysis of elastic torsion in a bar with circular holes by a special boundary integral method, *ASME Journal of Applied Mechanics*, Vol. 50, pp. 101-108.
- [15] Caulk, D.A., 1984, Special boundary integral equations for potential problems in regions with circular holes, *ASME Journal of Applied Mechanics*, Vol. 51, pp. 713-716.
- [16] Chen, C.T., 2005, Null-field integral equation approach for Helmholtz (interior and exterior acoustic) problems with circular boundaries, Master Thesis, *Department of Harbor and River Engineering, National Taiwan Ocean University*, Taiwan.
- [17] Chen, C.T., Chen, I.L. and Chen, J.T, 2005, Null-field integral equation approach for Helmholtz (interior and exterior acoustic) problems with circular boundaries, 九十四年電子計算機於土木水利工程應用研討會, 台南成大.
- [18] Chen, H.B., Lu, P., Schnack, E., 2001, Regularized algorithms for the calculation of values on and near boundaries in 2D elastic BEM, *Engineering Analysis with Boundary Elements*, Vol. 25(10), pp. 851-876.
- [19] Chen, I.L., 2002, Treatment of rank-deficiency problems and its applications for the Helmholtz equation using boundary element method, Ph.D. Dissertation, *Department of Harbor and River Engineering, National Taiwan Ocean University*, Taiwan.
- [20] Chen, J.T., 2005, Null-field integral equation approach for boundary value

problems with circular boundaries, *International Conference on Computational & Experimental Engineering Sciences*, India.

- [21] Chen, J.T. and Chiu, Y. P., 2002, On the pseudo-differential operators in the dual boundary integral equations using degenerate kernels and circulants, *Engineering Analysis with Boundary Elements*, Vol. 26, pp. 41-53.
- [22] Chen, J.T., Hsiao, C.C. and Leu, S.Y., 2006, Null-field integral equation approach for plate problems with circular boundaries, *ASME Journal of Applied Mechanics*, Vol.73, pp. 679-693.
- [23] Chen, J.T. and Hong, H.-K., 1999, Review of dual boundary element methods with emphasis on hypersingular integral and divergent series, *Applied Mechanics Reviews*, Vol. 52, pp. 17-33.
- [24] Chen, J.T., Lee, C.F. and Lin, S.Y., 2002, A new point of view for the polar decomposition using singular value decomposition, *International Journal of Computational and Numerical Analysis and Application*, Vol. 2(3), pp. 257-264.
- [25] Chen, J.T., Liu, L.W. and Hong, H.-K., 2003, Spurious and true eigensolutions of Helmholtz BIEs and BEMs for a multiply connected problem, *Proceedings of the Royal Society of London. Series A*, Vol. 459, pp. 1891-1924.
- [26] Chen, J.T. and Shen, W.C., 2006, Degenerate scale for multiply connected Laplace problems, *Mechanics Research Communications*, Accepted.
- [27] Chen, J.T., Shen, W.C. and Wu, A.C., 2005, Null-field integral equations for stress field around circular holes under anti- plane shear, *Engineering Analysis with Boundary Elements*, Vol. 30, pp. 205-217.
- [28] Chen, J.T., Shen, W.C., Chen, P.Y., 2006, Analysis of circular torsion bar with circular holes using null-field approach, *Computer Modeling in Engineering Science*, Vol.12 (2), pp.109-119.
- [29] Chen, J.T. and Wu, A.C., 2006, Null-field approach for piezoelectricity problems with arbitrary circular inclusion, *Engineering Analysis with Boundary Elements*, Accepted.
- [30] Chen, J.T. and Wu, A.C., 2006, Null-field approach for the multi-inclusion problem under anti-plane shears, *ASME Journal of Applied Mechanics*, Accepted.

- [31] Chen, J.T. and Wu, C.S., 2006, Alternative derivations for the Poisson integral formula, *International Journal of Mathematical Education in Science and Technology*, Vol. 37, pp. 165-185.
- [32] Chen, J.T., Wu, C.S., Lee, Y.T. and Chen, K.H., 2006, On the equivalence of the Trefftz method and method of fundamental solutions for Laplace and biharmonic equations, *Computers and Mathematics with Applications*, Accepted.
- [33] Chen, P.Y., Chen, C.T. and Chen, J.T., 2005, A semi-analytical approach for dynamic stress concentration factor of Helmholtz problems with circular holes, *The 29th National Conference on Theoretical and Applied Mechanics*, NTHU, Hsinchu.
- [34] Chen, T. and Weng, I.S., 2001, Torsion of a circular compound bar with imperfect interface, *ASME Journal of Applied Mechanics*, Vol. 68, pp. 955-958.
- [35] Chou, S.I., 1997, Stress field around holes in antiplane shear using complex variable boundary element method, *ASME Journal of Applied Mechanics*, Vol. 64, pp. 432-435.
- [36] Crouch, S.L. and Mogilevskaya, S.G., 2003, On the use of Somigliana's formula and Fourier series for elasticity problems with circular boundaries, *International Journal for Numerical Methods in Engineering*, Vol. 58, pp. 537-578.
- [37] Doicu, A. and Wriedt, T., 1997, Extended boundary condition method with multiple sources located in the complex plane, *Optics Communications*, Vol. 139, pp. 85-91.
- [38] Elsherbeni, A.Z. and Hamid, M., 1987, Scattering by parallel conducting circular cylinders, *IEEE Transactions on Antennas and Propagation*, Vol. 35, pp. 355-358.
- [39] Graff, K.F., 1975, Wave motion in elastic solids, *Ohio State University Press*.
- [40] Gray, L.J. and Manne, L.L., 1993, Hypersingular integrals at a corner, *Engineering Analysis with Boundary Elements*, Vol. 11, pp. 327-334.
- [41] Greenberg, M.D., 1971, Applications of Green's function in science and engineering, *Prentice-Hall*, New Jersey.
- [42] Guiggiani, M., 1995, Hypersingular boundary integral equations have an

- additional free term, *Computational Mechanics*, Vol. 16, pp. 245-248.
- [43] Honein, E., Honein, T. and Herrmann, G., 1992, Further aspects of the elastic field for two circular inclusions in antiplane elastostatics, *ASME Journal of Applied Mechanics*, Vol. 59, pp. 774-779.
 - [44] Honein, E., Honein, T. and Herrmann, G., 1992, On two circular inclusions in harmonic problem, *Quarterly of Applied Mathematics*, Vol. 50, pp. 479-499.
 - [45] Hromadka, T.V. and Lai, C., 1986, The complex variable boundary element method in engineering analysis, *Springer-Verlag*, New York.
 - [46] Hsiao, C.C., 2005, A semi-analytical approach for Stokes flow and plate problems with circular boundaries, Master Thesis, *Department of Harbor and River Engineering, National Taiwan Ocean University*, Taiwan.
 - [47] Jaswon, M.A., Symm, G.T., 1977, Integral equation methods in potential theory and electrostatics, *Scademic Press*, New York.
 - [48] Kress, R., 1989, Linear integral equations, *Springer-Verlag*, Berlin.
 - [49] Lebedev, N.N., Skalskaya, I.P. and Uflyand, Y.S., 1979, Worked problems in applied mathematics, *Dover*, New York.
 - [50] Lee, V.W., 1990, Scattering of plane SH-waves by a semi-parabolic cylindrical canyon in an elastic half-space., *Geophysical Journal International*, Vol. 100, pp. 79-86.
 - [51] Lee, V.W., 1982, A note on the scattering of elastic plane waves by a hemispherical canyon, *Soil Dynamics and Earthquake Engineering*, Vol. 1(3), pp. 122-129.
 - [52] Lee, V.W., Chen S. and Hsu, I.R., 1999, Antiplane diffraction from canyon above subsurface unlined tunnel, *Journal of Engineering Mechanics*, Vol. 125(6), pp. 668-675.
 - [53] Lee, V.W. and Manoogian, M.E., 1995, Surface motion above an arbitrary shape underground cavity for incident SH waves, *European Earthquake Engineering*, Vol. 1, pp. 3-11.
 - [54] Lee, V.W. and Sherif, R.I., 1996, Diffraction around circular canyon in elastic wedge space by plane SH-waves, *Journal of Engineering Mechanics*, Vol. 122(6), pp. 539-544.

- [55] Lee, V.W., Trifunac, M.D. and ASCE, A.M., 1978, Response of tunnels to incident SH-waves, *Journal of the Engineering Mechanics Division*, Vol. 105 (EM4), pp. 643-659.
- [56] Liao, W.I., Teng, T.J. and Yeh, C.S., 2004, A series solution and numerical technique for wave diffraction by a three-dimensional canyon, *Wave Motion*, Vol. 39, pp. 129-142.
- [57] Ling, C.B., 1947, Torsion of a circular tube with longitudinal circular holes, *Quarterly of Applied Mathematics*, Vol. 5, pp.168-181.
- [58] Liu, D.K. and Han, F., 1991, Scattering of plane SH-wave by cylindrical canyon of arbitrary shape, *Soil Dynamics and Earthquake Engineering*, Vol. 10(5), pp. 249-255.
- [59] Liu, Y.J., He, Z.Y. and Fan, H.M., 2004, Scattering of SH-waves by an interface cavity, *Acta Mechanica*, Vol. 170, pp. 47-56.
- [60] Manooqian, M.E., 2006, Private communication.
- [61] Manooqian, M.E., 1992, Scattering and difference of plane SH-waves by surface and subsurface discontinuities, Ph.D. Dissertation, *Department of Civil Engineering of University*, Southern California, USA.
- [62] Manoogian, M.E. and Lee, V.W., 1996, Diffraction of SH-waves by subsurface inclusions of arbitrary shape, *Journal of Engineering Mechanics*, Vol. 122(2), pp. 123-129.
- [63] Melnikov, Y.A., 1977, Some Application of the Green's function method in mechanics, *International Journal of Solids and Structures*, Vol. 13, pp. 1045-1058
- [64] Melnikov, Y.A., 2001, Modified potential as a tool for computing Green's functions in continuum mechanics, *Computer Modeling in Engineering Science*, Vol. 2, pp. 291-305.
- [65] Mogilevskaya, S.G. and Crouch, S.L., 2001, A Galerkin boundary integral method for multiple circular elastic inclusions, *International Journal for Numerical Methods in Engineering*, Vol. 52, pp. 1069-1106.
- [66] Mow, C.C. and Mente, L.J., 1963, Dynamic stress and displacement around cylindrical discontinuities due to plane harmonic shear waves, *Transactions of*

the ASME, pp. 598-604.

- [67] Muskhelishvili, N.I., 1953, Some basic problems of the mathematical theory of elasticity, *Noordhoff*, Groningen.
- [68] Naghdi, A.K., 1991, Bending of a perforated circular cylindrical cantilever, *International Journal of Solids and Structures*, Vol. 28(6), pp. 739-749.
- [69] Pao, Y.H., 1962, Dynamical stress concentration in an elastic plate, *Transactions of the ASME*, Vol. June, pp.299-305.
- [70] Pao, Y.H. and Mow, C.C., 1972, Diffraction of elastic waves and dynamics stress concentration, *Cran*, New York.
- [71] Shams-Ahmadi, M. and Chou, S.I., 1997, Complex variable boundary element method for torsion of composite shafts, *International Journal for Numerical Methods in Engineering*, Vol. 40, pp. 1165-1179.
- [72] Shen, W.C., 2005, Null-field approach for Laplace problems with circular boundaries using degenerate kernels, Master Thesis, *Department of Harbor and River Engineering*, National Taiwan Ocean University, Taiwan.
- [73] Shen, W.C., Chen, P.Y. and Chen, J.T., 2005, Analysis of circular torsion bar with circular holes using null-field approach, 九十四年電子計算機於土木水利工程應用研討會, 台南成大.
- [74] Sommerfeld, A., 1949, Partial differential equations in physics, *Academic Press*, New York.
- [75] Sokolnikoff, I.S., 1956, Mathematical Theory of Elasticity, *McGraw-Hill*, New York.
- [76] Telles, J.C.F., Castor, G.S. and Guimaraes, S., 1995, Numerical Green's function approach for boundary elements applied to fracture mechanics, *International Journal for Numerical Methods in Engineering*, Vol. 38(19), pp.3259-3274.
- [77] Thomson, W. 1848 Maxwell in his treatise, Vol. I., Chap. XI, quotes a paper in the Cambridge and Dublin Math. Journ. of 1848.
- [78] Timoshenko, S.P. and Goodier, J.N., 1970, Theory of Elasticity, *McGraw-Hill*, New York.
- [79] Trifunac, M.D., 1971, Surface motion of a semi-cylindrical alluvial valley for

- incident plane SH waves, *Bulletin the Seismological Society of America*, Vol. 61(6), pp.1755-1770.
- [80] Trifunac, M.D., 1973, Scattering of plane SH waves by a semi-cylindrical canyon, *Earthquake Engineering and Structural Dynamics*, Vol. 1, pp. 267-281.
- [81] Trifunac, M.D. and Lee, V.W., 1996, Peak surface strains during strong earthquake motion, *Soil Dynamics and Earthquake Engineering*, Vol. 15, pp. 311-319.
- [82] Wang J., Mogilevskaya S.G. and Crouch S.L., 2002, A numerical procedure for multiple circular holes and elastic inclusions in a finite domain with a circular boundary, *Computational Mechanics*, Vol. 32, pp. 250-258.
- [83] Watermann, P.C., 1965, Matrix formulation of electromagnetic scattering, *Proc. IEEE*, Vol.53, pp.805-812.
- [84] Wu, A.C., Shen, W.C. and Chen, J.T., 2005, Null-field integral equation for stress field around circular inclusions under anti-plane shear, *The 29th National Conference on Theoretical and Applied Mechanics*, NTHU, Hsinchu.
- [85] 史守峡, 刘殿魁, 2001, SH 波与介面多圆孔的散射及应力集中, *力学学报*, Vol. 33(1), pp. 60-70。
- [86] 许贻燕, 韩峰, 1992, 平面 SH 波在相邻多个半圆形凹陷地形上的散射, *地震工程与工程振动*, Vol. 12(2), pp.12-18。
- [87] 林宏, 史文谱, 刘殿魁, 2001, SH 波入射时浅埋结构的动力分析, *哈尔滨工程大学学报*, Vol. 22(6), pp. 83-87。
- [88] 林宏, 史文谱, 刘殿魁, 2001, SH 波入射时浅埋结构的动力分析, *哈尔滨工程大学学报*, Vol. 22(6), pp. 83-87。
- [89] 林宏, 刘殿魁, 2002, 半无限空间中圆型孔洞周围 SH 波的散射, *地震工程与工程振动*, Vol. 22(2)。
- [90] 刘殿魁, 刘宏伟, 1998, SH 波散射与边界圆孔附近的动应力集中, *力学学报*, Vol. 30(5), pp. 597-604。
- [91] 刘殿魁, 刘宏伟, 1999, 孔边裂纹对 SH 波的散射及其动应力强度因子, *力学学报*, Vol. 3(3), 万方数据。
- [92] 刘殿魁, 许贻燕, 1993, 各项异性介质中 SH 波与多个半圆形凹陷地形的相互作用, *力学学报*, Vol. 25(1), pp.93-102。

- [93] 房营光, 1995, 二维地表相邻多个半圆弧沟谷对 SH 波的散射, *地震工程与工程振动*, Vol. 15(1), pp. 85-91。
- [94] 周焕林, 2003, 边界元素法中边界层效应和薄体问题的研究, 博士学位论文, *中国科学技术大学力学和机械工程系*。
- [95] 姜耙, 黄荣富, 刘殿魁, 王国庆, 2004, SH 波在浅埋多个圆孔处的地震动, *地震工程与工程振动*, Vol. 24(1), pp. 7-14。
- [96] 崔志刚, 郑永超, 刘殿魁, 1998, SH 波对圆弧形凸起地形的散射, *地震工程与工程振动*, Vol. 18(4)。
- [97] 袁晓铭, 廖振鹏, 1993, 圆弧形凹陷地形对平面 SH 波散射问题的级数解答, *地震工程与工程振动*, Vol. 13(2), pp. 1-11。
- [98] 袁晓铭, 廖振鹏, 1996, 任意圆弧形凸起地形对平面 SH 波的散射, *地震工程与工程振动*, Vol. 16(2)。
- [99] 汤任基, 1996, 裂纹柱的扭转理论, 上海交通大学出版社, 上海。
- [100] 陈志刚, 刘殿魁, 2004, SH 波冲击下浅埋任意型孔洞的动力分析, *地震工程与工程振动*, Vol. 24 (4), pp. 32-36。
- [101] 陳正宗, 洪宏基, 1992, 邊界元素法, 新世界, 台北台灣。
- [102] 曹登皓, 張高豪, 2006, Private communication。
- [103] 曹登皓, 張高豪, 林哲國, 2004, 多個半圓凹陷地形承受平面 SH 波的反應, *亞太工程科技學報*, Vol. 2(2), pp. 251-266。
- [104] 簡秋記, 蘇俊明, 陳文斌, 1996, 三維應力集中問題邊界元素法分析, *Chung Yuan Journal*, Vol. 24 (3), pp. 43-54。

Appendix Analytical evaluation of the integrals for Laplace kernels and their limit

	$U(s, x)$ and $\int_B U(s, x) t(s) dB(s)$	$T(s, x)$ and $\int_B T(s, x) u(s) dB(s)$
kernel		
Degenerate	$U(s, x) = \begin{cases} U^i(R, \theta; \rho, \phi) = \ln R - \sum_{m=1}^{\infty} \frac{1}{m} \left(\frac{\rho}{R} \right)^m \cos(m(\theta - \phi)), & R \geq \rho \\ U^e(R, \theta; \rho, \phi) = \ln \rho - \sum_{m=1}^{\infty} \frac{1}{m} \left(\frac{R}{\rho} \right)^m \cos(m(\theta - \phi)), & R < \rho \end{cases}$	$T(s, x) = \begin{cases} T^i(R, \theta; \rho, \phi) = \frac{1}{R} + \sum_{m=1}^{\infty} \frac{\rho^m}{R^{m+1}} \cos(m(\theta - \phi)), & R > \rho \\ T^e(R, \theta; \rho, \phi) = -\sum_{m=1}^{\infty} \frac{R^{m-1}}{\rho^m} \cos(m(\theta - \phi)), & R < \rho \end{cases}$
Orthogonal process	$\begin{cases} \int_0^{2\pi} \left[\ln R - \sum_{m=1}^{\infty} \frac{1}{m} \left(\frac{\rho}{R} \right)^m \cos(m(\theta - \phi)) \right] \cos(n\theta) R d\theta = \pi \frac{1}{n} \frac{\rho^n}{R^{n-1}} \cos(n\phi), & R \geq \rho \\ \int_0^{2\pi} \left[\ln R - \sum_{m=1}^{\infty} \frac{1}{m} \left(\frac{\rho}{R} \right)^m \cos(m(\theta - \phi)) \right] \sin(n\theta) R d\theta = \pi \frac{1}{n} \frac{\rho^n}{R^{n-1}} \sin(n\phi), & R \geq \rho \\ \int_0^{2\pi} \left[\ln \rho - \sum_{m=1}^{\infty} \frac{1}{m} \left(\frac{R}{\rho} \right)^m \cos(m(\theta - \phi)) \right] \cos(n\theta) R d\theta = \pi \frac{1}{n} \frac{R^{n+1}}{\rho^n} \cos(n\phi), & R < \rho \\ \int_0^{2\pi} \left[\ln \rho - \sum_{m=1}^{\infty} \frac{1}{m} \left(\frac{R}{\rho} \right)^m \cos(m(\theta - \phi)) \right] \sin(n\theta) R d\theta = \pi \frac{1}{n} \frac{R^{n+1}}{\rho^n} \sin(n\phi), & R < \rho \end{cases}$	$\begin{cases} \int_0^{2\pi} \left[\frac{1}{R} + \sum_{m=1}^{\infty} \frac{\rho^m}{R^{m+1}} \cos(m(\theta - \phi)) \right] \cos(n\theta) R d\theta = \pi \left(\frac{\rho}{R} \right)^n \cos(n\phi), & R > \rho \\ \int_0^{2\pi} \left[\frac{1}{R} + \sum_{m=1}^{\infty} \frac{\rho^m}{R^{m+1}} \cos(m(\theta - \phi)) \right] \sin(n\theta) R d\theta = \pi \left(\frac{\rho}{R} \right)^n \sin(n\phi), & R > \rho \\ \int_0^{2\pi} \left[-\sum_{m=1}^{\infty} \frac{R^{m-1}}{\rho^m} \cos(m(\theta - \phi)) \right] \cos(n\theta) R d\theta = -\pi \left(\frac{R}{\rho} \right)^n \cos(n\phi), & R < \rho \\ \int_0^{2\pi} \left[-\sum_{m=1}^{\infty} \frac{R^{m-1}}{\rho^m} \cos(m(\theta - \phi)) \right] \sin(n\theta) R d\theta = -\pi \left(\frac{R}{\rho} \right)^n \sin(n\phi), & R < \rho \end{cases}$
Limit	$\begin{cases} \lim_{\rho \rightarrow R} \left[\pi \frac{1}{n} \frac{\rho^n}{R^{n-1}} \cos(n\phi) \right] = \pi \frac{1}{n} R \cos(n\phi), & R \geq \rho \\ \lim_{\rho \rightarrow R} \left[\pi \frac{1}{n} \frac{\rho^n}{R^{n-1}} \sin(n\phi) \right] = \pi \frac{1}{n} R \sin(n\phi), & R \geq \rho \\ \lim_{\rho \rightarrow R} \left[\pi \frac{1}{n} \frac{R^{n+1}}{\rho^n} \cos(n\phi) \right] = \pi \frac{1}{n} R \cos(n\phi), & R < \rho \\ \lim_{\rho \rightarrow R} \left[\pi \frac{1}{n} \frac{R^{n+1}}{\rho^n} \sin(n\phi) \right] = \pi \frac{1}{n} R \sin(n\phi), & R < \rho \end{cases}$ <p>(Continuous for $R^- < \rho < R^+$)</p>	$\begin{cases} \lim_{\rho \rightarrow R} \left[\pi \left(\frac{\rho}{R} \right)^n \cos(n\phi) \right] = \pi \cos(n\phi), & R > \rho \\ \lim_{\rho \rightarrow R} \left[\pi \left(\frac{\rho}{R} \right)^n \sin(n\phi) \right] = \pi \sin(n\phi), & R > \rho \\ \lim_{\rho \rightarrow R} \left[-\pi \left(\frac{R}{\rho} \right)^n \cos(n\phi) \right] = -\pi \cos(n\phi), & R < \rho \\ \lim_{\rho \rightarrow R} \left[-\pi \left(\frac{R}{\rho} \right)^n \sin(n\phi) \right] = -\pi \sin(n\phi), & R < \rho \end{cases}$ <p>(jump for $R^- < \rho < R^+$)</p>

	$L(s, x) \text{ and } \int_B L(s, x) t(s) dB(s)$	$M(s, x) \text{ and } \int_B M(s, x) u(s) dB(s)$
kernel	$L(s, x) = \begin{cases} L^i(R, \theta; \rho, \phi) = -\sum_{m=1}^{\infty} \frac{\rho^{m-1}}{R^m} \cos(m(\theta - \phi)), & R > \rho \\ L^e(R, \theta; \rho, \phi) = \frac{1}{\rho} + \sum_{m=1}^{\infty} \frac{R^m}{\rho^{m+1}} \cos(m(\theta - \phi)), & R < \rho \end{cases}$	$M(s, x) = \begin{cases} M^i(R, \theta; \rho, \phi) = \sum_{m=1}^{\infty} m \frac{\rho^{m-1}}{R^{m+1}} \cos(m(\theta - \phi)), & R \geq \rho \\ M^e(R, \theta; \rho, \phi) = \sum_{m=1}^{\infty} m \frac{R^{m-1}}{\rho^{m+1}} \cos(m(\theta - \phi)), & R < \rho \end{cases}$
Orthogonal process	$\begin{cases} \int_0^{2\pi} \left[-\sum_{m=1}^{\infty} \frac{\rho^{m-1}}{R^m} \cos(m(\theta - \phi)) \right] \cos(n\theta) R d\theta = -\pi \left(\frac{\rho}{R} \right)^{n-1} \cos(n\phi), & R > \rho \\ \int_0^{2\pi} \left[-\sum_{m=1}^{\infty} \frac{\rho^{m-1}}{R^m} \cos(m(\theta - \phi)) \right] \sin(n\theta) R d\theta = -\pi \left(\frac{\rho}{R} \right)^{n-1} \sin(n\phi), & R > \rho \\ \int_0^{2\pi} \left[\frac{1}{\rho} + \sum_{m=1}^{\infty} \frac{R^m}{\rho^{m+1}} \cos(m(\theta - \phi)) \right] \cos(n\theta) R d\theta = \pi \left(\frac{R}{\rho} \right)^{n+1} \cos(n\phi), & R < \rho \\ \int_0^{2\pi} \left[\frac{1}{\rho} + \sum_{m=1}^{\infty} \frac{R^m}{\rho^{m+1}} \cos(m(\theta - \phi)) \right] \sin(n\theta) R d\theta = \pi \left(\frac{R}{\rho} \right)^{n+1} \sin(n\phi), & R < \rho \end{cases}$	$\begin{cases} \int_0^{2\pi} \left[\sum_{m=1}^{\infty} m \frac{\rho^{m-1}}{R^{m+1}} \cos(m(\theta - \phi)) \right] \cos(n\theta) R d\theta = n\pi \frac{\rho^{n-1}}{R^n} \cos(n\phi), & R \geq \rho \\ \int_0^{2\pi} \left[\sum_{m=1}^{\infty} m \frac{\rho^{m-1}}{R^{m+1}} \cos(m(\theta - \phi)) \right] \sin(n\theta) R d\theta = n\pi \frac{\rho^{n-1}}{R^n} \sin(n\phi), & R \geq \rho \\ \int_0^{2\pi} \left[\sum_{m=1}^{\infty} m \frac{R^{m-1}}{\rho^{m+1}} \cos(m(\theta - \phi)) \right] \cos(n\theta) R d\theta = n\pi \frac{R^n}{\rho^{n+1}} \cos(n\phi), & R < \rho \\ \int_0^{2\pi} \left[\sum_{m=1}^{\infty} m \frac{R^{m-1}}{\rho^{m+1}} \cos(m(\theta - \phi)) \right] \sin(n\theta) R d\theta = n\pi \frac{R^n}{\rho^{n+1}} \sin(n\phi), & R < \rho \end{cases}$
Limit $\rho \rightarrow R$	$\begin{cases} \lim_{\rho \rightarrow R} \left[-\pi \left(\frac{\rho}{R} \right)^{n-1} \cos(n\phi) \right] = -\pi \cos(n\phi), & R > \rho \\ \lim_{\rho \rightarrow R} \left[-\pi \left(\frac{\rho}{R} \right)^{n-1} \sin(n\phi) \right] = -\pi \sin(n\phi), & R > \rho \\ \lim_{\rho \rightarrow R} \left[\pi \left(\frac{R}{\rho} \right)^{n+1} \cos(n\phi) \right] = \pi \cos(n\phi), & R < \rho \\ \lim_{\rho \rightarrow R} \left[\pi \left(\frac{R}{\rho} \right)^{n+1} \sin(n\phi) \right] = \pi \sin(n\phi), & R < \rho \end{cases}$	$\begin{cases} \lim_{\rho \rightarrow R} \left[n\pi \frac{\rho^{n-1}}{R^n} \cos(n\phi) \right] = n\pi \frac{1}{R} \cos(n\phi), & R \geq \rho \\ \lim_{\rho \rightarrow R} \left[n\pi \frac{\rho^{n-1}}{R^n} \sin(n\phi) \right] = n\pi \frac{1}{R} \sin(n\phi), & R \geq \rho \\ \lim_{\rho \rightarrow R} \left[n\pi \frac{R^n}{\rho^{n+1}} \cos(n\phi) \right] = n\pi \frac{1}{R} \cos(n\phi), & R < \rho \\ \lim_{\rho \rightarrow R} \left[n\pi \frac{R^n}{\rho^{n+1}} \sin(n\phi) \right] = n\pi \frac{1}{R} \sin(n\phi), & R < \rho \end{cases}$
	(jump for $R^- < \rho < R^+$)	(Continuous for $R^- < \rho < R^+$)

Appendix Analytical evaluation of the integrals for Helmholtz kernels and their limit

$$U(s, x) \text{ and } \int_B U(s, x) t(s) dB(s)$$

Degenerate kernel

$$U(s, x) = \begin{cases} U^i(R, \theta; \rho, \phi) = \sum_{m=0}^{\infty} \frac{\pi}{2} \varepsilon_m J_m(k\rho) [Y_m(kR) - iJ_m(kR)] \cos(m(\theta - \phi)), & R > \rho \\ U^e(R, \theta; \rho, \phi) = \sum_{m=0}^{\infty} \frac{\pi}{2} \varepsilon_m J_m(kR) [Y_m(k\rho) - iJ_m(k\rho)] \cos(m(\theta - \phi)), & R < \rho \end{cases}$$

Orthogonal process for $n = 0$

$$\begin{cases} \int_0^{2\pi} \left[\sum_{m=0}^{\infty} \frac{\pi}{2} \varepsilon_m J_m(k\rho) [Y_m(kR) - iJ_m(kR)] \cos(m(\theta - \phi)) \right] \cos(0 \cdot \theta) R d\theta = R\pi^2 J_0(k\rho) [Y_0(kR) - iJ_0(kR)], & R \geq \rho \\ \int_0^{2\pi} \left[\sum_{m=0}^{\infty} \frac{\pi}{2} \varepsilon_m J_m(k\rho) [Y_m(kR) - iJ_m(kR)] \cos(m(\theta - \phi)) \right] \sin(0 \cdot \theta) R d\theta = 0, & R \geq \rho \\ \int_0^{2\pi} \left[\sum_{m=0}^{\infty} \frac{\pi}{2} \varepsilon_m J_m(kR) [Y_m(k\rho) - iJ_m(k\rho)] \cos(m(\theta - \phi)) \right] \cos(0 \cdot \theta) R d\theta = R\pi^2 J_0(kR) [Y_0(k\rho) - iJ_0(k\rho)], & R < \rho \\ \int_0^{2\pi} \left[\sum_{m=0}^{\infty} \frac{\pi}{2} \varepsilon_m J_m(kR) [Y_m(k\rho) - iJ_m(k\rho)] \cos(m(\theta - \phi)) \right] \sin(0 \cdot \theta) R d\theta = 0, & R < \rho \end{cases}$$

for $n \neq 0$

$$\begin{cases} \int_0^{2\pi} \left[\sum_{m=0}^{\infty} \frac{\pi}{2} \varepsilon_m J_m(k\rho) [Y_m(kR) - iJ_m(kR)] \cos(m(\theta - \phi)) \right] \cos(n\theta) R d\theta = R\pi^2 J_n(k\rho) [Y_n(kR) - iJ_n(kR)] \cos(n\phi), & R \geq \rho \\ \int_0^{2\pi} \left[\sum_{m=0}^{\infty} \frac{\pi}{2} \varepsilon_m J_m(k\rho) [Y_m(kR) - iJ_m(kR)] \cos(m(\theta - \phi)) \right] \sin(n\theta) R d\theta = R\pi^2 J_n(k\rho) [Y_n(kR) - iJ_n(kR)] \sin(n\phi), & R \geq \rho \\ \int_0^{2\pi} \left[\sum_{m=0}^{\infty} \frac{\pi}{2} \varepsilon_m J_m(kR) [Y_m(k\rho) - iJ_m(k\rho)] \cos(m(\theta - \phi)) \right] \cos(n\theta) R d\theta = R\pi^2 J_n(kR) [Y_n(k\rho) - iJ_n(k\rho)] \cos(n\phi), & R < \rho \\ \int_0^{2\pi} \left[\sum_{m=0}^{\infty} \frac{\pi}{2} \varepsilon_m J_m(kR) [Y_m(k\rho) - iJ_m(k\rho)] \cos(m(\theta - \phi)) \right] \sin(n\theta) R d\theta = R\pi^2 J_n(kR) [Y_n(k\rho) - iJ_n(k\rho)] \sin(n\phi), & R < \rho \end{cases}$$

Limit $\rho \rightarrow R$

for $n = 0$

$$\begin{cases} \lim_{\rho \rightarrow R} [R\pi^2 J_0(k\rho) [Y_0(kR) - iJ_0(kR)]] = R\pi^2 J_0(kR) [Y_0(kR) - iJ_0(kR)], & R \geq \rho \\ \lim_{\rho \rightarrow R} [R\pi^2 J_0(kR) [Y_0(k\rho) - iJ_0(k\rho)]] = R\pi^2 J_0(kR) [Y_0(kR) - iJ_0(kR)], & R < \rho \end{cases}$$

for $n \neq 0$

$$\begin{cases} \lim_{\rho \rightarrow R} [R\pi^2 J_n(k\rho) [Y_n(kR) - iJ_n(kR)] \cos(n\phi)] = R\pi^2 J_n(kR) [Y_n(kR) - iJ_n(kR)] \cos(n\phi), & R \geq \rho \\ \lim_{\rho \rightarrow R} [R\pi^2 J_n(k\rho) [Y_n(kR) - iJ_n(kR)] \sin(n\phi)] = R\pi^2 J_n(kR) [Y_n(kR) - iJ_n(kR)] \sin(n\phi), & R \geq \rho \\ \lim_{\rho \rightarrow R} [R\pi^2 J_n(kR) [Y_n(k\rho) - iJ_n(k\rho)] \cos(n\phi)] = R\pi^2 J_n(kR) [Y_n(kR) - iJ_n(kR)] \cos(n\phi), & R < \rho \\ \lim_{\rho \rightarrow R} [R\pi^2 J_n(kR) [Y_n(k\rho) - iJ_n(k\rho)] \sin(n\phi)] = R\pi^2 J_n(kR) [Y_n(kR) - iJ_n(kR)] \sin(n\phi), & R < \rho \end{cases}$$

(Continuous for $R^- < \rho < R^+$)

$$T(s, x) \text{ and } \int_B T(s, x) u(s) dB(s)$$

Degenerate kernel

$$T(s, x) = \begin{cases} T^i(R, \theta; \rho, \phi) = \sum_{m=0}^{\infty} k \frac{\pi}{2} \varepsilon_m J_m(k\rho) [Y'_m(kR) - iJ'_m(kR)] \cos(m(\theta - \phi)), & R > \rho \\ T^e(R, \theta; \rho, \phi) = \sum_{m=0}^{\infty} k \frac{\pi}{2} \varepsilon_m J'_m(kR) [Y_m(k\rho) - iJ_m(k\rho)] \cos(m(\theta - \phi)), & R < \rho \end{cases}$$

Orthogonal process for $n = 0$

$$\begin{cases} \int_0^{2\pi} \left[\sum_{m=0}^{\infty} k \frac{\pi}{2} \varepsilon_m J_m(k\rho) [Y'_m(kR) - iJ'_m(kR)] \cos(m(\theta - \phi)) \right] \cos(0 \cdot \theta) R d\theta = kR\pi^2 J_0(k\rho) [Y'_0(kR) - iJ'_0(kR)], & R > \rho \\ \int_0^{2\pi} \left[\sum_{m=0}^{\infty} k \frac{\pi}{2} \varepsilon_m J_m(k\rho) [Y'_m(kR) - iJ'_m(kR)] \cos(m(\theta - \phi)) \right] \sin(0 \cdot \theta) R d\theta = 0, & R > \rho \\ \int_0^{2\pi} \left[\sum_{m=0}^{\infty} k \frac{\pi}{2} \varepsilon_m J'_m(kR) [Y_m(k\rho) - iJ_m(k\rho)] \cos(m(\theta - \phi)) \right] \cos(0 \cdot \theta) R d\theta = kR\pi^2 J'_0(kR) [Y_0(k\rho) - iJ_0(k\rho)], & R < \rho \\ \int_0^{2\pi} \left[\sum_{m=0}^{\infty} k \frac{\pi}{2} \varepsilon_m J'_m(kR) [Y_m(k\rho) - iJ_m(k\rho)] \cos(m(\theta - \phi)) \right] \sin(0 \cdot \theta) R d\theta = 0, & R < \rho \end{cases}$$

for $n \neq 0$

$$\begin{cases} \int_0^{2\pi} \left[\sum_{m=0}^{\infty} k \frac{\pi}{2} \varepsilon_m J_m(k\rho) [Y'_m(kR) - iJ'_m(kR)] \cos(m(\theta - \phi)) \right] \cos(n \cdot \theta) R d\theta = kR\pi^2 J_n(k\rho) [Y'_n(kR) - iJ'_n(kR)] \cos(n\phi), & R > \rho \\ \int_0^{2\pi} \left[\sum_{m=0}^{\infty} k \frac{\pi}{2} \varepsilon_m J_m(k\rho) [Y'_m(kR) - iJ'_m(kR)] \cos(m(\theta - \phi)) \right] \sin(n \cdot \theta) R d\theta = kR\pi^2 J_n(k\rho) [Y'_n(kR) - iJ'_n(kR)] \sin(n\phi), & R > \rho \\ \int_0^{2\pi} \left[\sum_{m=0}^{\infty} k \frac{\pi}{2} \varepsilon_m J'_m(kR) [Y_m(k\rho) - iJ_m(k\rho)] \cos(m(\theta - \phi)) \right] \cos(n \cdot \theta) R d\theta = kR\pi^2 J'_n(kR) [Y_n(k\rho) - iJ_n(k\rho)] \cos(n\phi), & R < \rho \\ \int_0^{2\pi} \left[\sum_{m=0}^{\infty} k \frac{\pi}{2} \varepsilon_m J'_m(kR) [Y_m(k\rho) - iJ_m(k\rho)] \cos(m(\theta - \phi)) \right] \sin(n \cdot \theta) R d\theta = kR\pi^2 J'_n(kR) [Y_n(k\rho) - iJ_n(k\rho)] \sin(n\phi), & R < \rho \end{cases}$$

Limit $\rho \rightarrow R$

for $n = 0$

$$\begin{cases} \lim_{\rho \rightarrow R} [kR\pi^2 J_0(k\rho) [Y_0'(kR) - iJ_0'(kR)]] = kR\pi^2 J_0(k\rho) [Y_0'(kR) - iJ_0'(kR)], & R > \rho \\ \lim_{\rho \rightarrow R} [kR\pi^2 J_0'(kR) [Y_0(k\rho) - iJ_0(k\rho)]] = kR\pi^2 J_0'(kR) [Y_0(k\rho) - iJ_0(k\rho)], & R < \rho \end{cases}$$

for $n \neq 0$

$$\begin{cases} \lim_{\rho \rightarrow R} [kR\pi^2 J_n(k\rho) [Y_n'(kR) - iJ_n'(kR)] \cos(n\phi)] = kR\pi^2 J_n(kR) [Y_n'(kR) - iJ_n'(kR)] \cos(n\phi), & R > \rho \\ \lim_{\rho \rightarrow R} [kR\pi^2 J_n(k\rho) [Y_n'(kR) - iJ_n'(kR)] \sin(n\phi)] = kR\pi^2 J_n(kR) [Y_n'(kR) - iJ_n'(kR)] \sin(n\phi), & R > \rho \\ \lim_{\rho \rightarrow R} [kR\pi^2 J_n'(kR) [Y_n(k\rho) - iJ_n(k\rho)] \cos(n\phi)] = kR\pi^2 J_n'(kR) [Y_n(kR) - iJ_n(kR)] \cos(n\phi), & R < \rho \\ \lim_{\rho \rightarrow R} [kR\pi^2 J_n'(kR) [Y_n(k\rho) - iJ_n(k\rho)] \sin(n\phi)] = kR\pi^2 J_n'(kR) [Y_n(kR) - iJ_n(kR)] \sin(n\phi), & R < \rho \end{cases}$$

(jump for $R^- < \rho < R^+$)

$$L(s, x) \text{ and } \int_B L(s, x) t(s) dB(s)$$

Degenerate kernel

$$L(s, x) = \begin{cases} L^i(R, \theta; \rho, \phi) = \sum_{m=0}^{\infty} k \frac{\pi}{2} \varepsilon_m J'_m(k\rho) [Y_m(kR) - iJ_m(kR)] \cos(m(\theta - \phi)), & R > \rho \\ L^e(R, \theta; \rho, \phi) = \sum_{m=0}^{\infty} k \frac{\pi}{2} \varepsilon_m J_m(kR) [Y'_m(k\rho) - iJ'_m(k\rho)] \cos(m(\theta - \phi)), & R < \rho \end{cases}$$

Orthogonal process for $n = 0$

$$\begin{cases} \int_0^{2\pi} \left[\sum_{m=0}^{\infty} k \frac{\pi}{2} \varepsilon_m J'_m(k\rho) [Y_m(kR) - iJ_m(kR)] \cos(m(\theta - \phi)) \right] \cos(0 \cdot \phi) R d\theta = kR\pi^2 J'_0(k\rho) [Y_0(kR) - iJ_0(kR)], & R > \rho \\ \int_0^{2\pi} \left[\sum_{m=0}^{\infty} k \frac{\pi}{2} \varepsilon_m J'_m(k\rho) [Y_m(kR) - iJ_m(kR)] \sin(m(\theta - \phi)) \right] \sin(0 \cdot \phi) R d\theta = 0, & R > \rho \\ \int_0^{2\pi} \left[\sum_{m=0}^{\infty} k \frac{\pi}{2} \varepsilon_m J_m(kR) [Y'_m(k\rho) - iJ'_m(k\rho)] \cos(m(\theta - \phi)) \right] \cos(0 \cdot \phi) R d\theta = kR\pi^2 J_0(kR) [Y'_0(k\rho) - iJ'_0(k\rho)], & R < \rho \\ \int_0^{2\pi} \left[\sum_{m=0}^{\infty} k \frac{\pi}{2} \varepsilon_m J_m(kR) [Y'_m(k\rho) - iJ'_m(k\rho)] \sin(m(\theta - \phi)) \right] \sin(0 \cdot \phi) R d\theta = 0, & R < \rho \end{cases}$$

for $n \neq 0$

$$\begin{cases} \int_0^{2\pi} \left[\sum_{m=0}^{\infty} k \frac{\pi}{2} \varepsilon_m J'_m(k\rho) [Y_m(kR) - iJ_m(kR)] \cos(m(\theta - \phi)) \right] \cos(n\phi) R d\theta = kR\pi^2 J'_n(k\rho) [Y_n(kR) - iJ_n(kR)] \cos(n\phi), & R > \rho \\ \int_0^{2\pi} \left[\sum_{m=0}^{\infty} k \frac{\pi}{2} \varepsilon_m J'_m(k\rho) [Y_m(kR) - iJ_m(kR)] \sin(m(\theta - \phi)) \right] \sin(n\phi) R d\theta = kR\pi^2 J'_n(k\rho) [Y_n(kR) - iJ_n(kR)] \sin(n\phi), & R > \rho \\ \int_0^{2\pi} \left[\sum_{m=0}^{\infty} k \frac{\pi}{2} \varepsilon_m J_m(kR) [Y'_m(k\rho) - iJ'_m(k\rho)] \cos(m(\theta - \phi)) \right] \cos(n\phi) R d\theta = kR\pi^2 J_n(kR) [Y'_n(k\rho) - iJ'_n(k\rho)] \cos(n\phi), & R < \rho \\ \int_0^{2\pi} \left[\sum_{m=0}^{\infty} k \frac{\pi}{2} \varepsilon_m J_m(kR) [Y'_m(k\rho) - iJ'_m(k\rho)] \sin(m(\theta - \phi)) \right] \sin(n\phi) R d\theta = kR\pi^2 J_n(kR) [Y'_n(k\rho) - iJ'_n(k\rho)] \sin(n\phi), & R < \rho \end{cases}$$

Limit $\rho \rightarrow R$

for $n = 0$

$$\begin{cases} \lim_{\rho \rightarrow R} [kR\pi^2 J'_0(k\rho) [Y_0(kR) - iJ_0(kR)]] = kR\pi^2 J'_0(kR) [Y_0(kR) - iJ_0(kR)], & R > \rho \\ \lim_{\rho \rightarrow R} [kR\pi^2 J_0(kR) [Y'_0(k\rho) - iJ'_0(k\rho)]] = kR\pi^2 J_0(kR) [Y'_0(kR) - iJ'_0(kR)], & R < \rho \end{cases}$$

for $n \neq 0$

$$\begin{cases} \lim_{\rho \rightarrow R} [kR\pi^2 J'_n(k\rho) [Y_n(kR) - iJ_n(kR)] \cos(n\phi)] = kR\pi^2 J'_n(kR) [Y_n(kR) - iJ_n(kR)] \cos(n\phi), & R > \rho \\ \lim_{\rho \rightarrow R} [kR\pi^2 J'_n(k\rho) [Y_n(kR) - iJ_n(kR)] \sin(n\phi)] = kR\pi^2 J'_n(kR) [Y_n(kR) - iJ_n(kR)] \sin(n\phi), & R > \rho \\ \lim_{\rho \rightarrow R} [kR\pi^2 J_n(kR) [Y'_n(k\rho) - iJ'_n(k\rho)] \cos(n\phi)] = kR\pi^2 J_n(kR) [Y'_n(kR) - iJ'_n(kR)] \cos(n\phi), & R < \rho \\ \lim_{\rho \rightarrow R} [kR\pi^2 J_n(kR) [Y'_n(k\rho) - iJ'_n(k\rho)] \sin(n\phi)] = kR\pi^2 J_n(kR) [Y'_n(kR) - iJ'_n(kR)] \sin(n\phi), & R < \rho \end{cases}$$

(jump for $R^- < \rho < R^+$)

$$M(s, x) \text{ and } \int_B M(s, x) u(s) dB(s)$$

Degenerate kernel

$$M(s, x) = \begin{cases} M^i(R, \theta; \rho, \phi) = \sum_{m=0}^{\infty} k^2 \frac{\pi}{2} \varepsilon_m J'_m(k\rho) [Y'_m(kR) - iJ'_m(kR)] \cos(m(\theta - \phi)), & R \geq \rho \\ M^e(R, \theta; \rho, \phi) = \sum_{m=0}^{\infty} k^2 \frac{\pi}{2} \varepsilon_m J'_m(kR) [Y'_m(k\rho) - iJ'_m(k\rho)] \cos(m(\theta - \phi)), & R < \rho \end{cases}$$

Orthogonal process for $n = 0$

$$\begin{cases} \int_0^{2\pi} \left[\sum_{m=0}^{\infty} k^2 \frac{\pi}{2} \varepsilon_m J'_m(k\rho) [Y'_m(kR) - iJ'_m(kR)] \cos(m(\theta - \phi)) \right] \cos(0 \cdot \phi) R d\theta = k^2 R \pi^2 J'_0(k\rho) [Y'_0(kR) - iJ'_0(kR)], & R \geq \rho \\ \int_0^{2\pi} \left[\sum_{m=0}^{\infty} k^2 \frac{\pi}{2} \varepsilon_m J'_m(k\rho) [Y'_m(kR) - iJ'_m(kR)] \cos(m(\theta - \phi)) \right] \sin(0 \cdot \phi) R d\theta = 0, & R \geq \rho \\ \int_0^{2\pi} \left[\sum_{m=0}^{\infty} k^2 \frac{\pi}{2} \varepsilon_m J'_m(kR) [Y'_m(k\rho) - iJ'_m(k\rho)] \cos(m(\theta - \phi)) \right] \cos(0 \cdot \phi) R d\theta = k^2 R \pi^2 J'_0(kR) [Y'_0(k\rho) - iJ'_0(k\rho)], & R < \rho \\ \int_0^{2\pi} \left[\sum_{m=0}^{\infty} k^2 \frac{\pi}{2} \varepsilon_m J'_m(kR) [Y'_m(k\rho) - iJ'_m(k\rho)] \cos(m(\theta - \phi)) \right] \sin(0 \cdot \phi) R d\theta = 0, & R < \rho \end{cases}$$

for $n \neq 0$

$$\begin{cases} \int_0^{2\pi} \left[\sum_{m=0}^{\infty} k^2 \frac{\pi}{2} \varepsilon_m J'_m(k\rho) [Y'_m(kR) - iJ'_m(kR)] \cos(m(\theta - \phi)) \right] \cos(n\phi) R d\theta = k^2 R \pi^2 J'_n(k\rho) [Y'_n(kR) - iJ'_n(kR)] \cos(n\phi), & R \geq \rho \\ \int_0^{2\pi} \left[\sum_{m=0}^{\infty} k^2 \frac{\pi}{2} \varepsilon_m J'_m(k\rho) [Y'_m(kR) - iJ'_m(kR)] \cos(m(\theta - \phi)) \right] \sin(n\phi) R d\theta = k^2 R \pi^2 J'_n(k\rho) [Y'_n(kR) - iJ'_n(kR)] \sin(n\phi), & R \geq \rho \\ \int_0^{2\pi} \left[\sum_{m=0}^{\infty} k^2 \frac{\pi}{2} \varepsilon_m J'_m(kR) [Y'_m(k\rho) - iJ'_m(k\rho)] \cos(m(\theta - \phi)) \right] \cos(n\phi) R d\theta = k^2 R \pi^2 J'_n(kR) [Y'_n(k\rho) - iJ'_n(k\rho)] \cos(n\phi), & R < \rho \\ \int_0^{2\pi} \left[\sum_{m=0}^{\infty} k^2 \frac{\pi}{2} \varepsilon_m J'_m(kR) [Y'_m(k\rho) - iJ'_m(k\rho)] \cos(m(\theta - \phi)) \right] \sin(n\phi) R d\theta = k^2 R \pi^2 J'_n(kR) [Y'_n(k\rho) - iJ'_n(k\rho)] \sin(n\phi), & R < \rho \end{cases}$$

Limit $\rho \rightarrow R$

for $n = 0$

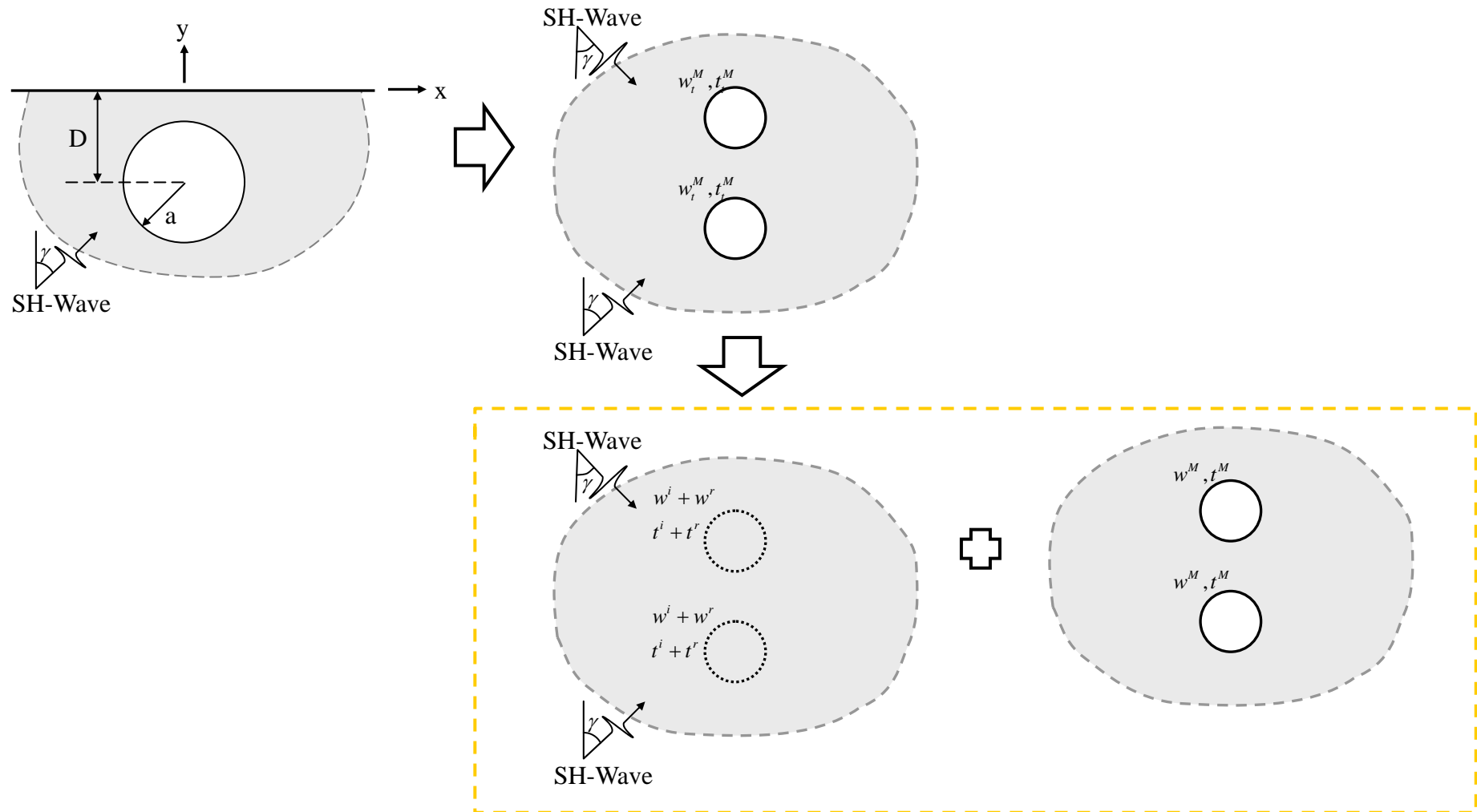
$$\begin{cases} \lim_{\rho \rightarrow R^-} \left[k^2 R \pi^2 J'_0(k\rho) \left[Y'_0(kR) - iJ'_0(kR) \right] \right] = k^2 R \pi^2 J'_0(kR) \left[Y'_0(kR) - iJ'_0(kR) \right], & R \geq \rho \\ \lim_{\rho \rightarrow R^+} \left[k^2 R \pi^2 J'_0(kR) \left[Y'_0(k\rho) - iJ'_0(k\rho) \right] \right] = k^2 R \pi^2 J'_0(kR) \left[Y'_0(kR) - iJ'_0(kR) \right], & R < \rho \end{cases}$$

for $n \neq 0$

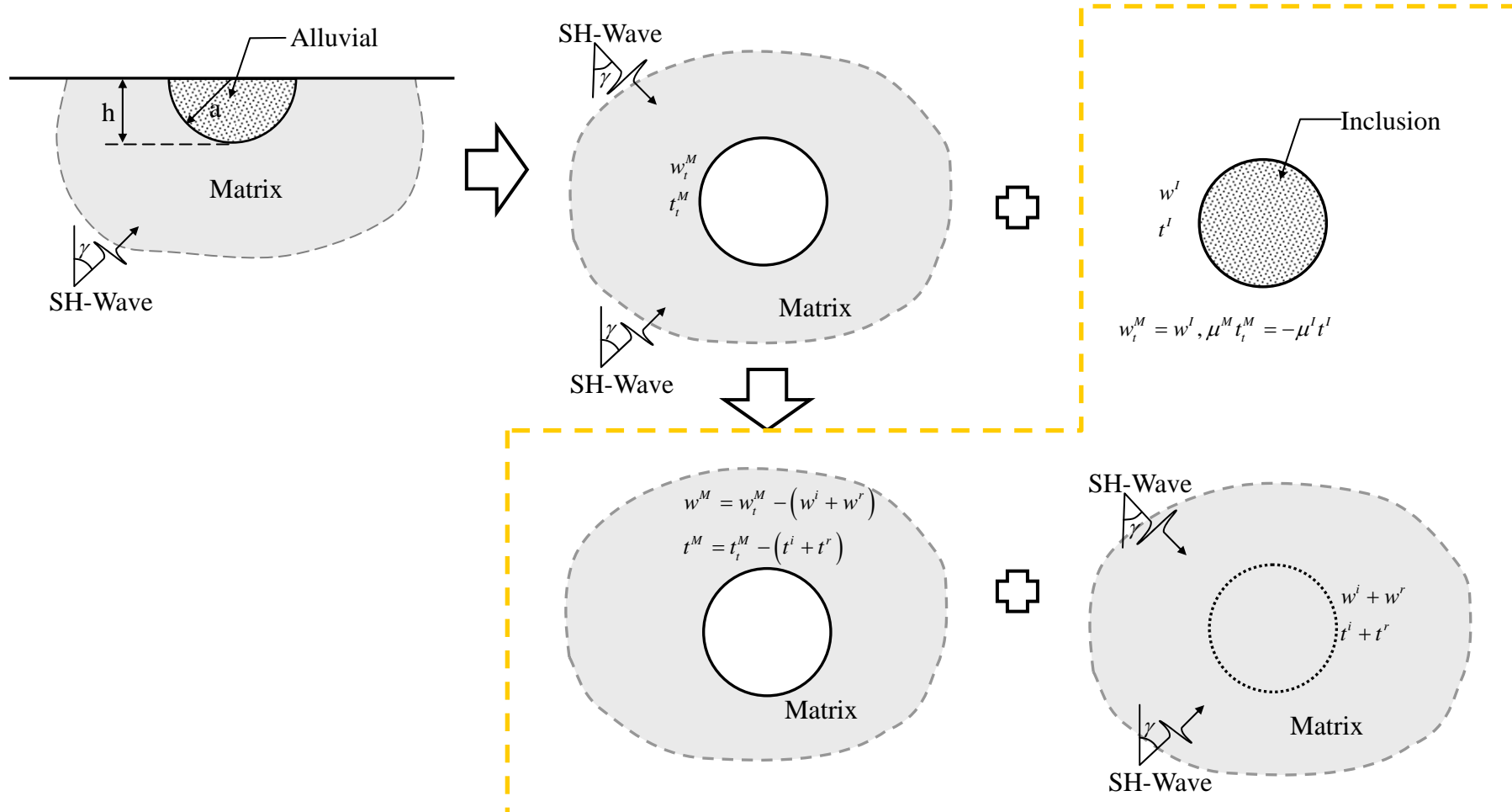
$$\begin{cases} \lim_{\rho \rightarrow R^-} \left[k^2 R \pi^2 J'_n(k\rho) \left[Y'_n(kR) - iJ'_n(kR) \right] \cos(n\phi) \right] = k^2 R \pi^2 J'_n(kR) \left[Y'_n(kR) - iJ'_n(kR) \right] \cos(n\phi), & R \geq \rho \\ \lim_{\rho \rightarrow R^-} \left[k^2 R \pi^2 J'_n(k\rho) \left[Y'_n(kR) - iJ'_n(kR) \right] \sin(n\phi) \right] = k^2 R \pi^2 J'_n(kR) \left[Y'_n(kR) - iJ'_n(kR) \right] \sin(n\phi), & R \geq \rho \\ \lim_{\rho \rightarrow R^+} \left[k^2 R \pi^2 J'_n(kR) \left[Y'_n(k\rho) - iJ'_n(k\rho) \right] \cos(n\phi) \right] = k^2 R \pi^2 J'_n(kR) \left[Y'_n(kR) - iJ'_n(kR) \right] \cos(n\phi), & R < \rho \\ \lim_{\rho \rightarrow R^+} \left[k^2 R \pi^2 J'_n(kR) \left[Y'_n(k\rho) - iJ'_n(k\rho) \right] \sin(n\phi) \right] = k^2 R \pi^2 J'_n(kR) \left[Y'_n(kR) - iJ'_n(kR) \right] \sin(n\phi), & R < \rho \end{cases}$$

(Continuous for $R^- < \rho < R^+$)

Appendix Image concept and the decomposition of superposition of a circular cavity



Appendix Image concept and the decomposition of superposition of a alluvial valley



Appendix Limiting process of the annular Green's function to an exterior case by setting $b \rightarrow \infty$.

$G(x, \xi)$ for $a \leq \rho \leq R_\xi$

Annular Green's function

$$G(x, \xi) = -(b \ln b \, p_0 + a \ln \rho \, \bar{p}_0 - \frac{\ln R_\xi}{2\pi}) + \sum_{m=1}^{\infty} \frac{1}{2m} \left[\left(b \left(\frac{\rho}{b} \right)^m p_m + a \left(\frac{a}{\rho} \right)^m \bar{p}_m - \left(\frac{\rho}{R_\xi} \right)^m \frac{\cos m\theta_\xi}{\pi} \cos m\phi + \left(b \left(\frac{\rho}{b} \right)^m q_m + a \left(\frac{a}{\rho} \right)^m \bar{q}_m - \left(\frac{\rho}{R_\xi} \right)^m \frac{\sin m\theta_\xi}{\pi} \sin m\phi \right] \right.$$

$$= -(b \ln b \frac{\ln a - \ln R_\xi}{2\pi b (\ln a - \ln b)} + a \ln \rho \frac{\ln b - \ln R_\xi}{2\pi a (\ln b - \ln a)} - \frac{\ln R_\xi}{2\pi}) \sum_{m=1}^{\infty} \frac{1}{2m} \left(b \left(\frac{\rho}{b} \right)^m \frac{b^{m-1} [b^m \left(\frac{R_\xi}{b} \right)^m - a^m \left(\frac{a}{R_\xi} \right)^m]}{(b^{2m} - a^{2m})\pi} + a \left(\frac{a}{\rho} \right)^m \frac{b^m [b^m \left(\frac{a}{R_\xi} \right)^m - a^m \left(\frac{R_\xi}{b} \right)^m]}{a(b^{2m} - a^{2m})\pi} - \left(\frac{\rho}{\pi R_\xi} \right)^m \cos m(\phi - \theta_\xi) \right)$$

Limiting process

$$\lim_{b \rightarrow \infty} G(x, \xi) = -(\not{b} \ln b \frac{\ln a - \ln R_\xi}{2\pi \not{b} (\ln a - \ln b)} + \not{a} \ln \rho \frac{\ln b - \ln R_\xi}{2\pi \not{a} (\ln b - \ln \not{a})} - \frac{\ln R_\xi}{2\pi}) + \sum_{m=1}^{\infty} \frac{1}{2m} \left[\left(b \left(\frac{\rho}{b} \right)^m \frac{b^{m-1} [b^m \left(\frac{R_\xi}{b} \right)^m - a^m \left(\frac{a}{R_\xi} \right)^m]}{(b^{2m} - a^{2m})\pi} + \not{a} \left(\frac{a}{\rho} \right)^m \frac{b^m [b^m \left(\frac{a}{R_\xi} \right)^m - a^m \left(\frac{R_\xi}{b} \right)^m]}{\not{a} (b^{2m} - a^{2m})\pi} - \left(\frac{\rho}{\pi R_\xi} \right)^m \cos m(\phi - \theta_\xi) \right]$$

$$= -(\ln b \frac{\ln a - \ln R_\xi}{2\pi (\ln \not{a} - \ln b)} + \ln \rho \frac{\ln b - \ln R_\xi}{2\pi (\ln b - \ln \not{a})} - \frac{\ln R_\xi}{2\pi}) + \sum_{m=1}^{\infty} \frac{1}{2m} \left[\left(\frac{\rho^m \not{b}^m [b^m \left(\frac{R_\xi}{b} \right)^m - \not{a}^m \left(\frac{a}{R_\xi} \right)^m]}{\not{b}^m (b^{2m} - \not{a}^{2m})\pi} + \frac{a^m b^m [b^m \left(\frac{a}{R_\xi} \right)^m - \not{a}^m \left(\frac{R_\xi}{b} \right)^m]}{\rho^m (b^{2m} - \not{a}^{2m})\pi} - \left(\frac{\rho}{\pi R_\xi} \right)^m \cos m(\phi - \theta_\xi) \right]$$

$$= -(\ln \not{b} \frac{\ln a - \ln R_\xi}{-2\pi \ln \not{b}} + a \ln \rho \frac{\ln \not{b}}{2\pi a \ln \not{b}} - \frac{\ln R_\xi}{2\pi}) + \sum_{m=1}^{\infty} \frac{1}{2m} \left[\left(\frac{\rho^m \not{b}^m \left(\frac{R_\xi}{\not{b}} \right)^m}{b^{2m} \pi} + \frac{a^m \not{b}^m \not{b}^m \left(\frac{a}{R_\xi} \right)^m}{\rho^m \not{b}^{2m} \pi} - \left(\frac{\rho}{\pi R_\xi} \right)^m \cos m(\phi - \theta_\xi) \right]$$

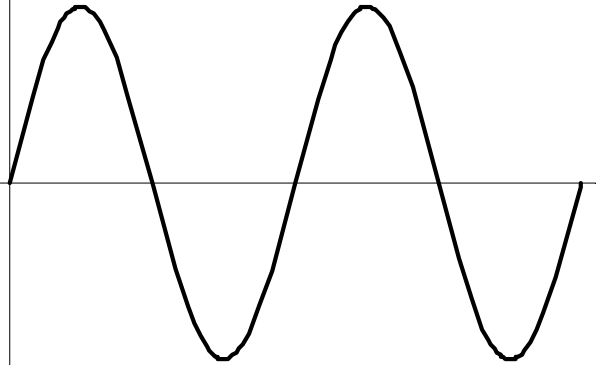
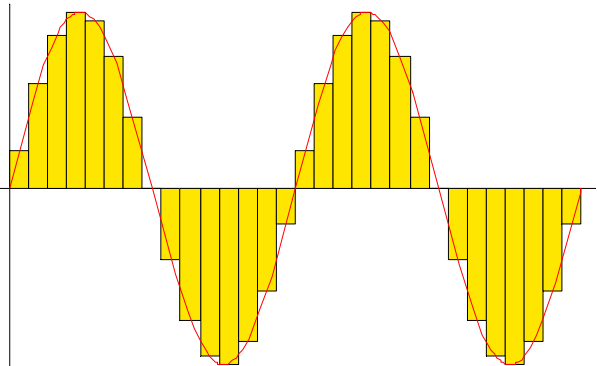
$$= -\left(-\frac{\ln a - \ln R_\xi}{2\pi} + \frac{\ln \rho}{2\pi} - \frac{\ln R_\xi}{2\pi} \right) + \sum_{m=1}^{\infty} \frac{1}{2m} \left[\left(\frac{\rho^m R_\xi^m}{b^{2m} \pi} + \frac{\left(\frac{a^2}{R_\xi} \right)^m}{\rho^m \pi} - \left(\frac{\rho}{\pi R_\xi} \right)^m \cos m(\phi - \theta_\xi) \right] \right]$$

$$= -\left(-\frac{\ln a}{2\pi} + \frac{\ln \rho}{2\pi} \right) + \sum_{m=1}^{\infty} \frac{1}{2m} \left[\left(0 + \frac{\left(\frac{a^2}{R_\xi} \right)^m}{\rho^m \pi} - \left(\frac{\rho}{\pi R_\xi} \right)^m \cos m(\phi - \theta_\xi) \right] \right]$$

$$= \frac{1}{2\pi} \left\{ \frac{\ln a}{\ln \rho} - \sum_{m=1}^{\infty} \frac{1}{m} \left[\left(\frac{\rho}{R_\xi} \right)^m - \left(\frac{a^2}{\rho^m R_\xi} \right)^m \right] \cos m(\phi - \theta_\xi) \right\}$$

$G(x, \xi)$ for $R_\xi \leq \rho \leq b$	
Annular Green's function	$G(x, \xi) = -(b \ln b p_0 + a \ln \rho \bar{p}_0 - \frac{\ln \rho}{2\pi}) + \sum_{m=1}^{\infty} \frac{1}{2m} [(b \left(\frac{\rho}{b}\right)^m p_m + a \left(\frac{a}{\rho}\right)^m \bar{p}_m - \left(\frac{R_\xi}{\rho}\right)^m \frac{\cos m\theta_\xi}{\pi}) \cos m\phi + (b \left(\frac{\rho}{b}\right)^m q_m + a \left(\frac{a}{\rho}\right)^m \bar{q}_m - \left(\frac{R_\xi}{\rho}\right)^m \frac{\sin m\theta_\xi}{\pi}) \sin m\phi]$ $= -(b \ln b \frac{\ln a - \ln R_\xi}{2\pi b (\ln a - \ln b)} + a \ln \rho \frac{\ln b - \ln R_\xi}{2\pi a (\ln b - \ln a)} - \frac{\ln \rho}{2\pi}) + \sum_{m=1}^{\infty} \frac{1}{2m} [(b \left(\frac{\rho}{b}\right)^m \frac{b^{m-1} [b^m \left(\frac{R_\xi}{b}\right)^m - a^m \left(\frac{a}{R_\xi}\right)^m]}{(b^{2m} - a^{2m})\pi} + a \left(\frac{a}{\rho}\right)^m \frac{b^m [b^m \left(\frac{a}{R_\xi}\right)^m - a^m \left(\frac{R_\xi}{b}\right)^m]}{a(b^{2m} - a^{2m})\pi} - \left(\frac{R_\xi}{\rho}\right)^m) \cos m(\phi - \theta_\xi)]$
Limiting process	$\lim_{b \rightarrow \infty} G(x, \xi) = -(\not{b} \ln b \frac{\ln a - \ln R_\xi}{2\pi \not{b} (\ln a - \ln b)} + \not{a} \ln \rho \frac{\ln b - \ln R_\xi}{2\pi \not{a} (\ln b - \ln a)} - \frac{\ln \rho}{2\pi}) + \sum_{m=1}^{\infty} \frac{1}{2m} [(b \left(\frac{\rho}{b}\right)^m \frac{b^{m-1} [b^m \left(\frac{R_\xi}{b}\right)^m - a^m \left(\frac{a}{R_\xi}\right)^m]}{(b^{2m} - a^{2m})\pi} + \not{a} \left(\frac{a}{\rho}\right)^m \frac{b^m [b^m \left(\frac{a}{R_\xi}\right)^m - a^m \left(\frac{R_\xi}{b}\right)^m]}{\not{a}(b^{2m} - a^{2m})\pi} - \left(\frac{R_\xi}{\pi \rho}\right)^m) \cos m(\phi - \theta_\xi)]$ $= -(\ln b \frac{\ln a - \ln R_\xi}{2\pi (\ln \not{a} - \ln b)} + \ln \rho \frac{\ln b - \ln \not{R}_\xi}{2\pi (\ln b - \ln \not{a})} - \frac{\ln \rho}{2\pi}) + \sum_{m=1}^{\infty} \frac{1}{2m} [(\frac{\rho^m \not{b}^m [b^m \left(\frac{R_\xi}{b}\right)^m - \not{a}^m \left(\frac{a}{R_\xi}\right)^m]}{\not{b}^m (b^{2m} - \not{a}^{2m})\pi} + \frac{a^m b^m [b^m \left(\frac{a}{R_\xi}\right)^m - \not{a}^m \left(\frac{R_\xi}{b}\right)^m]}{\rho^m (b^{2m} - \not{a}^{2m})\pi} - \left(\frac{R_\xi}{\pi \rho}\right)^m) \cos m(\phi - \theta_\xi)]$ $= -(\ln \not{b} \frac{\ln a - \ln R_\xi}{-2\pi \ln \not{b}} + \ln \rho \frac{\ln \not{b}}{2\pi \ln \not{b}} - \frac{\ln \rho}{2\pi}) + \sum_{m=1}^{\infty} \frac{1}{2m} [(\frac{\rho^m \not{b}^m \left(\frac{R_\xi}{\not{b}}\right)^m}{b^{2m} \pi} + \frac{a^m \not{b}^m \not{b}^m \left(\frac{a}{R_\xi}\right)^m}{\rho^m \not{b}^{2m} \pi} - \left(\frac{R_\xi}{\pi \rho}\right)^m) \cos m(\phi - \theta_\xi)]$ $= -(\frac{\ln a - \ln R_\xi}{2\pi} + \frac{\ln \rho}{2\pi} - \frac{\ln \rho}{2\pi}) + \sum_{m=1}^{\infty} \frac{1}{2m} [(\frac{\rho^m R_\xi^m}{b^{2m} \pi} + \frac{\left(\frac{a^2}{R_\xi}\right)^m}{\rho^m \pi} - \left(\frac{R_\xi}{\pi \rho}\right)^m) \cos m(\phi - \theta_\xi)]$ $= -(\frac{\ln a - \ln R_\xi}{2\pi}) + \sum_{m=1}^{\infty} \frac{1}{2m} [(0 + \frac{\left(\frac{a^2}{R_\xi}\right)^m}{\rho^m \pi} - \left(\frac{R_\xi}{\pi \rho}\right)^m) \cos m(\phi - \theta_\xi)]$ $= \frac{1}{2\pi} \{ \ln \frac{a}{R_\xi} - \sum_{m=1}^{\infty} \frac{1}{m} [\left(\frac{R_\xi}{\rho}\right)^m - \left(\frac{a^2}{\rho R_\xi}\right)^m] \cos m(\phi - \theta_\xi) \}$

Table 1-1 Comparisons of the present method and conventional BEM.

	Boundary density discretization	Auxiliary system	Formulation	Observer system	Singularity
Present method	<p>Fourier series</p> 	Degenerate kernel	Null-field integral equation	Adaptive observer system	No principal value
Conventional BEM	<p>Constant element</p> 	Fundamental solution	Boundary integral equation	Fixed observer system	Principal value (CPV, RPV and HPV)

where CPV, RPV and HPV are the Cauchy principal value, Riemann principal value and Hadamard principal value, respectively.

Conventional BEM fundamental solution-closed form		
Primary field	$2\pi u(\mathbf{x}) = \int_B T(\mathbf{s}, \mathbf{x}) u(\mathbf{s}) dB(\mathbf{s}) - \int_B U(\mathbf{s}, \mathbf{x}) t(\mathbf{s}) dB(\mathbf{s}), \quad \mathbf{x} \in \Omega$	
	$\pi u(\mathbf{x}) = C.P.V. \int_B T(\mathbf{s}, \mathbf{x}) u(\mathbf{s}) dB(\mathbf{s}) - R.P.V. \int_B U(\mathbf{s}, \mathbf{x}) t(\mathbf{s}) dB(\mathbf{s}), \quad \mathbf{x} \in B$	
	$0 = \int_B T(\mathbf{s}, \mathbf{x}) u(\mathbf{s}) dB(\mathbf{s}) - \int_B U(\mathbf{s}, \mathbf{x}) t(\mathbf{s}) dB(\mathbf{s}), \quad \mathbf{x} \in \Omega^c$	
Secondary field	$2\pi \frac{\partial u(\mathbf{x})}{\partial \mathbf{n}_x} = \int_B M(\mathbf{s}, \mathbf{x}) u(\mathbf{s}) dB(\mathbf{s}) - \int_B L(\mathbf{s}, \mathbf{x}) t(\mathbf{s}) dB(\mathbf{s}), \quad \mathbf{x} \in \Omega$	
	$\pi \frac{\partial u(\mathbf{x})}{\partial \mathbf{n}_x} = H.P.V. \int_B M(\mathbf{s}, \mathbf{x}) u(\mathbf{s}) dB(\mathbf{s}) - C.P.V. \int_B L(\mathbf{s}, \mathbf{x}) t(\mathbf{s}) dB(\mathbf{s}), \quad \mathbf{x} \in B$	
	$0 = \int_B M(\mathbf{s}, \mathbf{x}) u(\mathbf{s}) dB(\mathbf{s}) - \int_B L(\mathbf{s}, \mathbf{x}) t(\mathbf{s}) dB(\mathbf{s}), \quad \mathbf{x} \in \Omega^c$	
Present formulation (degenerate kernel-series form)		
	Interior problem	Exterior problem
Primary field	$2\pi u(\mathbf{x}) = \int_B T^i(\mathbf{s}, \mathbf{x}) u(\mathbf{s}) dB(\mathbf{s}) - \int_B U^i(\mathbf{s}, \mathbf{x}) t(\mathbf{s}) dB(\mathbf{s}), \quad \mathbf{x} \in \Omega \cup B$	$2\pi u(\mathbf{x}) = \int_B T^e(\mathbf{s}, \mathbf{x}) u(\mathbf{s}) dB(\mathbf{s}) - \int_B U^e(\mathbf{s}, \mathbf{x}) t(\mathbf{s}) dB(\mathbf{s}), \quad \mathbf{x} \in \Omega \cup B$
	NA, $\mathbf{x} \in B$	NA, $\mathbf{x} \in B$
	$0 = \int_B T^e(\mathbf{s}, \mathbf{x}) u(\mathbf{s}) dB(\mathbf{s}) - \int_B U^e(\mathbf{s}, \mathbf{x}) t(\mathbf{s}) dB(\mathbf{s}), \quad \mathbf{x} \in \Omega^c \cup B$	$0 = \int_B T^i(\mathbf{s}, \mathbf{x}) u(\mathbf{s}) dB(\mathbf{s}) - \int_B U^i(\mathbf{s}, \mathbf{x}) t(\mathbf{s}) dB(\mathbf{s}), \quad \mathbf{x} \in \Omega^c \cup B$

Secondary field	$2\pi \frac{\partial u(\mathbf{x})}{\partial \mathbf{n}_x} = \int_B M^i(\mathbf{s}, \mathbf{x}) u(\mathbf{s}) dB(\mathbf{s}) - \int_B L^i(\mathbf{s}, \mathbf{x}) t(\mathbf{s}) dB(\mathbf{s}), \quad \mathbf{x} \in \Omega \cup B$	$2\pi \frac{\partial u(\mathbf{x})}{\partial \mathbf{n}_x} = \int_B M^e(\mathbf{s}, \mathbf{x}) u(\mathbf{s}) dB(\mathbf{s}) - \int_B L^e(\mathbf{s}, \mathbf{x}) t(\mathbf{s}) dB(\mathbf{s}), \quad \mathbf{x} \in \Omega \cup B$
	NA, $\mathbf{x} \in B$	NA, $\mathbf{x} \in B$
	$0 = \int_B M^e(\mathbf{s}, \mathbf{x}) u(\mathbf{s}) dB(\mathbf{s}) - \int_B L^e(\mathbf{s}, \mathbf{x}) t(\mathbf{s}) dB(\mathbf{s}), \quad \mathbf{x} \in \Omega^c \cup B$	$0 = \int_B M^i(\mathbf{s}, \mathbf{x}) u(\mathbf{s}) dB(\mathbf{s}) - \int_B L^i(\mathbf{s}, \mathbf{x}) t(\mathbf{s}) dB(\mathbf{s}), \quad \mathbf{x} \in \Omega^c \cup B$

where $C.P.V$, $R.P.V$ and $H.P.V$ denote the Cauchy principal value, Riemann principal value and Hadamard principal value, respectively.

Table 3-2 Torsional rigidity of a circular cylinder with a single eccentric hole ($a/R=1/3$)

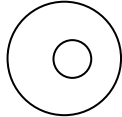
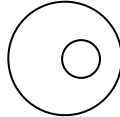
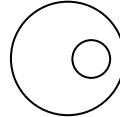
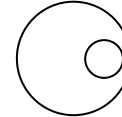
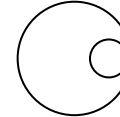
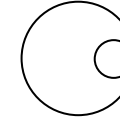
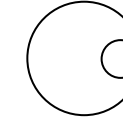
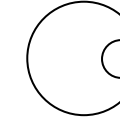
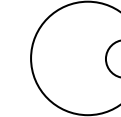
Geometry											
$\frac{b}{R-a}$			0.20	0.40	0.60	0.80	0.90	0.92	0.94	0.96	0.98
$\frac{2G}{(\mu\pi R^4)}$	Exact solution [68]		0.97872	0.95137	0.90312	0.82473	0.76168	0.74454	0.72446	0.69968	0.66555
	Present method	$L = 20$	0.97872	0.95137	0.90312	0.82473	0.76168	0.74455	0.72451	0.69991	0.66705
		$L = 10$	0.97872	0.95137	0.90312	0.82476	0.76244	0.74603	0.72748	0.70616	0.68111
	Caulk's method (BIE) [14]	40 divisions	0.97872	0.95137	0.90316	0.82497	0.76252	0.74569	0.72605	0.70178	0.66732
		20 divisions	0.97873	0.95140	0.90328	0.82574	0.76583	0.75057	0.73367	0.71473	0.69321

Table 3-3 Torsional rigidity of a circular cylinder with a ring of N holes $a/R=1/4$, $b/R=1/2$

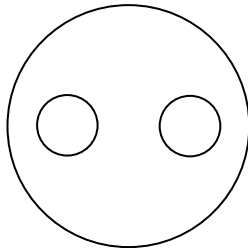
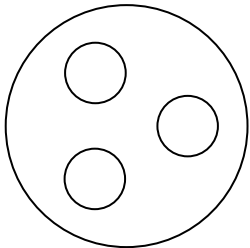
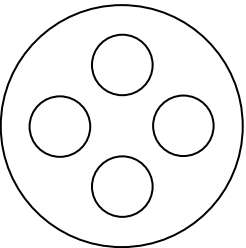
Number of holes				
		2	3	4
$\frac{2G}{(\mu\pi R^4)}$	Caulk (First-order Approximate) [14]	0.8661	0.8224	0.7934
	Caulk (BIE formulation) [14]	0.8657	0.8214	0.7893
	Present method ($L=10$)	0.8657	0.8214	0.7893

Table 3-4 Torsional rigidity in Ling's [57] examples

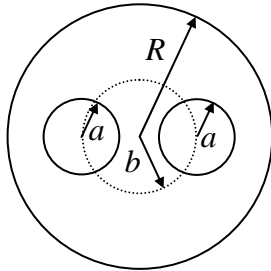
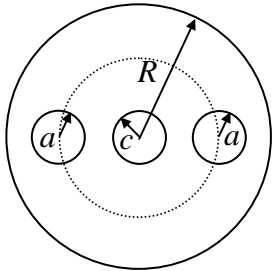
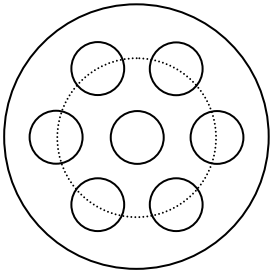
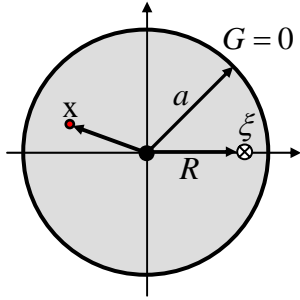
Case				
	$a/R=2/7, b/R=3/7$	$c/R=1/5, a/R=1/5, b/R=3/5$	$c/R=1/5, a/R=1/5, b/R=3/5$	
$\frac{2G}{(\mu\pi R^4)}$	Caulk (First-order approximate) [14]	0.8739	0.8741	0.7261
	Caulk (BIE formulation) [14]	0.8713	0.8732	0.7261
	Ling's results	0.8809	0.8093	0.7305
	Present method ($L=10$)	0.8712	0.8732	0.7244

Table 5-1 Green's functions of interior and exterior problems.

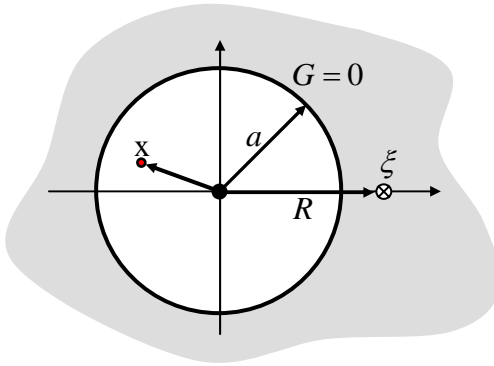


Close form [31]:

$$G(x; \xi, \xi') = \ln|x - \xi| - \ln|x - \xi'| + \ln a - \ln R$$

Series form [31]:

$$G(x; \xi, \xi') = \begin{cases} \ln\left(\frac{R}{a}\right) - \sum_{m=1}^{\infty} \frac{1}{m} \left[\left(\frac{\rho}{R}\right)^m - \left(\frac{\rho R}{a^2}\right)^m \right] \cos(m(\theta - \phi)), & 0 < \rho \leq R \\ \ln\left(\frac{\rho}{a}\right) - \sum_{m=1}^{\infty} \frac{1}{m} \left[\left(\frac{R}{\rho}\right)^m - \left(\frac{\rho R}{a^2}\right)^m \right] \cos(m(\theta - \phi)), & R \leq \rho < a \end{cases}$$



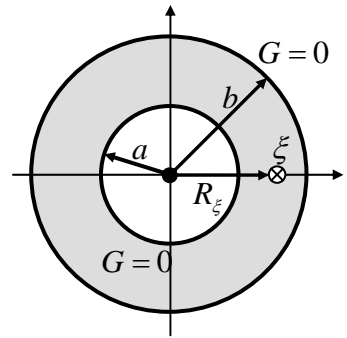
Close form [31]:

$$G(x; \xi, \xi') = \ln|x - \xi| - \ln|x - \xi'| + \ln a - \ln R$$

Series form [31]:

$$G(x; \xi, \xi') = \begin{cases} \ln\left(\frac{a}{\rho}\right) - \sum_{m=1}^{\infty} \frac{1}{m} \left[\left(\frac{\rho}{R}\right)^m - \left(\frac{a^2}{\rho R}\right)^m \right] \cos(m(\theta - \phi)), & a < \rho \leq R \\ \ln\left(\frac{a}{R}\right) - \sum_{m=1}^{\infty} \frac{1}{m} \left[\left(\frac{R}{\rho}\right)^m - \left(\frac{a^2}{\rho R}\right)^m \right] \cos(m(\theta - \phi)), & R \leq \rho < \infty \end{cases}$$

Table 5-2 Green's function of annular case

	<p>Series form</p> $G(x, \xi) = -(b \ln b \, p_0 + a \ln \rho \, \bar{p}_0) + \sum_{m=1}^{\infty} \frac{1}{2m} \left[\left(b \left(\frac{\rho}{b} \right)^m p_m + a \left(\frac{a}{\rho} \right)^m \bar{p}_m \right) \cos m\phi + \left(b \left(\frac{\rho}{b} \right)^m q_m + a \left(\frac{a}{\rho} \right)^m \bar{q}_m \right) \sin m\phi \right] + \frac{\ln x - \xi }{2\pi}$
	<p>Series form</p> $G(x, \xi) = - \left(b \ln b \, p_0 + a \ln \rho \, \bar{p}_0 - \frac{\ln R_\xi}{2\pi} \right) + \sum_{m=1}^{\infty} \frac{1}{2m} \left[\left(b \left(\frac{\rho}{b} \right)^m p_m + a \left(\frac{a}{\rho} \right)^m \bar{p}_m - \left(\frac{\rho}{R_\xi} \right)^m \frac{\cos m\theta_\xi}{\pi} \right) \cos m\phi + \left(b \left(\frac{\rho}{b} \right)^m q_m + a \left(\frac{a}{\rho} \right)^m \bar{q}_m - \left(\frac{\rho}{R_\xi} \right)^m \frac{\sin m\theta_\xi}{\pi} \right) \sin m\phi \right], \quad a \leq \rho \leq R_\xi$ $G(x, \xi) = - \left(b \ln b p_0 + a \ln \rho \bar{p}_0 + \frac{\ln \rho}{2\pi} \right) + \sum_{m=1}^{\infty} \frac{1}{2m} \left[\left(b \left(\frac{\rho}{b} \right)^m p_m + a \left(\frac{a}{\rho} \right)^m \bar{p}_m - \left(\frac{R_\xi}{\rho} \right)^m \frac{\cos m\theta_\xi}{\pi} \right) \cos m\phi + \left(b \left(\frac{\rho}{b} \right)^m q_m + a \left(\frac{a}{\rho} \right)^m \bar{q}_m - \left(\frac{R_\xi}{\rho} \right)^m \frac{\sin m\theta_\xi}{\pi} \right) \sin m\phi \right], \quad R_\xi \leq \rho \leq b$

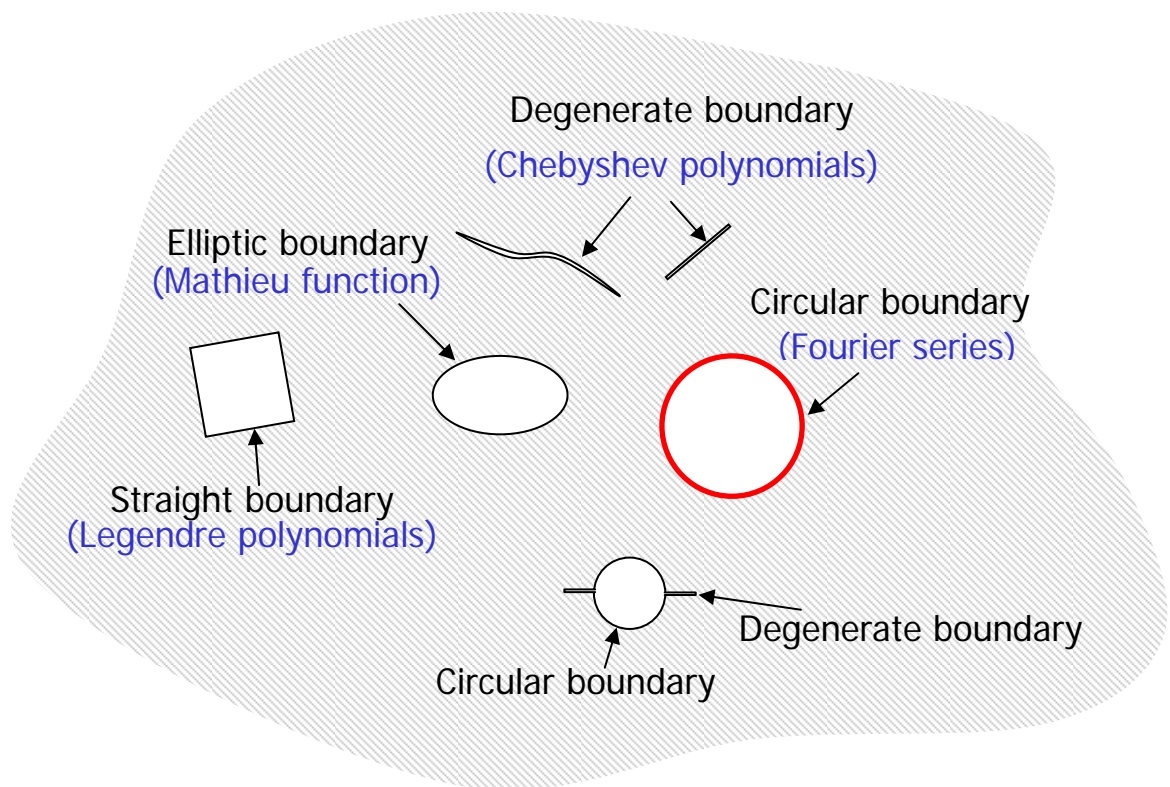


Figure 1-1 The boundary value problems with arbitrary boundaries.

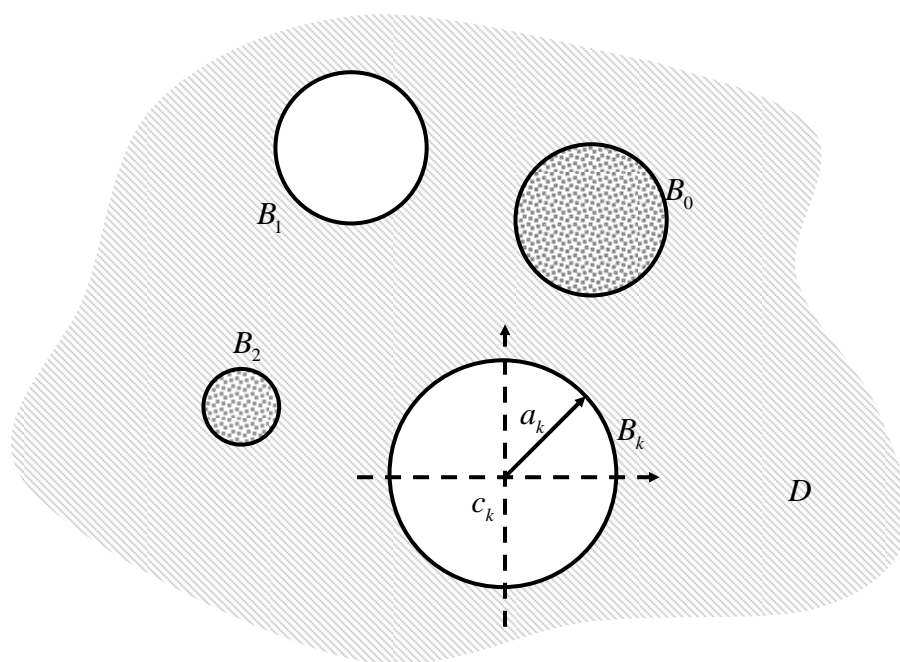


Figure 2-1 Problem statement.

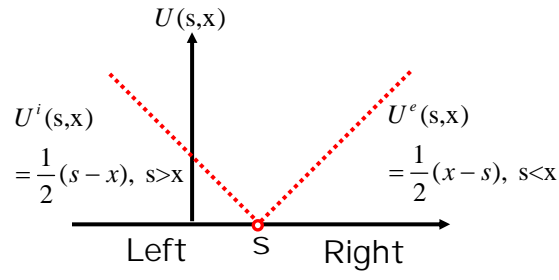


Figure 2-2 (a) The 1-D degenerate kernel for $U(s,x)$.

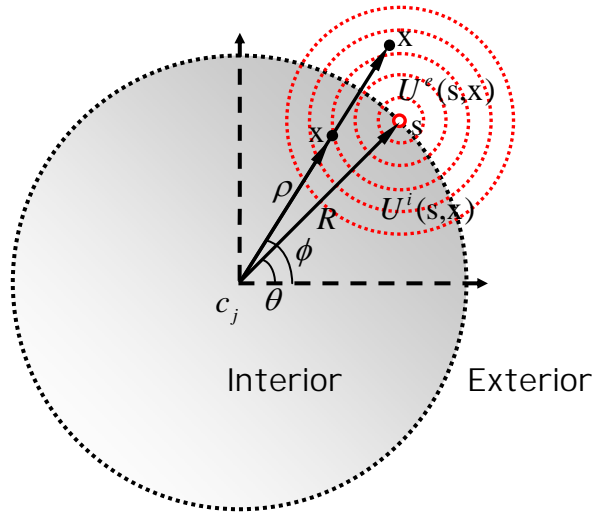


Figure 2-2 (b) The 2-D degenerate kernel for $U(s,x)$.

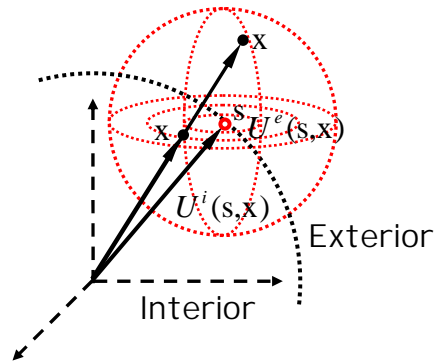


Figure 2-2 (c) The 3-D degenerate kernel for $U(s,x)$.

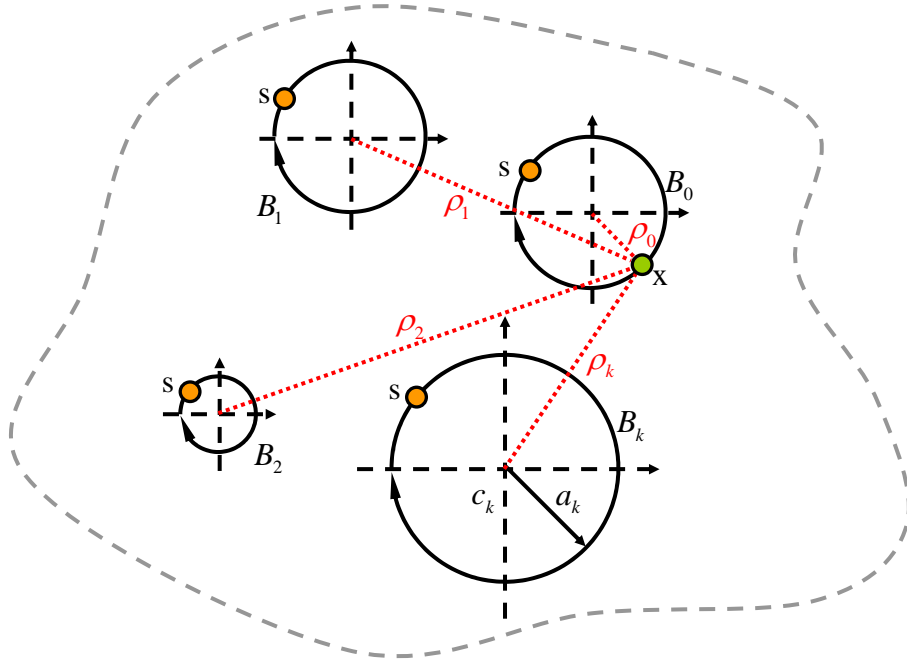


Figure 2-3 (a) Sketch of the null-field integral equation in conjunction with the adaptive observer system.

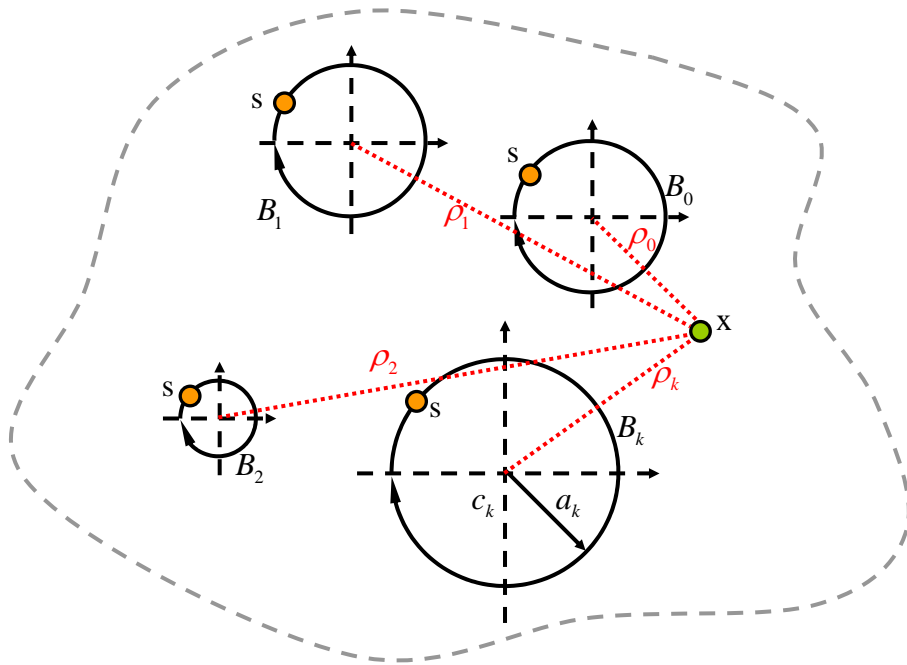
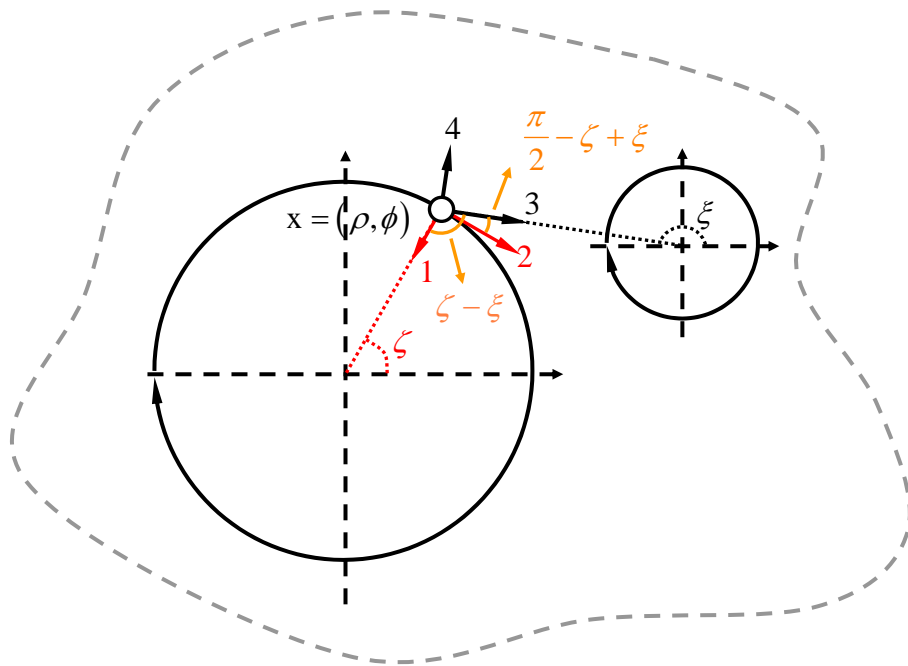


Figure 2-3 (b) Sketch of the boundary integral equation for the domain point in conjunction with the adaptive observer system.



- 1: True normal direction
- 2: True tangential direction
- 3: Normal direction
- 4: Tangential direction

Figure 2-4 Vector decomposition for the potential gradient in the hypersingular equation.

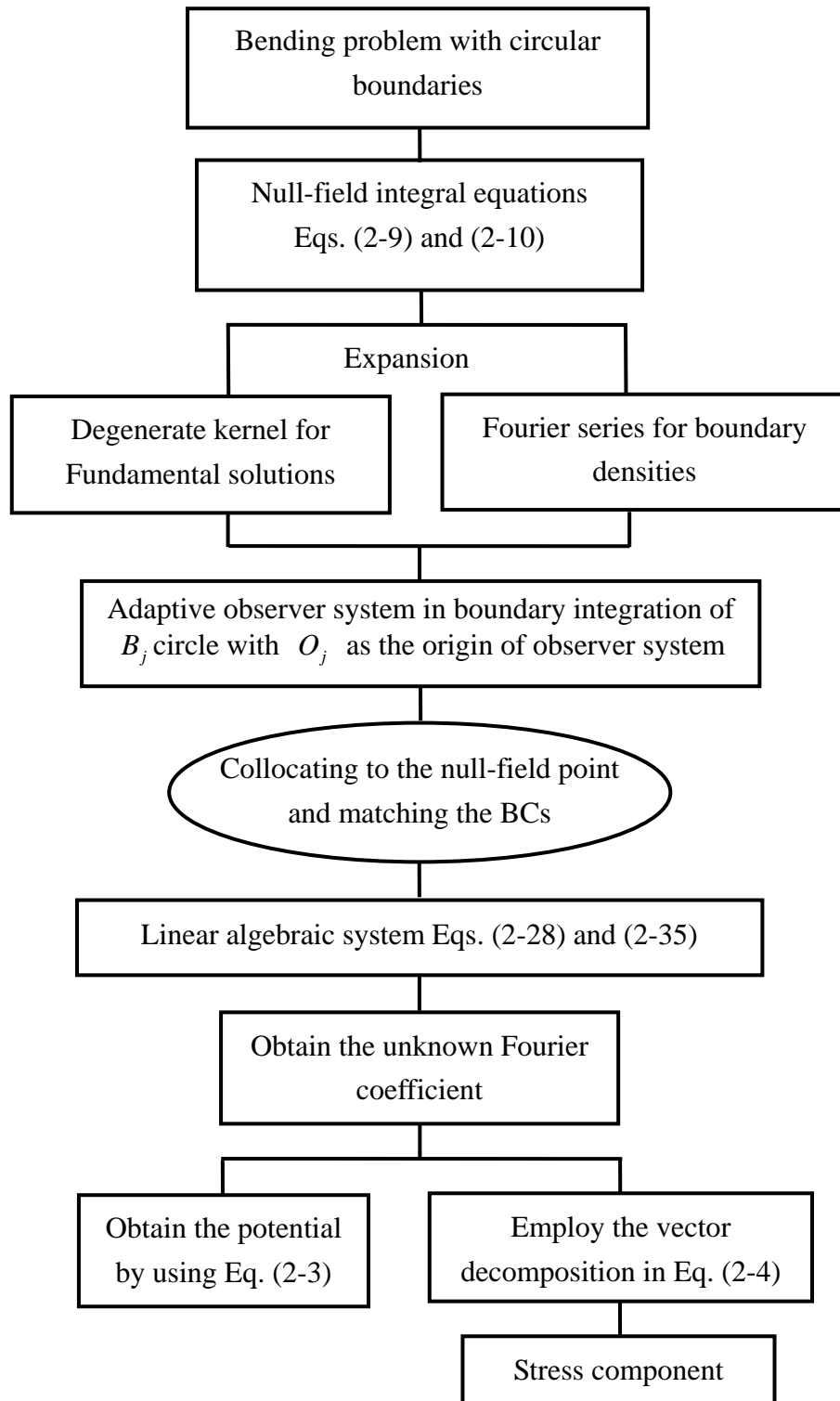


Figure 2-5 The flowchart of the present method.

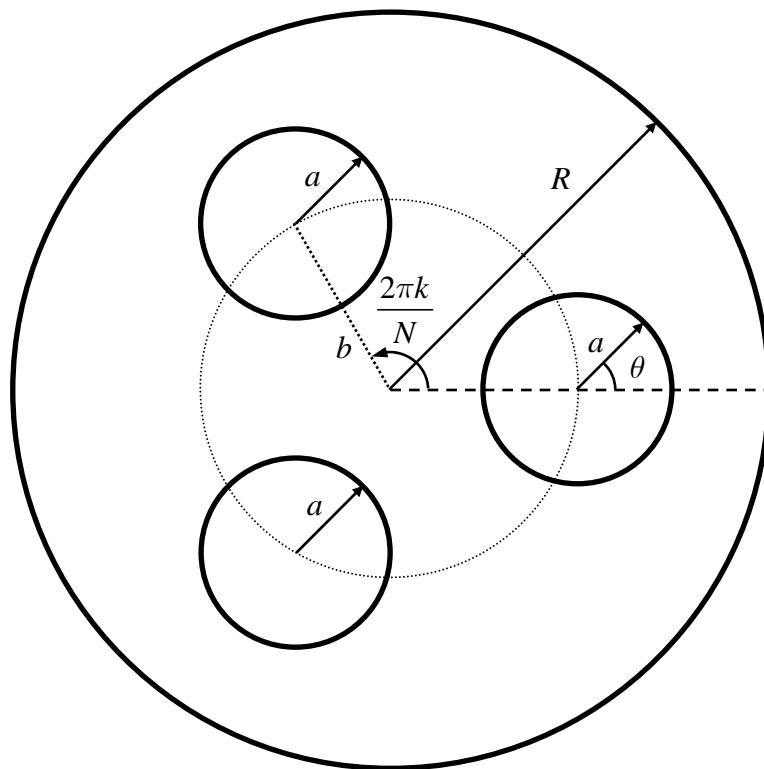


Figure 3-1 Cross section of a bar weakened by N ($N = 3$) equal circular holes.

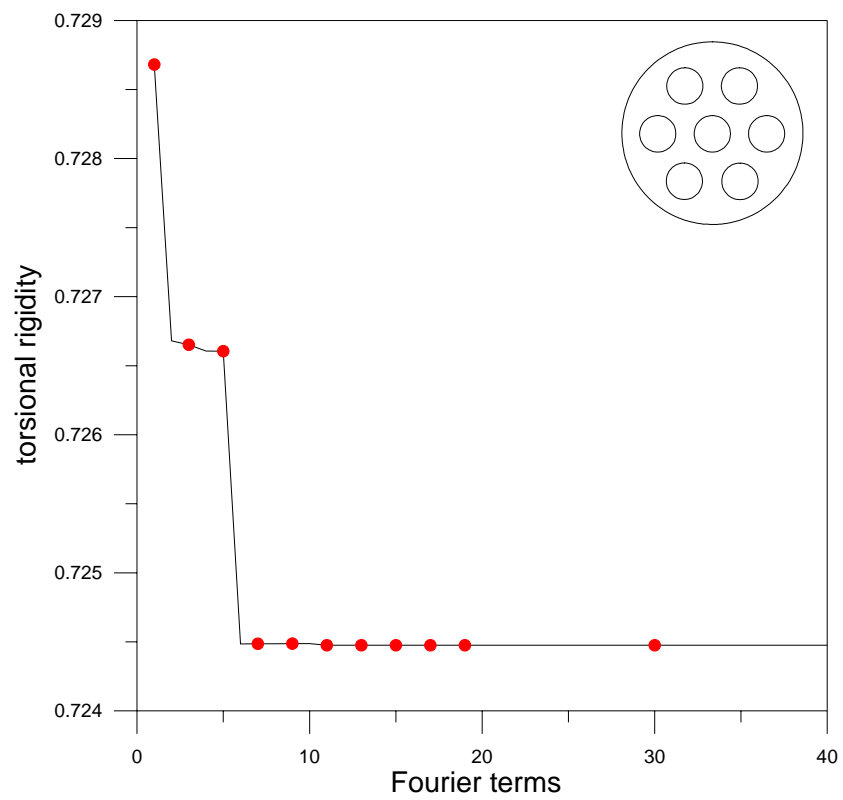
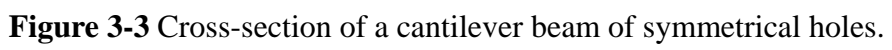
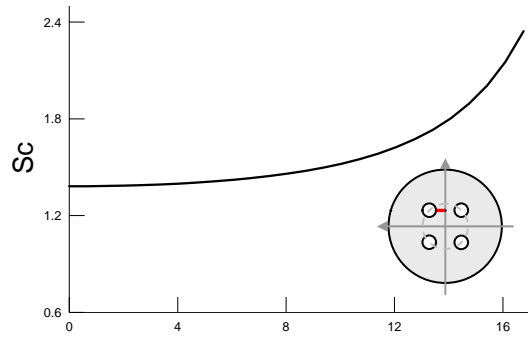
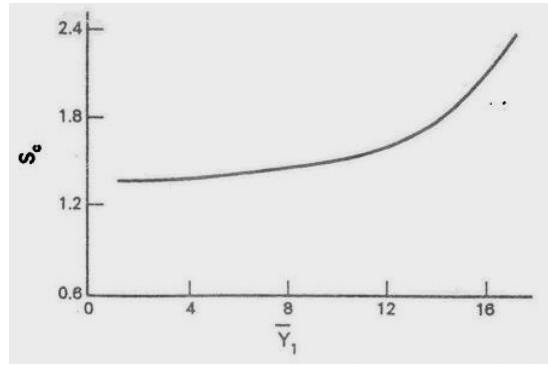


Figure 3-2 Torsion rigidity versus the number of Fourier terms.

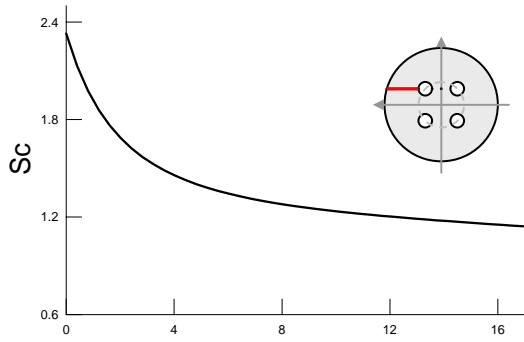




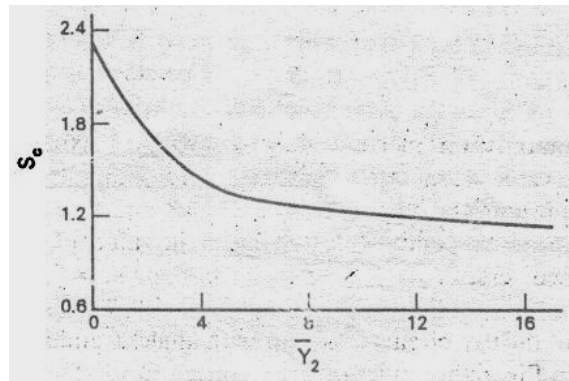
(a)



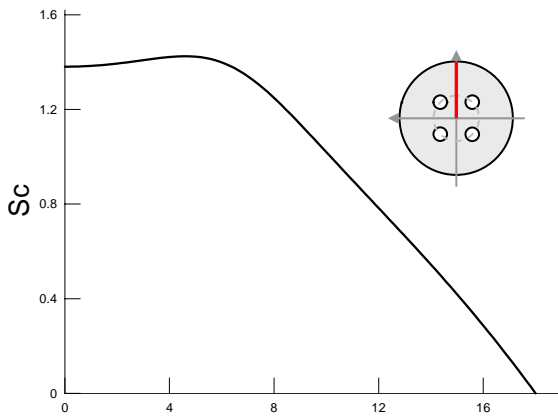
(d)



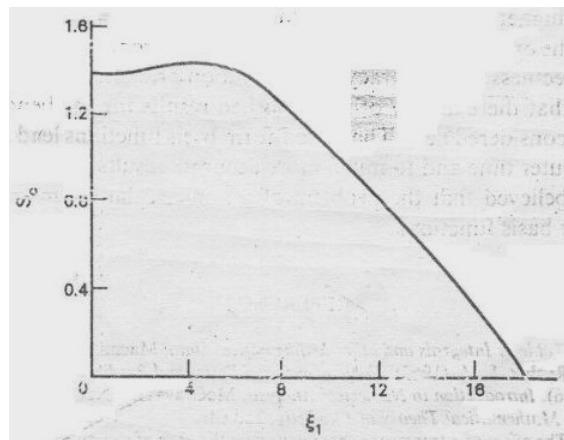
(b)



(e)



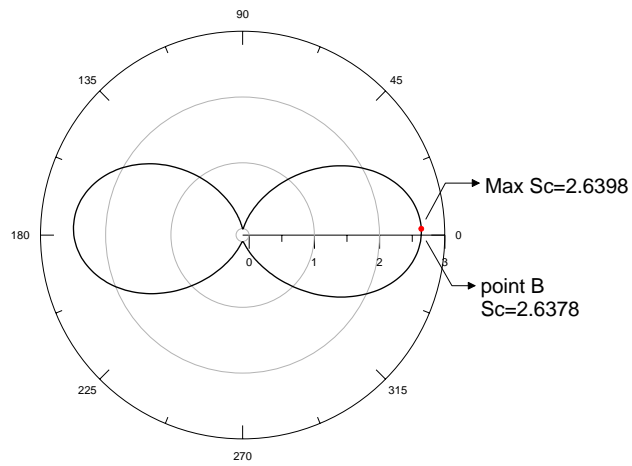
(c)



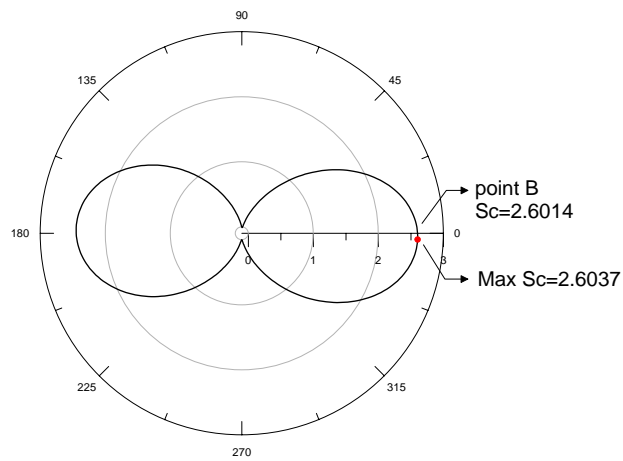
(f)

Figure 3-4 Stress concentration for $R=1.0$, $b=0.5$, $\bar{\theta} = \pi/4$ and $a=0.1$.

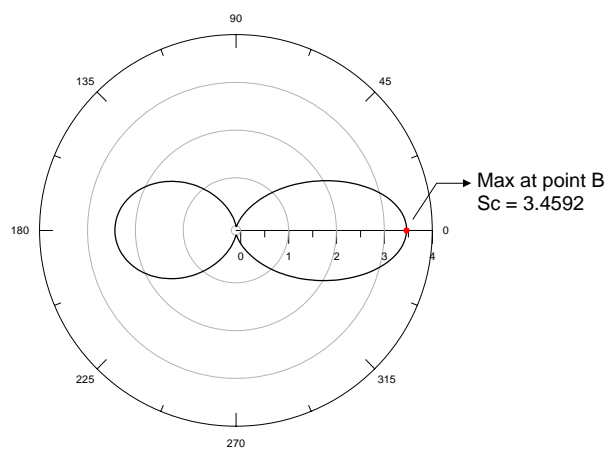
- (a) Sc along AB (Present method)
- (b) Sc along CD (Present method)
- (c) Sc along OT (Present method)
- (d) Sc along AB (Naghdi's result) [68]
- (e) Sc along CD (Naghdi's result) [68]
- (f) Sc along OT (Naghdi's result) [68]



(a) $\bar{\theta} = 22.5$

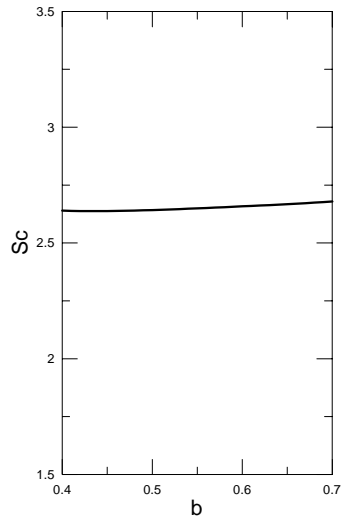


(b) $\bar{\theta} = 45$

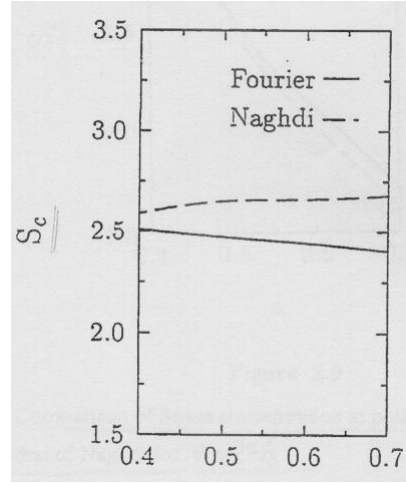


(c) $\bar{\theta} = 67.5$

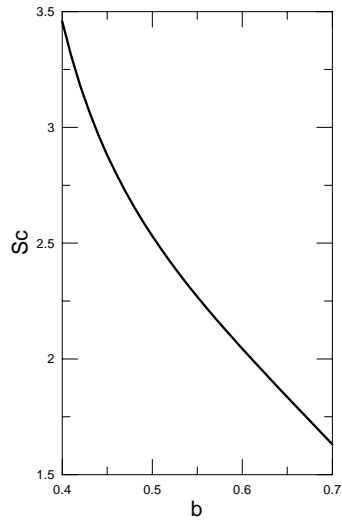
Figure 3-5 Stress concentrations around the third circle.



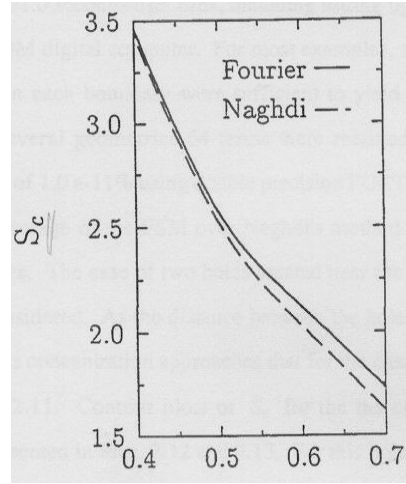
(a)



(c)



(b)



(d)

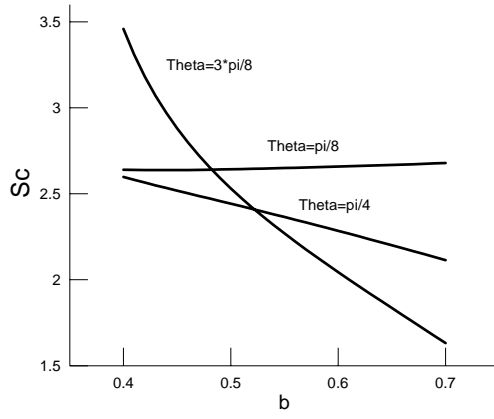
Figure 3-6 Stress concentration versus b for $a = 0.12$ and $R = 1.0$.

(a) $\bar{\theta} = \pi/8$ (Present method)

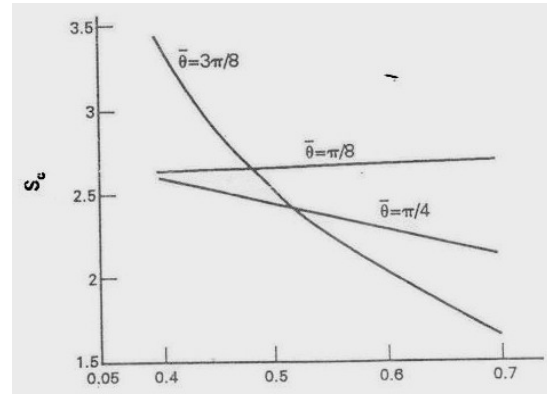
(b) $\bar{\theta} = 3\pi/8$ (Present method)

(c) $\bar{\theta} = \pi/8$ (Bird's result [6])

(d) $\bar{\theta} = 3\pi/8$ (Bird's result [6])



(a)



(b)

Figure 3-7 Stress concentration versus b for $a = 0.12$, $R = 1.0$ and three different values of $\bar{\theta} = \pi/8$, $\bar{\theta} = \pi/4$ and $\bar{\theta} = 3\pi/8$.

(a) S_c at the point B (Present method)

(b) S_c at the point B (Naghdi's result [68])

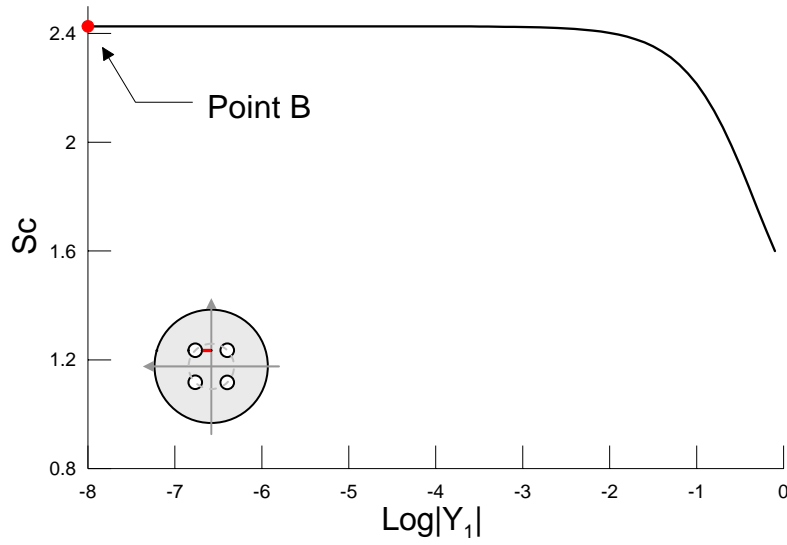


Figure 3-8 Stress concentration along \overline{AB} and extremely close to the point B for $b = 5$, $a = 1$, $R = 10$ and $\bar{\theta} = \pi/4$.

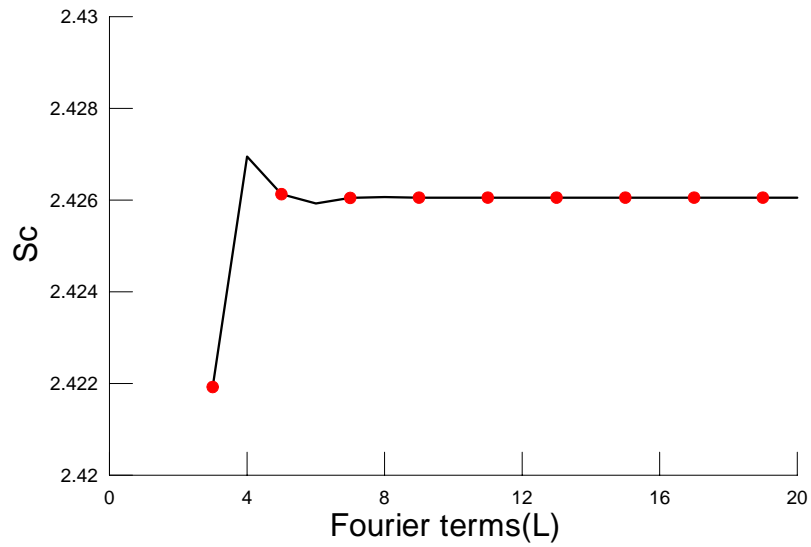
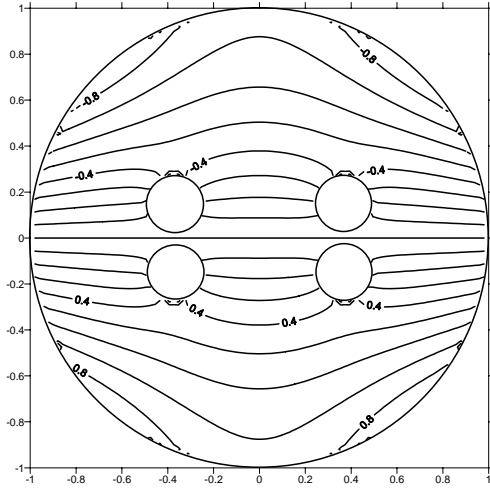
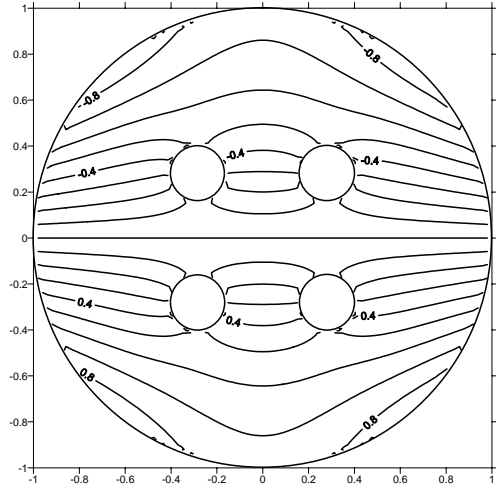


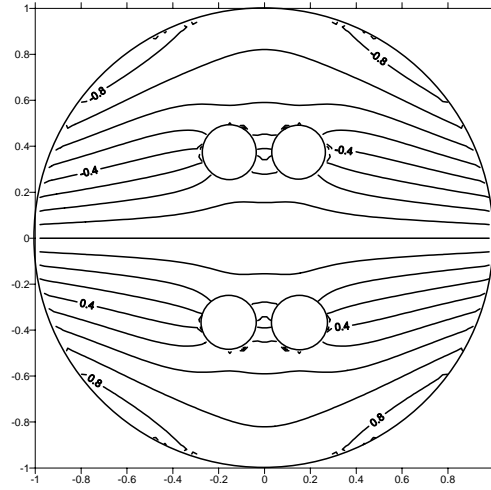
Figure 3-9 Stress concentration on point B for $R = 1.0$, $b = 0.5$, $\bar{\theta} = \pi/4$ and $a = 0.1$.



(a) $\bar{\theta} = \pi/8$



(b) $\bar{\theta} = \pi/4$



(c) $\bar{\theta} = 3\pi/8$

Figure 3-10 Contour plot for $R=1.0$, $b=0.4$, $a=0.12$ for three various values of
(a) $\bar{\theta} = \pi/8$, (b) $\bar{\theta} = \pi/4$ and (c) $\bar{\theta} = 3\pi/8$.

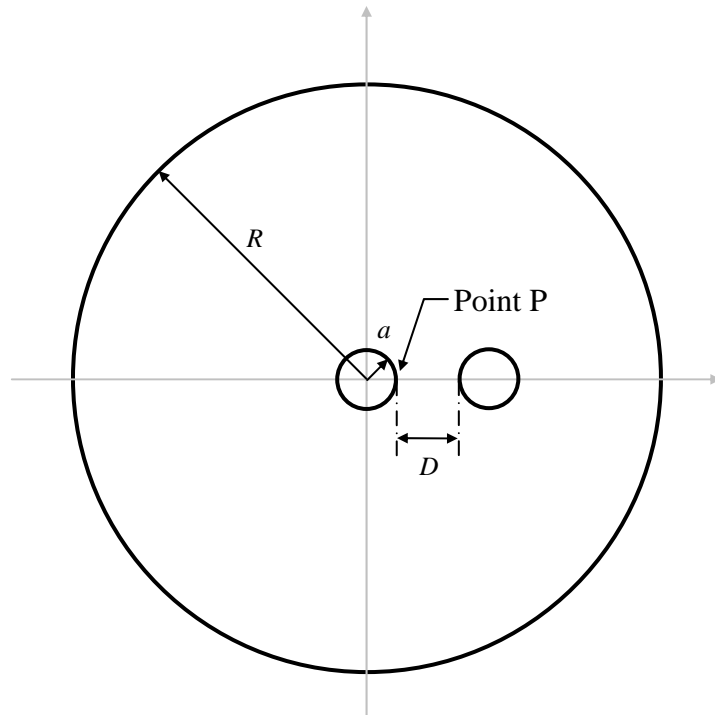
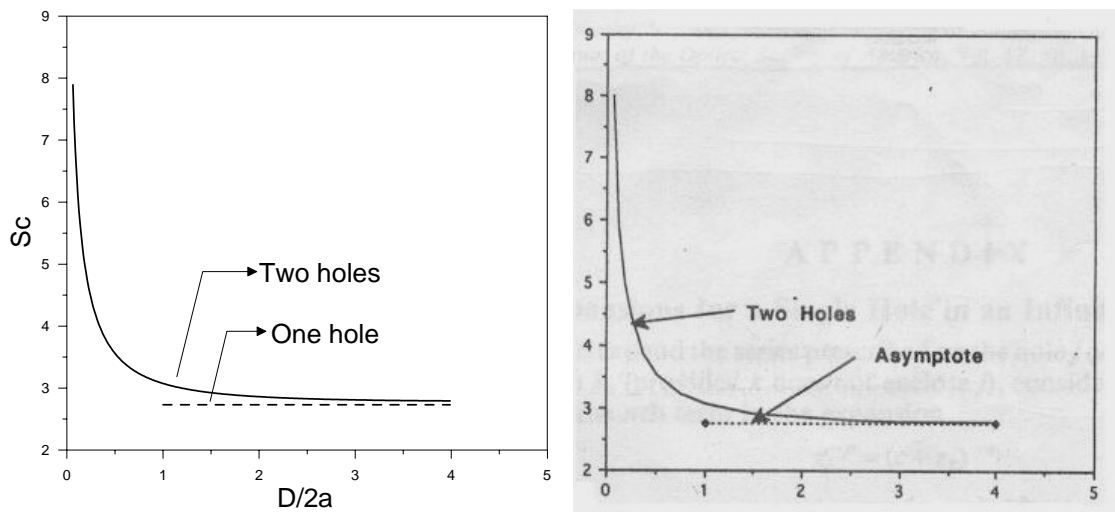


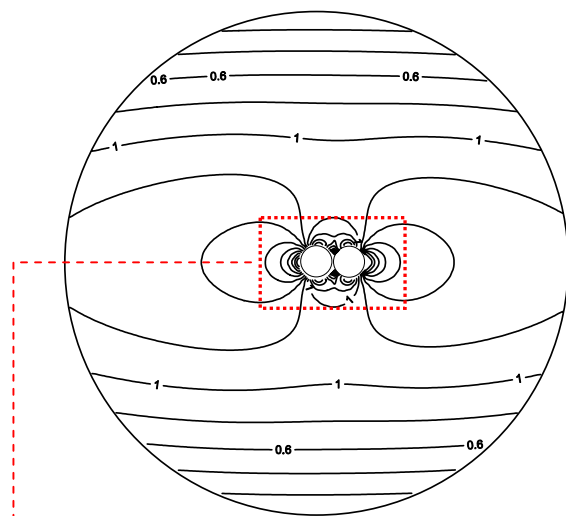
Figure 3-11 Cantilever beam under bending weakened by two holes the on x -axis



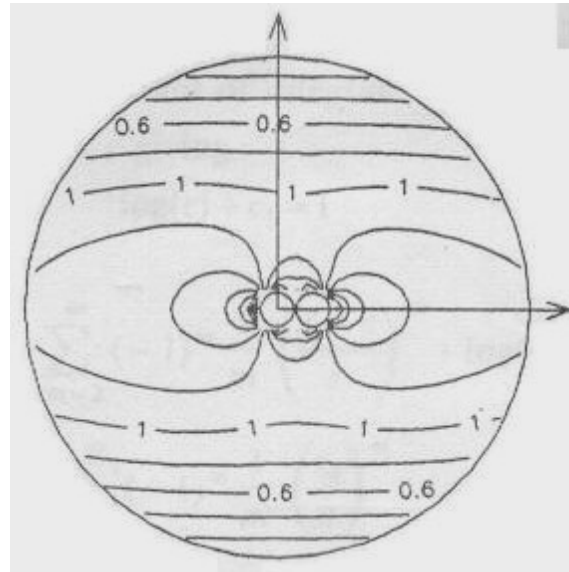
(a) Present method

(b) Bird's result [6]

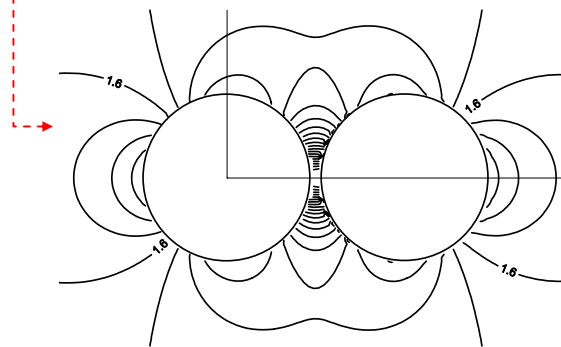
Figure 3-12 Stress concentration versus $D/2a$ for the point P .



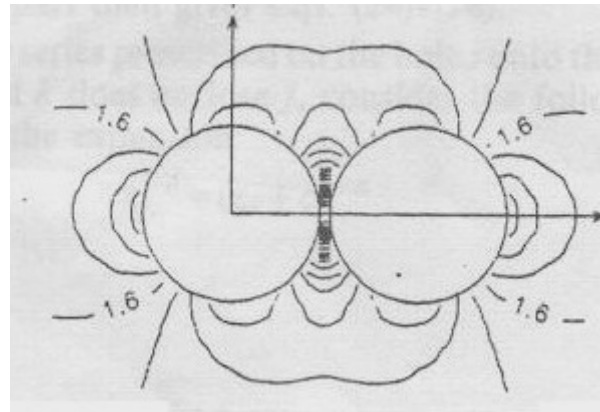
(a) Present method



(c) Bird's result [6]



(b) Present method (local)



(d) Bird's result (local) [6]

Figure 3-13 Contour of stress concentration of $D/2a = 0.0625$

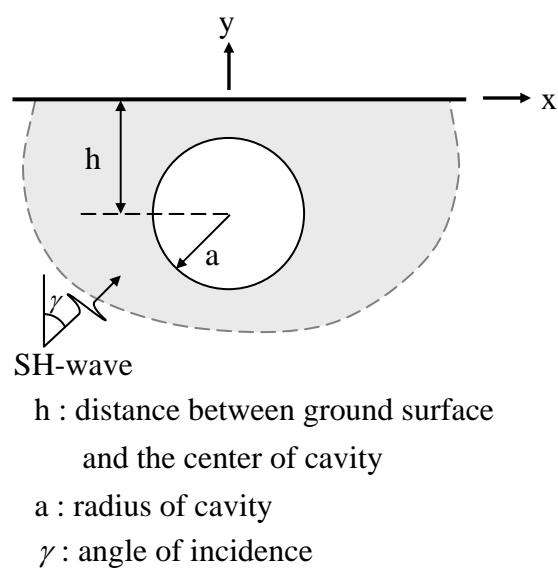
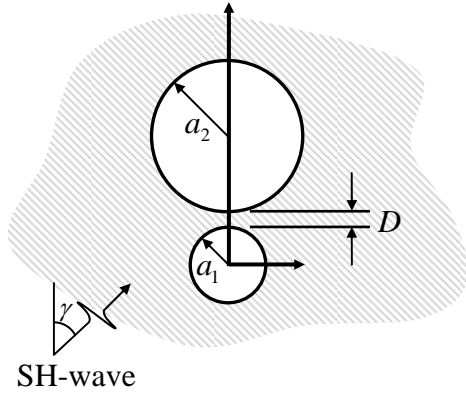
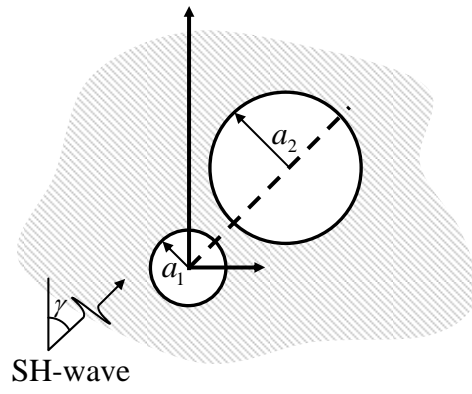


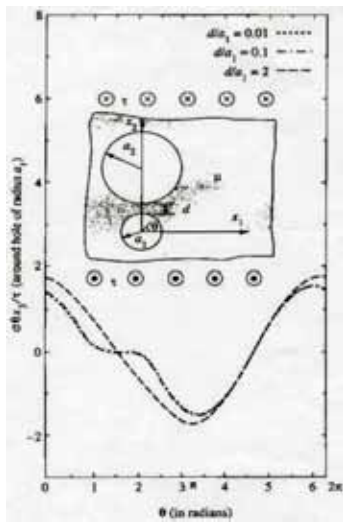
Figure 4-1 A half-plane problem with a circular cavity subject to incident SH-wave.



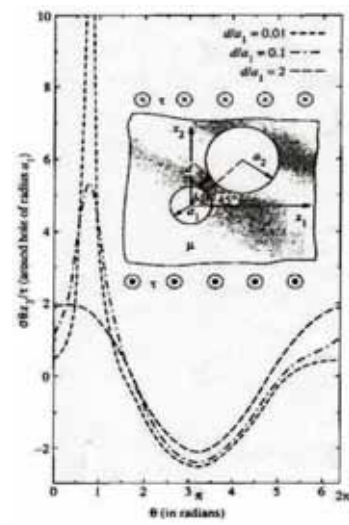
(a) Two cavities with centers on the y -axis



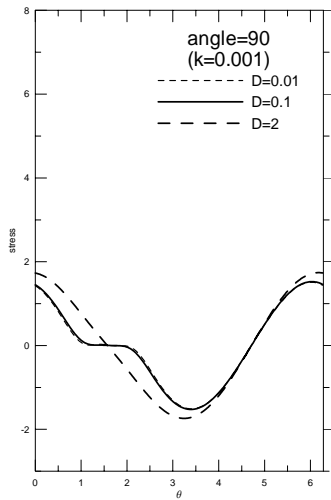
(b) Two cavities with centers on the 45° -axis



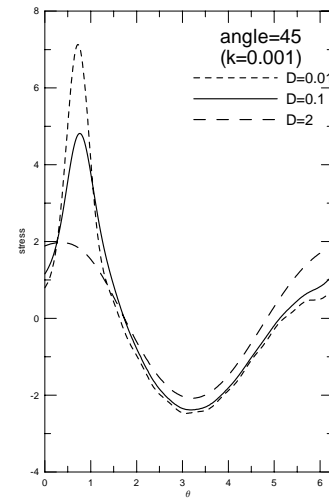
(c) Shear stress around the smaller cavity (Honein's result [44])



(d) Shear stress around the smaller cavity (Honein's result [44])

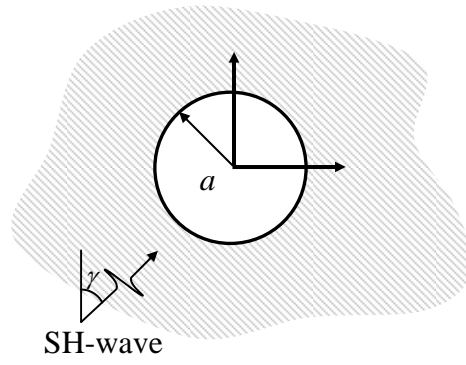


(e) Shear stress around the smaller cavity (Present method)

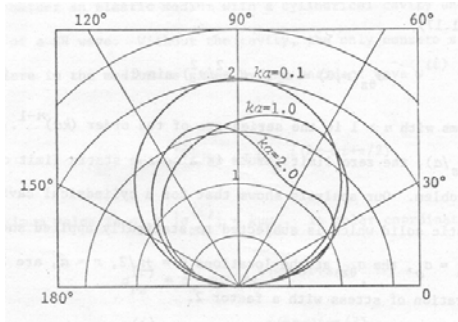


(f) Shear stress around the smaller cavity (Present method)

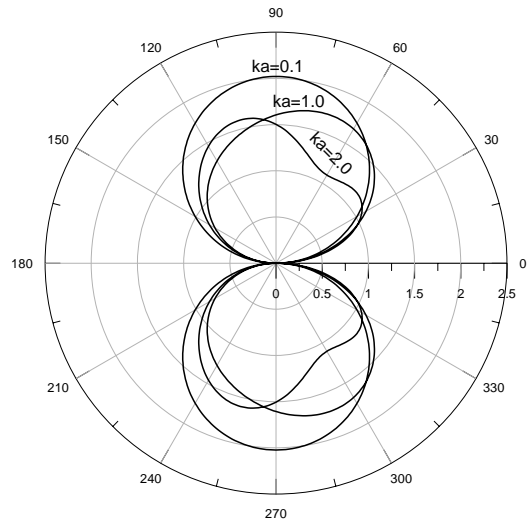
Figure 4-2 A full-plane problem with two cavities subject to the incident SH-wave.



(a) A full-plane problem with a cavity subject to SH-wave.



(b) Pao and Mow's result [70] (only half).



(c) Present method ($\gamma = 90^\circ$).

Figure 4-3 Shear stress (σ_{θ_z}) around the cavity of a full-plane problem subject to the horizontally incident SH wave.

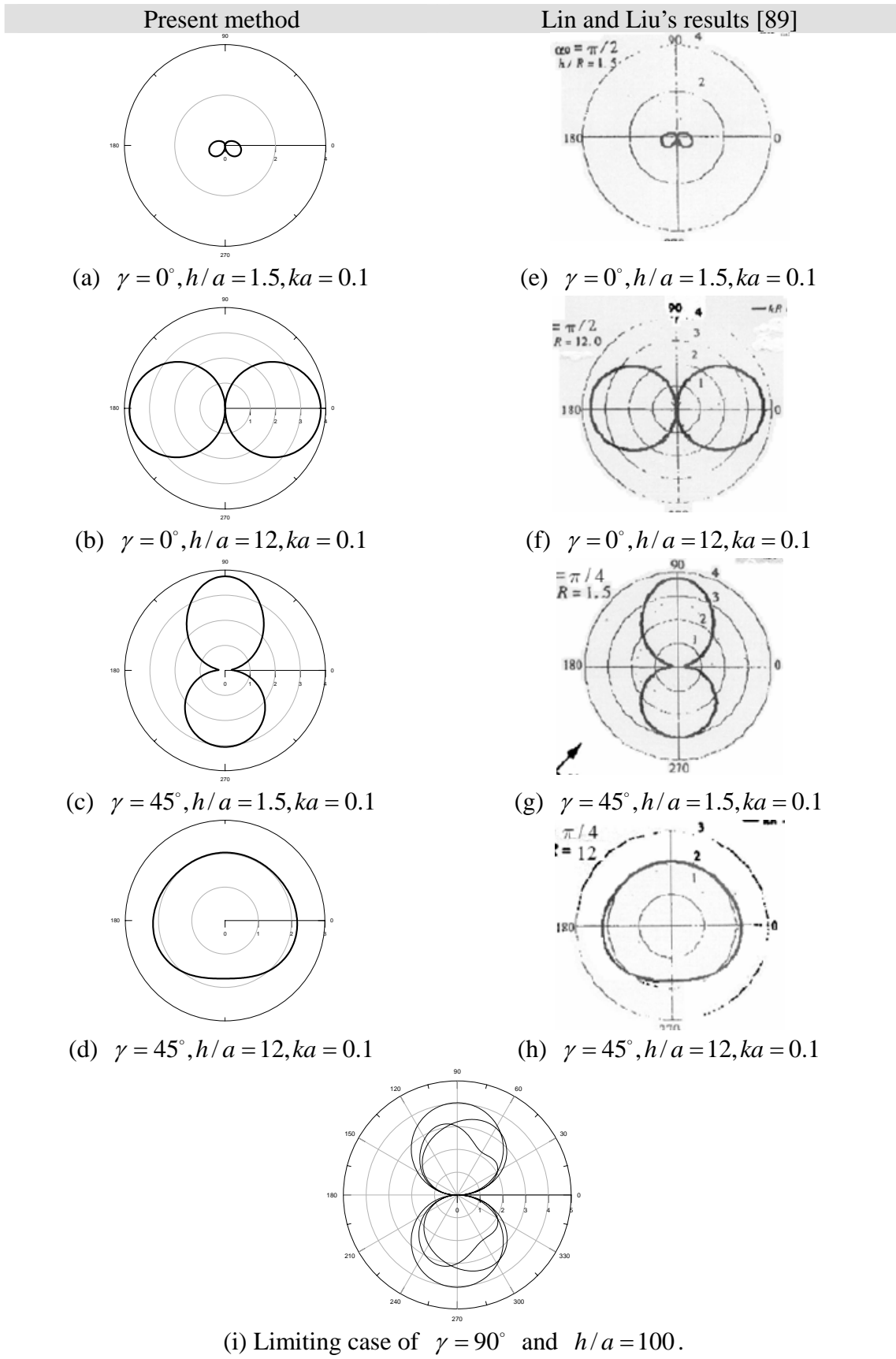
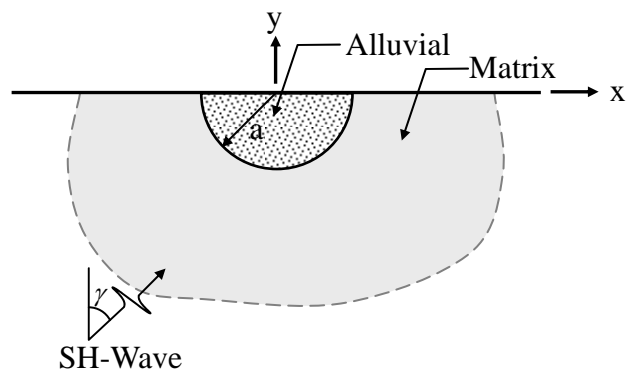


Figure 4-4 Shear stress ($\sigma_{\theta z}^*$) around the cavity under the ground surface subject to the SH-wave.



ρ_l : density of alluvial

ρ_M : density of matrix

μ_l : shear modulus of alluvial

μ_M : shear modulus of matrix

γ : the angle of incident wave and y-axis

Figure 4-5 A half-plane problem with a semi-circular alluvial valley subject to the SH-wave.

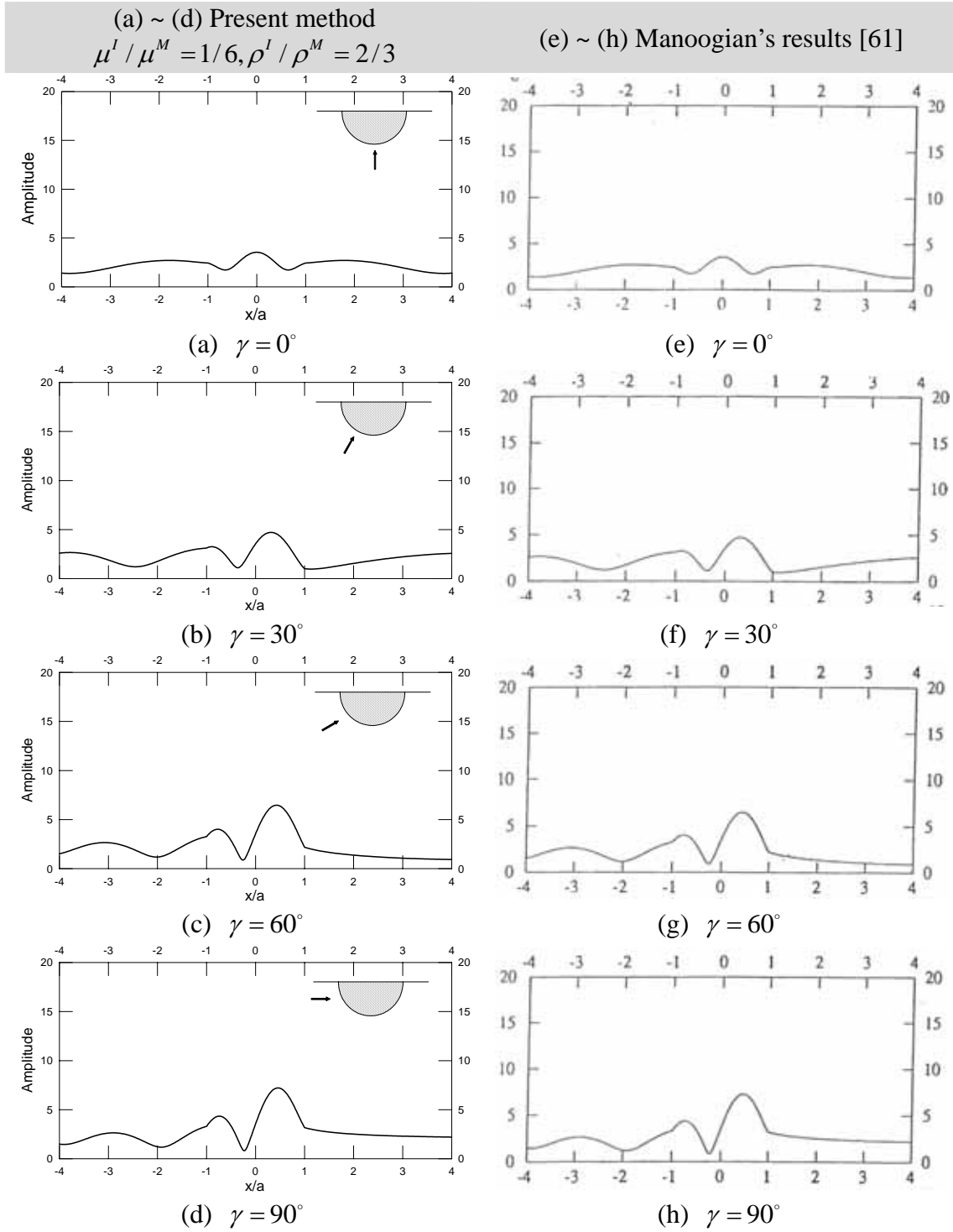


Figure 4-6 Surface amplitudes of the alluvial valley problem for $\eta = 0.5$.

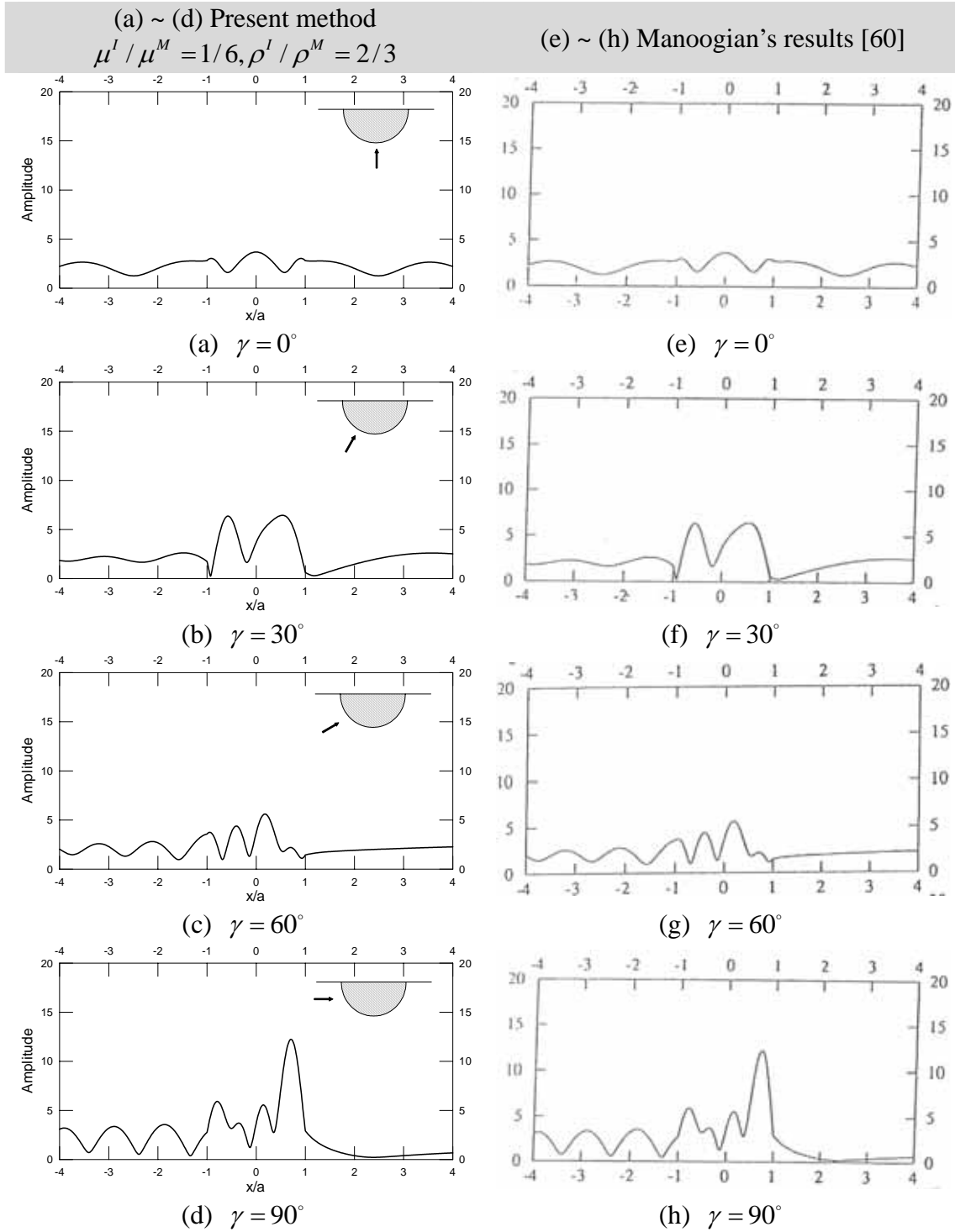


Figure 4-7 Surface amplitudes of the alluvial valley problem for $\eta = 1.0$.

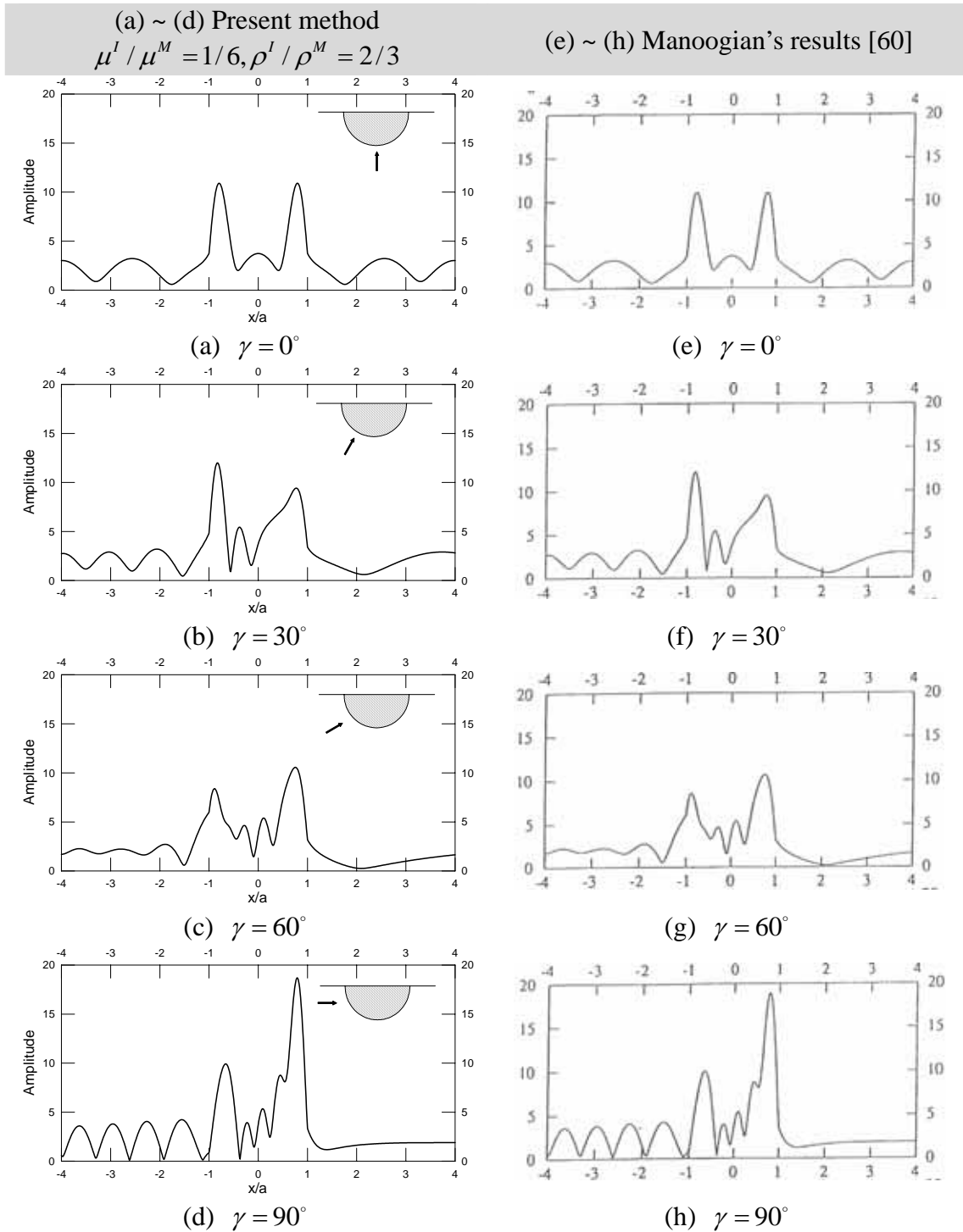


Figure 4-8 Surface amplitudes of the alluvial valley problem for $\eta = 1.5$.

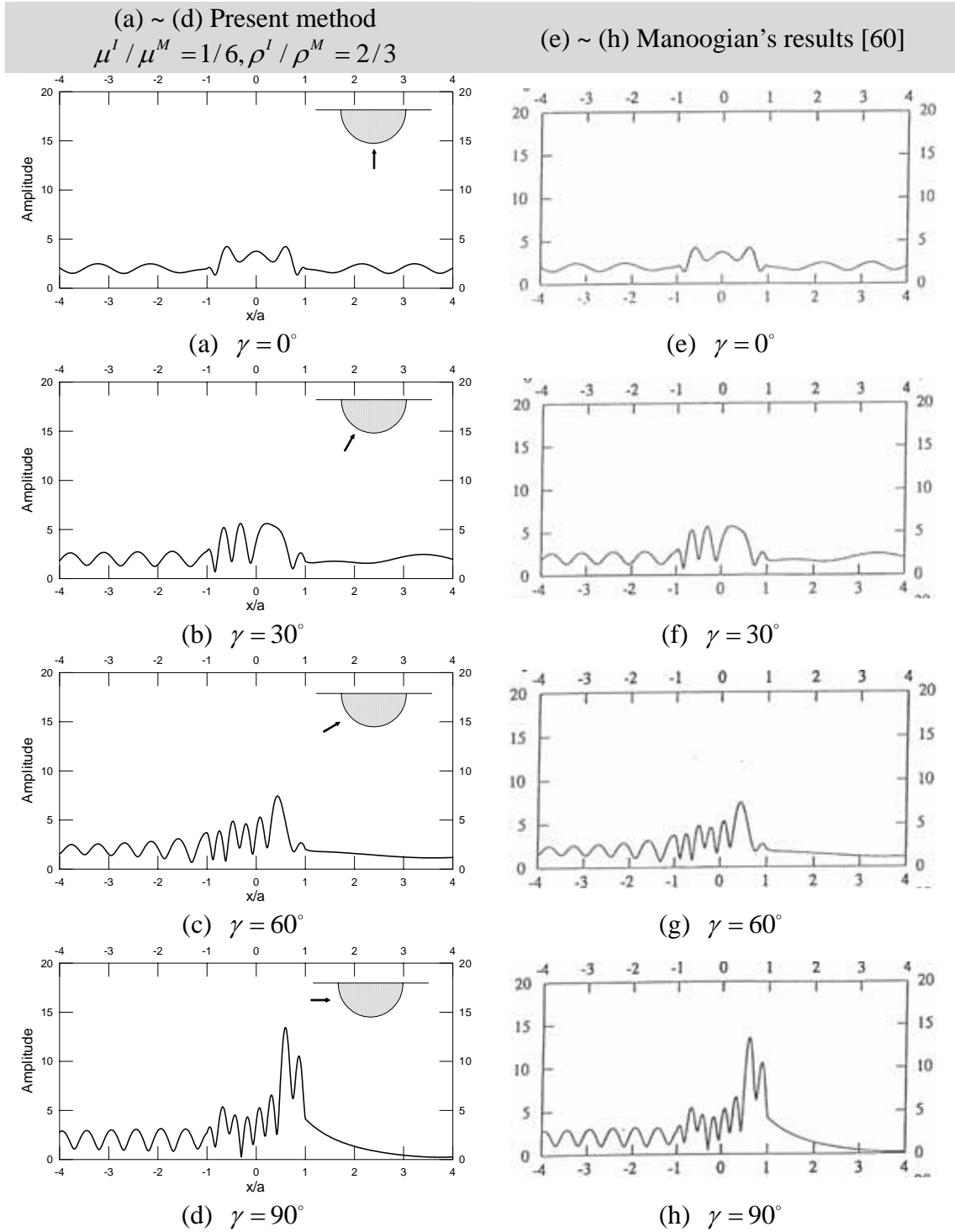
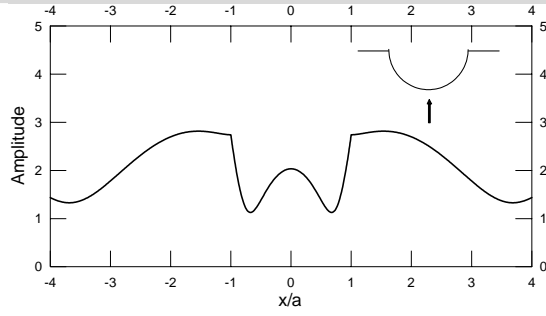


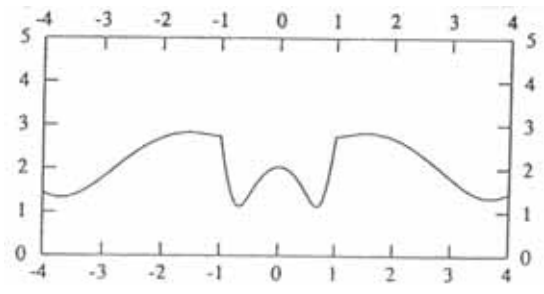
Figure 4-9 Surface amplitudes of the alluvial valley problem for $\eta = 2.0$.

(a) ~ (d) Present method $\rho^I / \rho^M = 2/3$

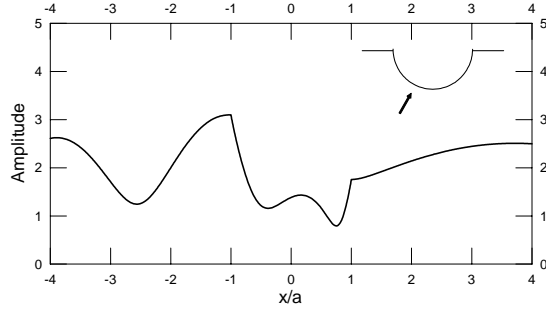
(e) ~ (h) Manoogian's results [60]



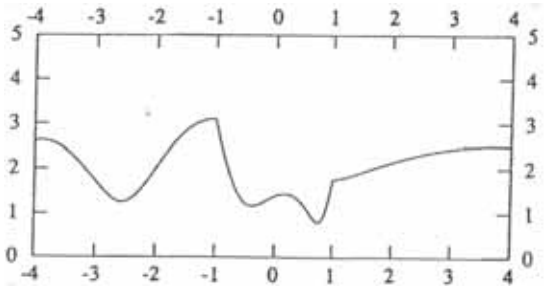
(a) $\gamma = 0^\circ$



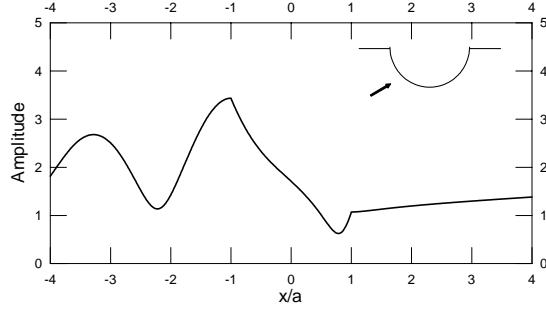
(e) $\gamma = 0^\circ$



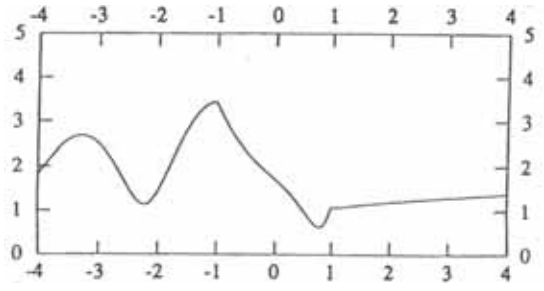
(b) $\gamma = 30^\circ$



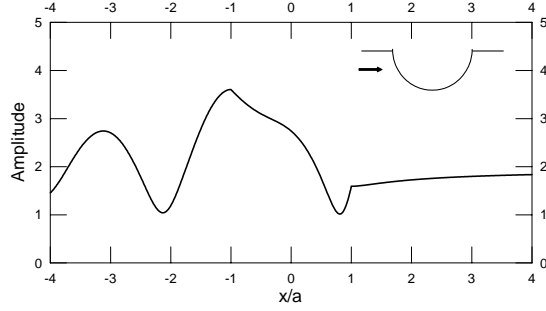
(f) $\gamma = 30^\circ$



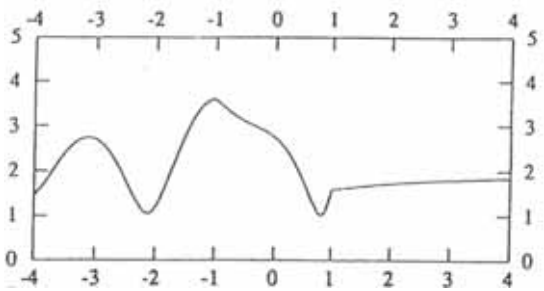
(c) $\gamma = 60^\circ$



(g) $\gamma = 60^\circ$



(d) $\gamma = 90^\circ$

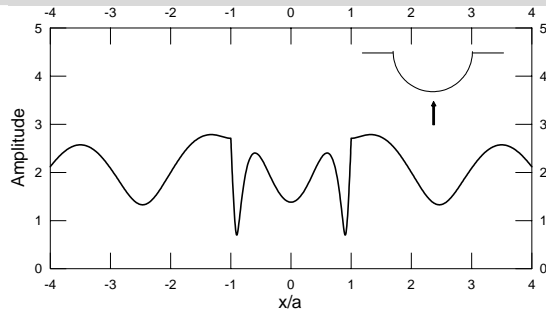


(h) $\gamma = 90^\circ$

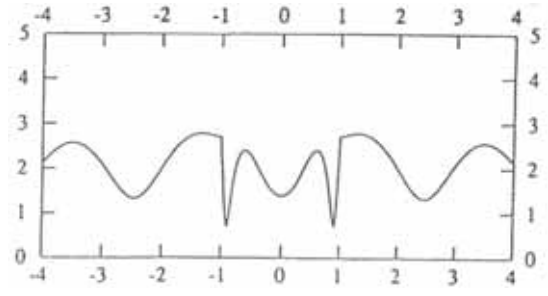
Figure 4-10 Limiting case of a canyon ($\mu^I / \mu^M = 10^{-8}$ and $\eta = 0.5$)

(a) ~ (d) Present method $\rho^I / \rho^M = 2/3$

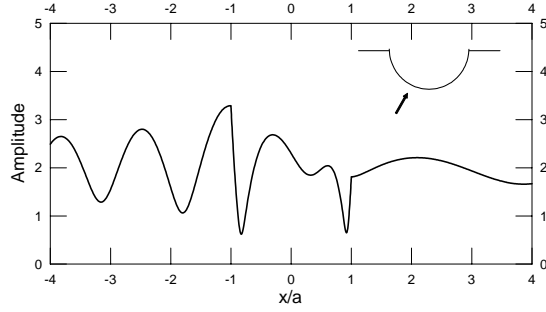
(e) ~ (h) Manoogian's results [60]



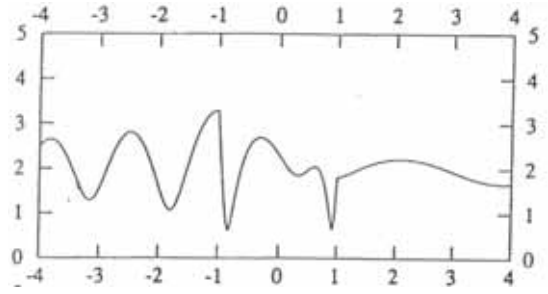
(a) $\gamma = 0^\circ$



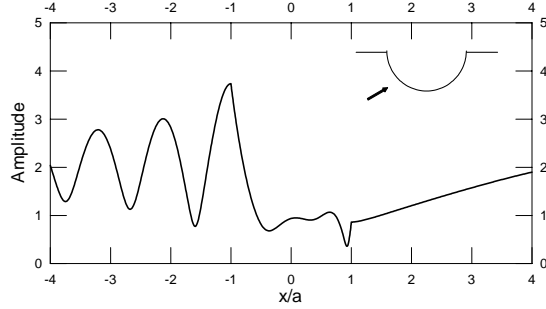
(e) $\gamma = 0^\circ$



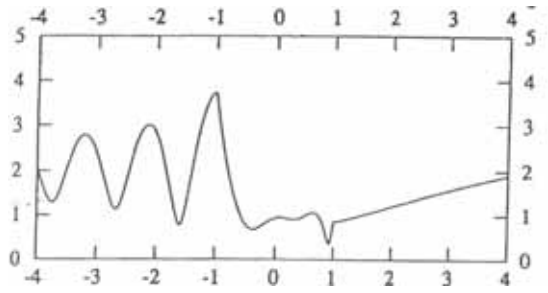
(b) $\gamma = 30^\circ$



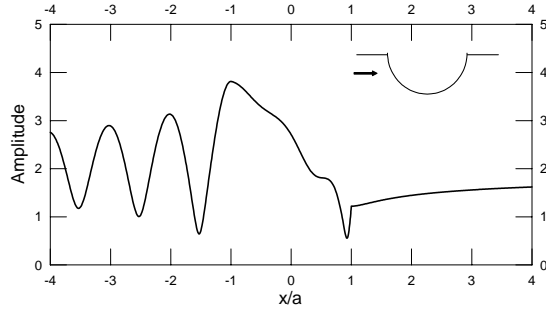
(f) $\gamma = 30^\circ$



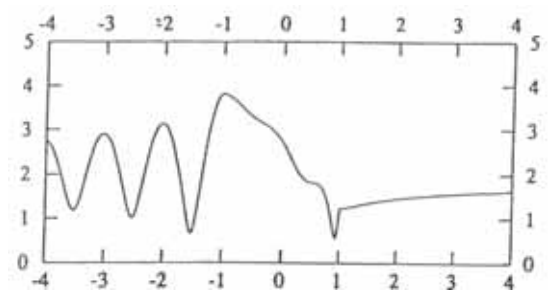
(c) $\gamma = 60^\circ$



(g) $\gamma = 60^\circ$



(d) $\gamma = 90^\circ$

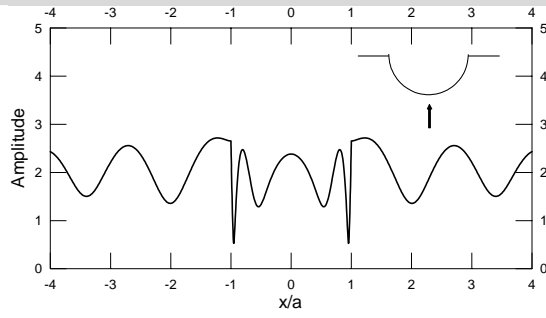


(h) $\gamma = 90^\circ$

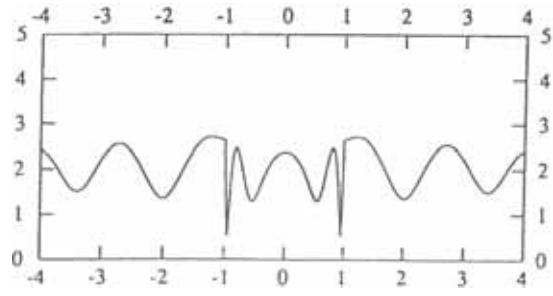
Figure 4-11 Limiting case of a canyon ($\mu^I / \mu^M = 10^{-8}$ and $\eta = 1$).

(a) ~ (d) Present method $\rho^I / \rho^M = 2/3$

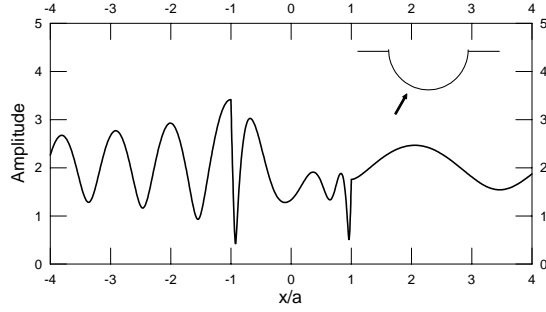
(e) ~ (h) Manoogian's results [60]



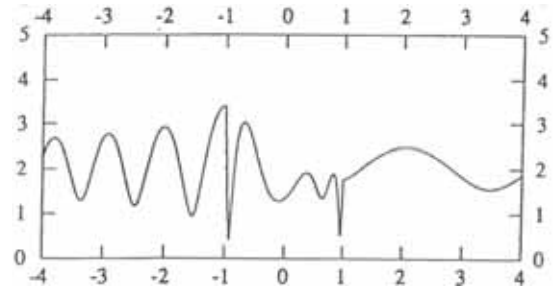
(a) $\gamma = 0^\circ$



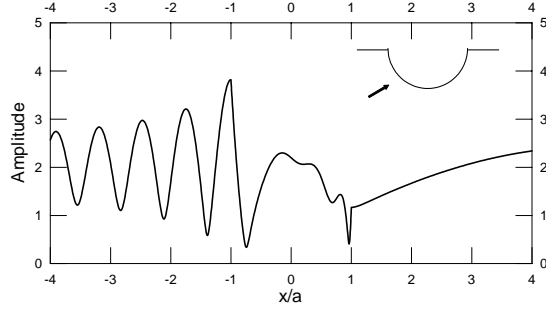
(e) $\gamma = 0^\circ$



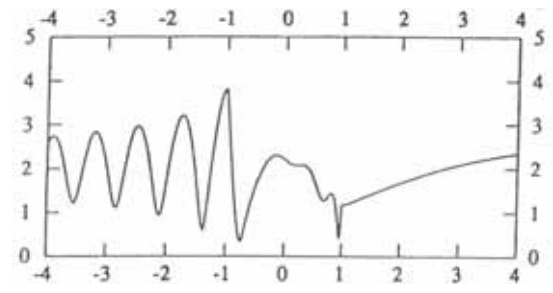
(b) $\gamma = 30^\circ$



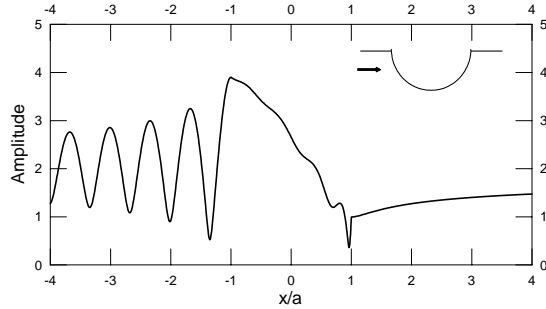
(f) $\gamma = 30^\circ$



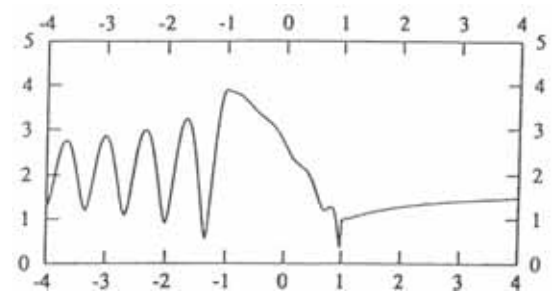
(c) $\gamma = 60^\circ$



(g) $\gamma = 60^\circ$



(d) $\gamma = 90^\circ$

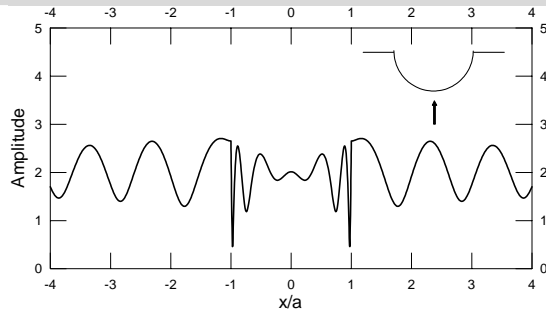


(h) $\gamma = 90^\circ$

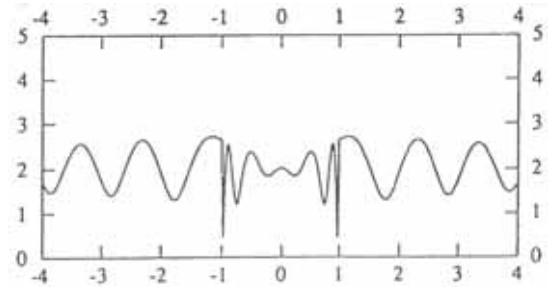
Figure 4-12 Limiting case of a canyon ($\mu^I / \mu^M = 10^{-8}$ and $\eta = 1.5$).

(a) ~ (d) Present method $\rho^I / \rho^M = 2/3$

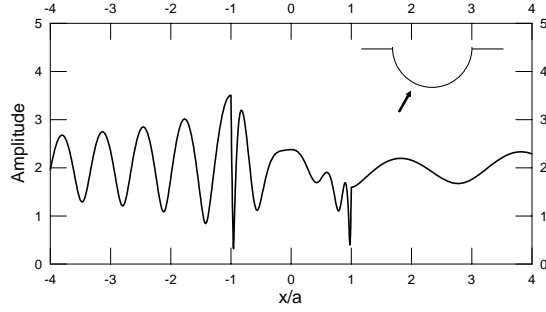
(e) ~ (h) Manoogian's results [60]



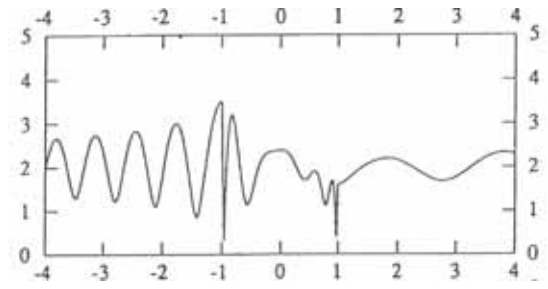
(a) $\gamma = 0^\circ$



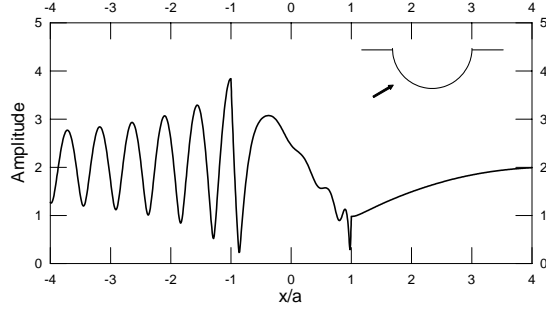
(e) $\gamma = 0^\circ$



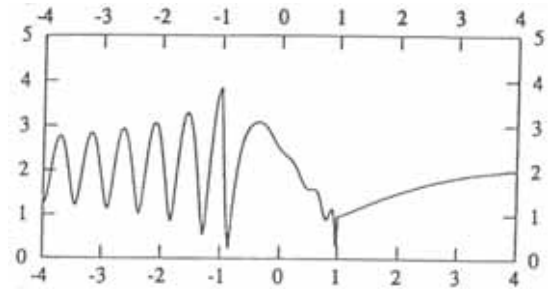
(b) $\gamma = 30^\circ$



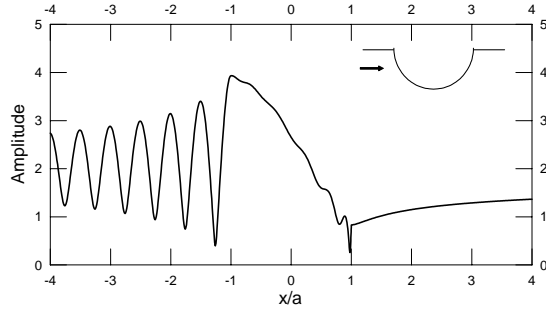
(f) $\gamma = 30^\circ$



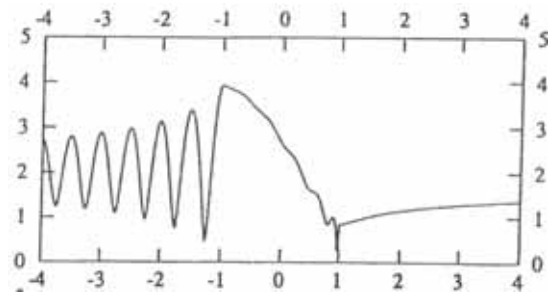
(c) $\gamma = 60^\circ$



(g) $\gamma = 60^\circ$



(d) $\gamma = 90^\circ$



(h) $\gamma = 90^\circ$

Figure 4-13 Limiting case of a canyon ($\mu^I / \mu^M = 10^{-8}$ and $\eta = 2$).

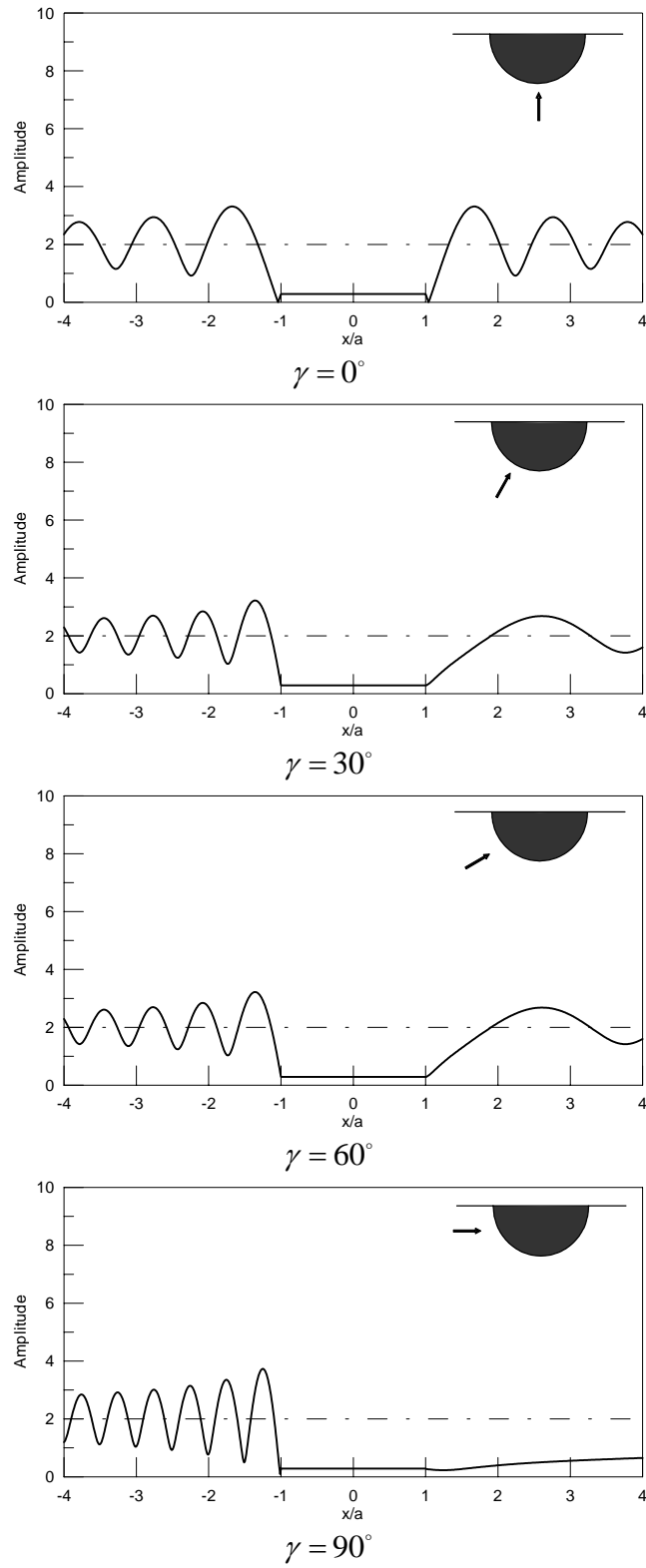
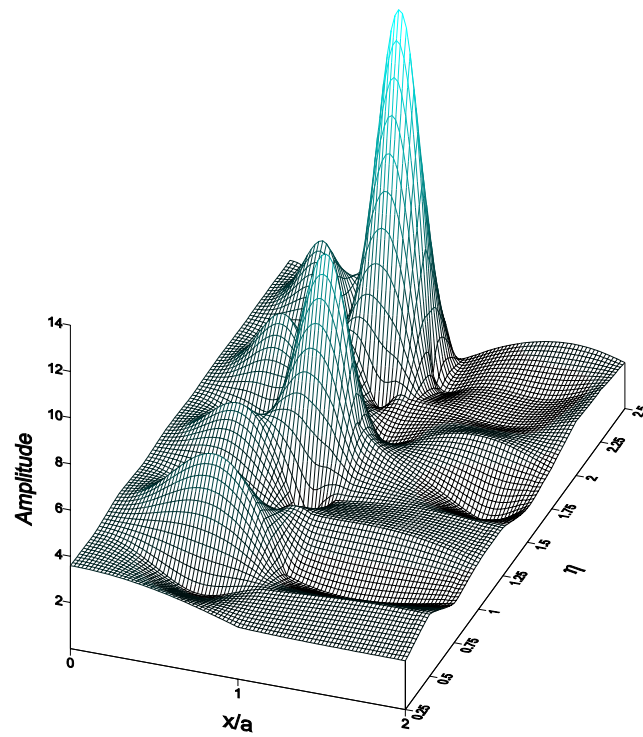
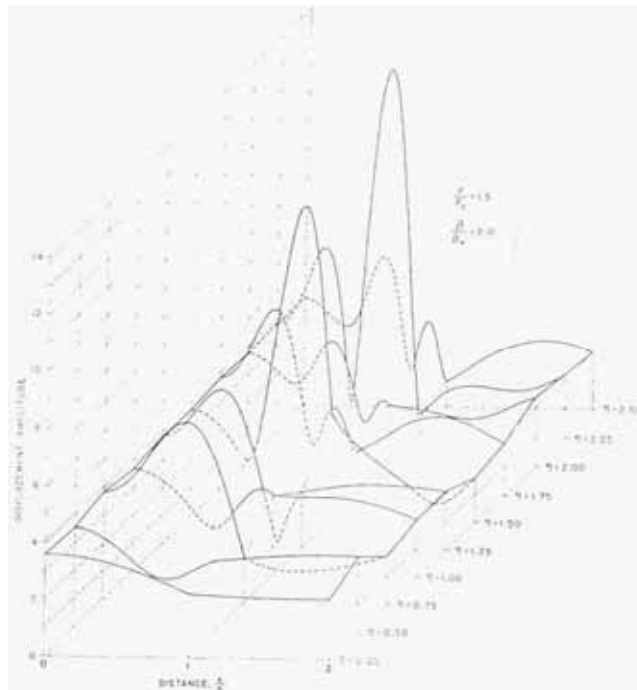


Figure 4-14 Limiting case of a rigid alluvial valley ($\mu^I = \mu^M = 10^4$, $\rho^I / \rho^M = 2/3$ and $\eta = 2$).

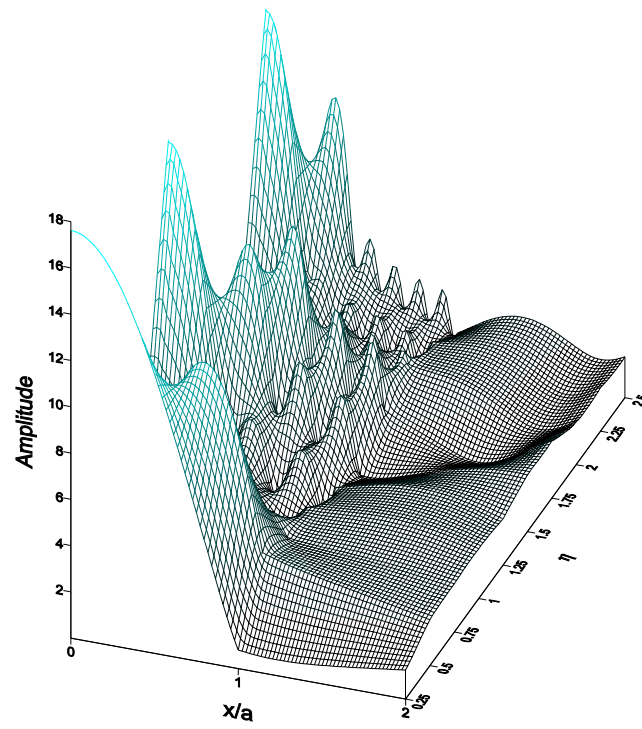


Present method ($\rho^I / \rho^M = 2/3$ and $c^I / c^M = 1/2$)

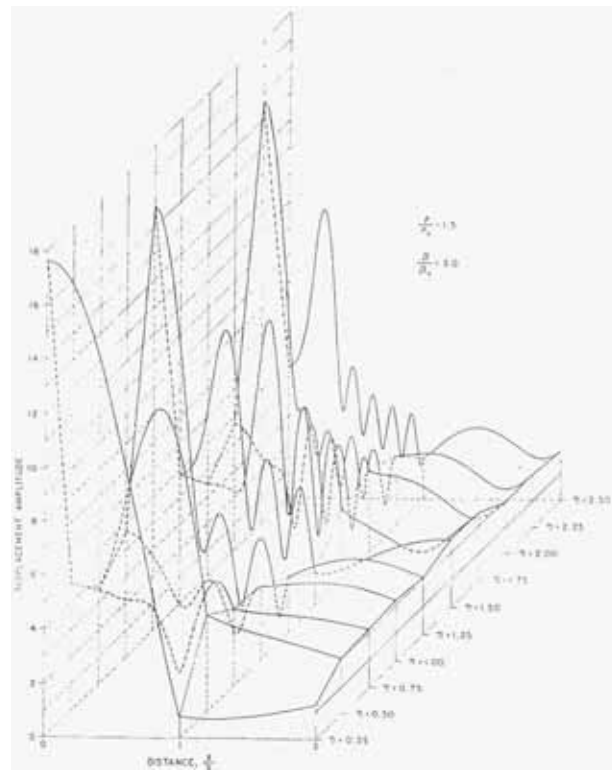


Trifunac's result [79]

Figure 4-15 Surface displacements as a function of x/a and η for the vertical incidence ($\gamma = 0^\circ$).

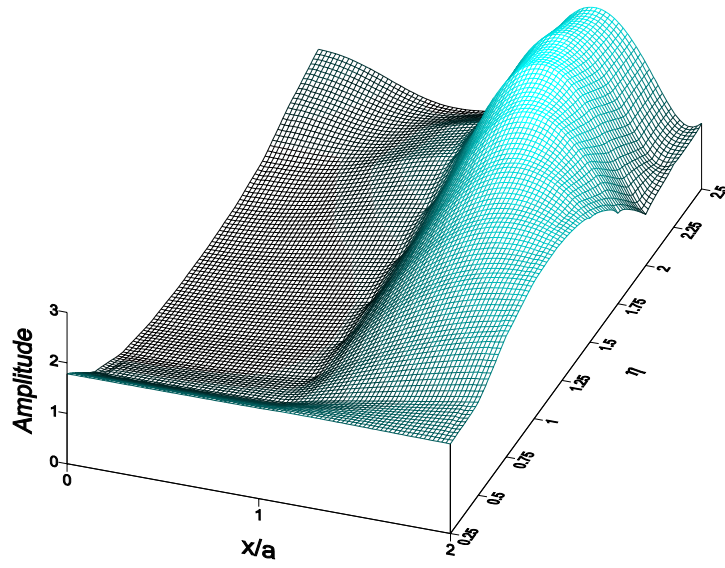


Present method ($\rho^I / \rho^M = 2/3$ and $c^I / c^M = 1/3$)

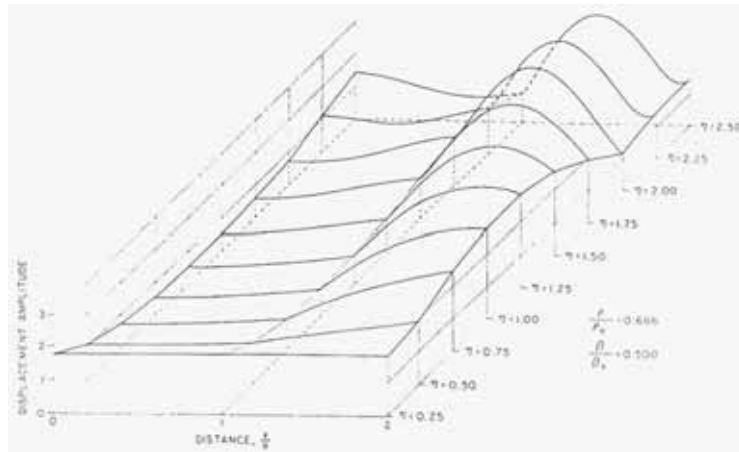


Trifunac's result [79]

Figure 4-16 Surface displacements as a function of x/a and η for the vertical incidence ($\gamma = 0^\circ$).

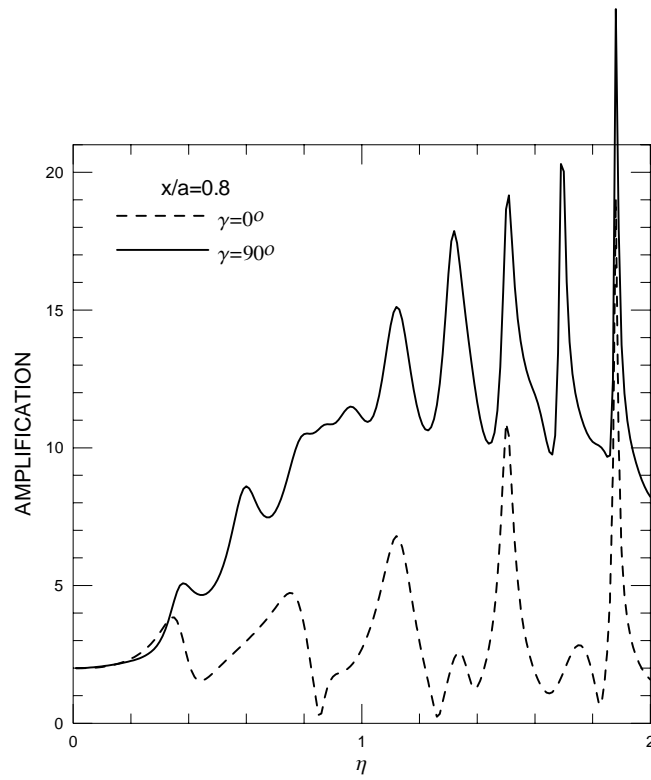


Present method ($\rho^I / \rho^M = 3/2$ and $c^I / c^M = 2$)

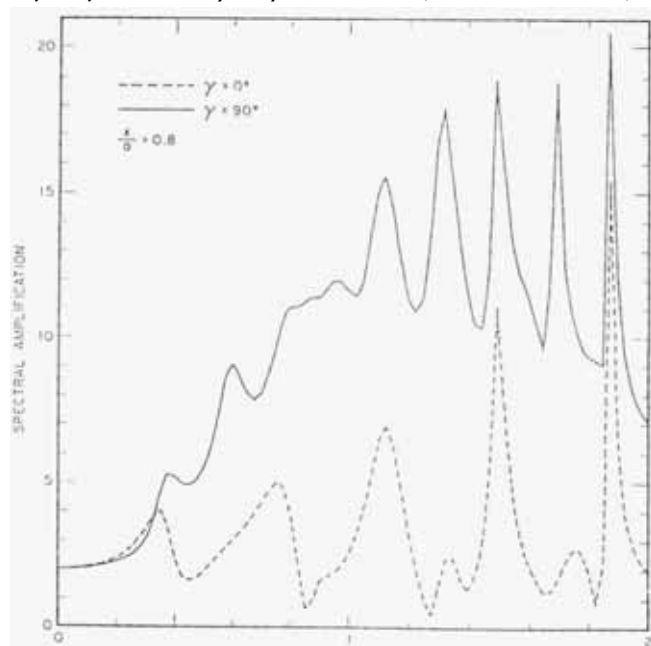


Trifunac's result [79]

Figure 4-17 Spectral displacement with harder material of alluvial valley versus the dimensionless frequency η for the vertically incident SH-wave.

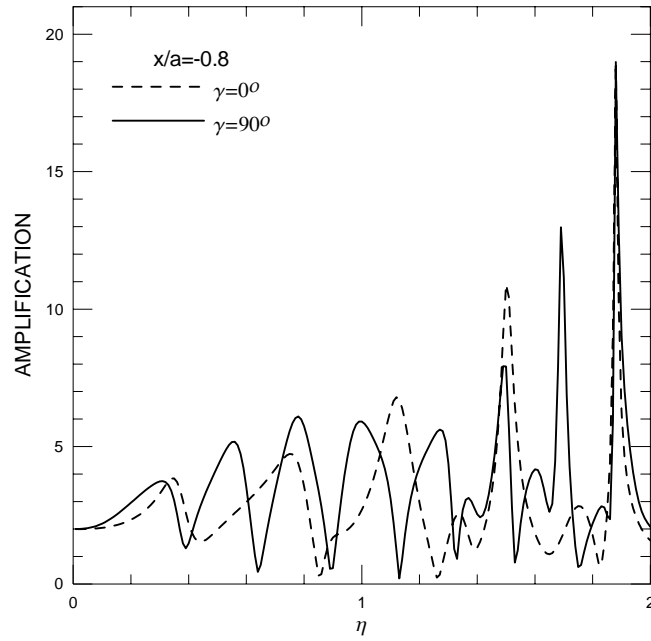


$\mu^I / \mu^M = 1/6, \rho^I / \rho^M = 2/3$ (Present method)

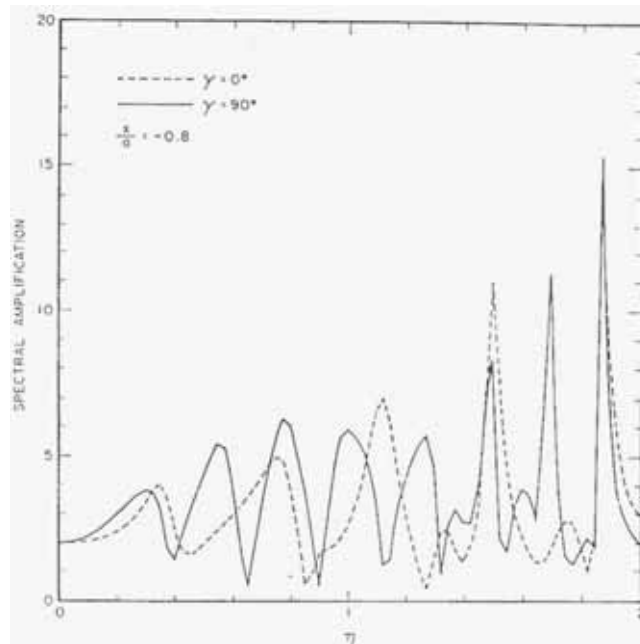


Trifunac's result [79]

Figure 4-18 Spectral amplification at $x/a = 0.8$ versus the dimensionless frequency η (Present method and Trifunac's result).

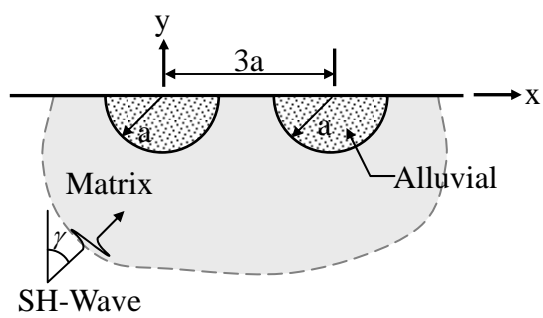


$\mu^I / \mu^M = 1/6, \rho^I / \rho^M = 2/3$ (Present method)



Trifunac's result [79]

Figure 4-19 Spectral amplification at $x/a = -0.8$ versus the dimensionless frequency η (Present method and Trifunac's result).



ρ_l : density of alluvial

ρ_M : density of matrix

μ_l : shear modulus of alluvial

μ_M : shear modulus of matrix

γ : the angle of incident wave and y-axis

Figure 4-20 A half-plane problem with two alluvial valleys subject to the incident SH-wave.

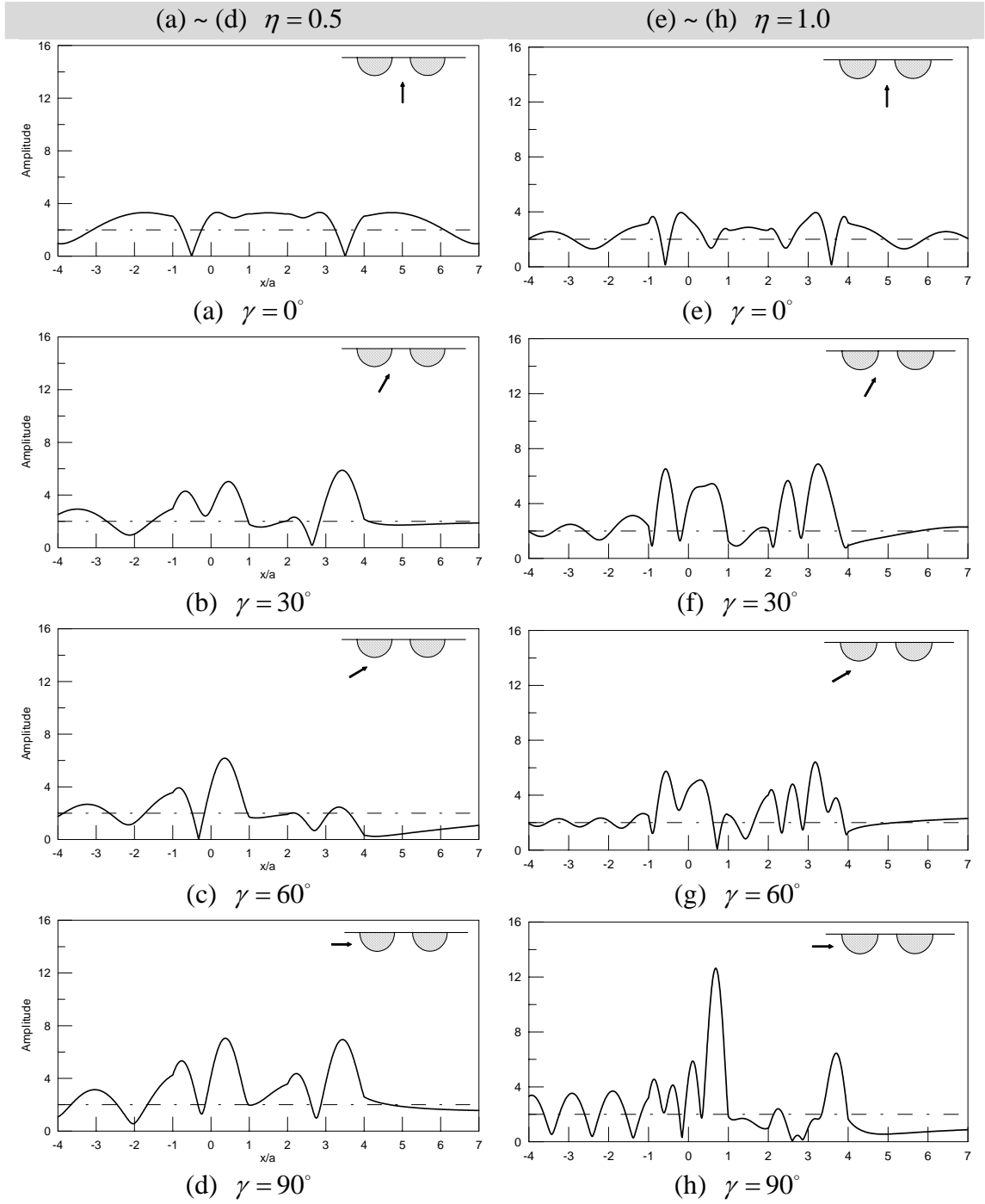


Figure 4-21 Surface displacements of two alluvial valleys ($\mu^I / \mu^M = 1/6$ and $\rho^I / \rho^M = 2/3$).

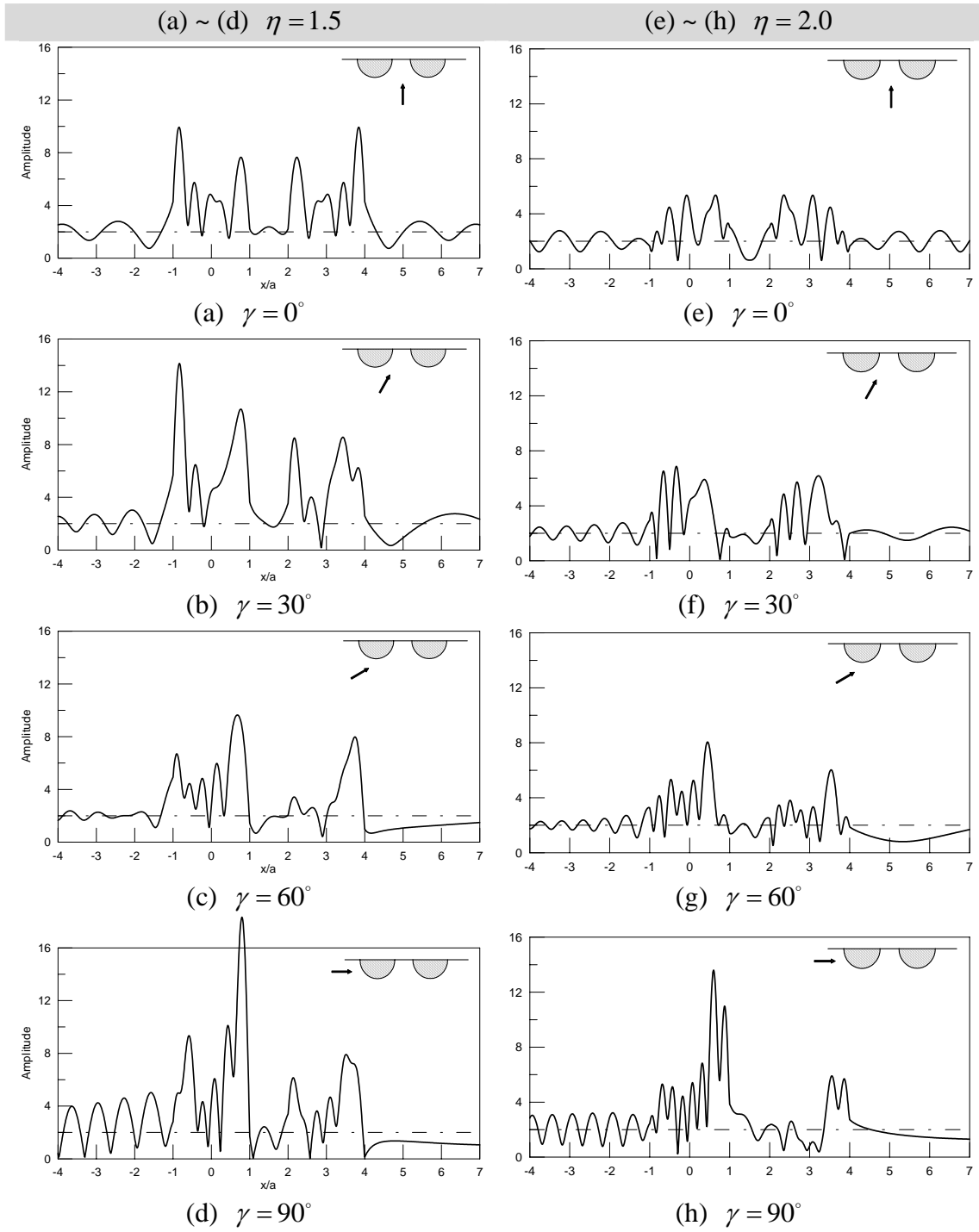


Figure 4-22 Surface displacements of two alluvial valleys ($\mu^I / \mu^M = 1/6$ and $\rho^I / \rho^M = 2/3$).

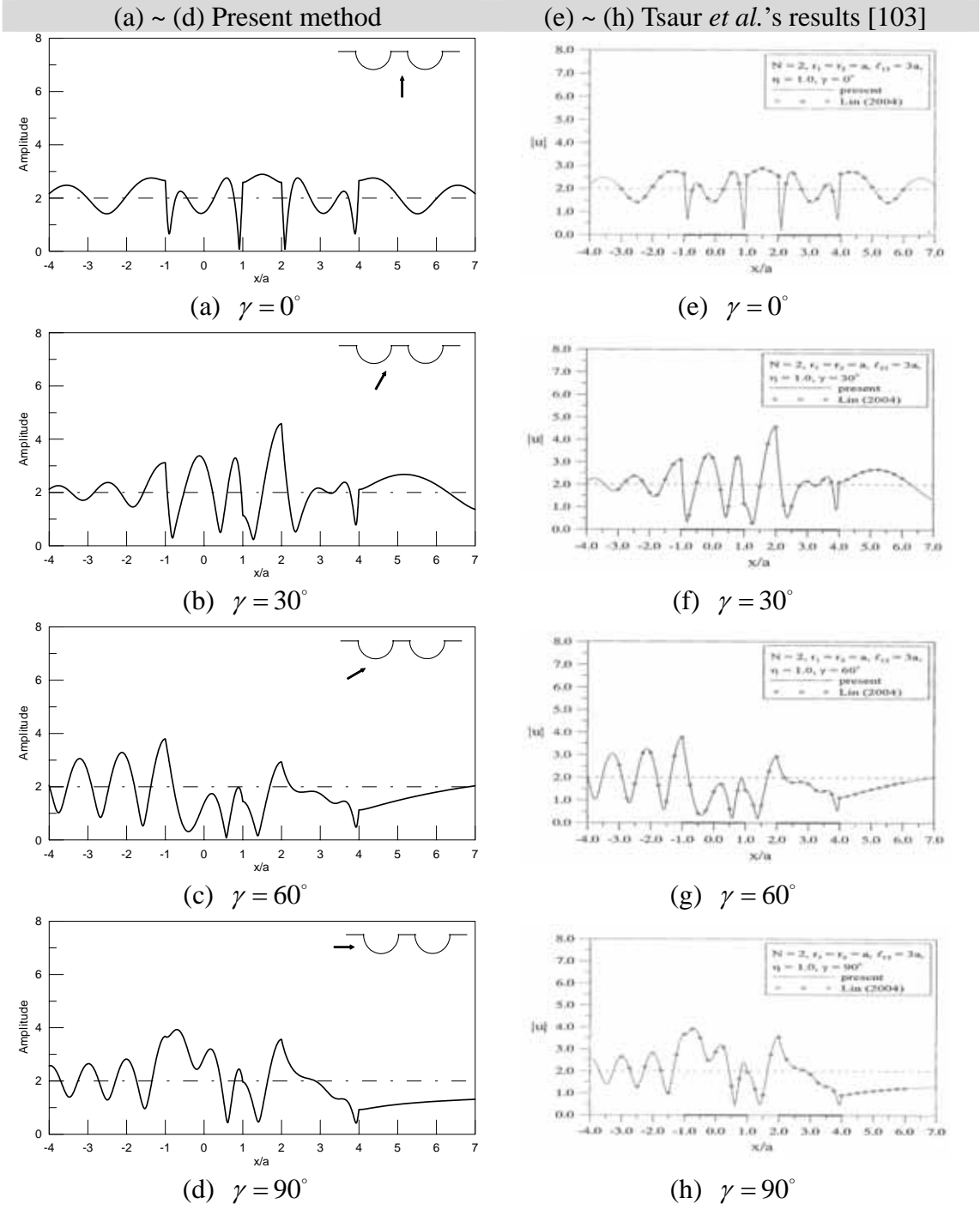


Figure 4-23 Limiting case of two canyons ($\mu^I / \mu^M = 10^{-8}$ and $\eta = 1$).

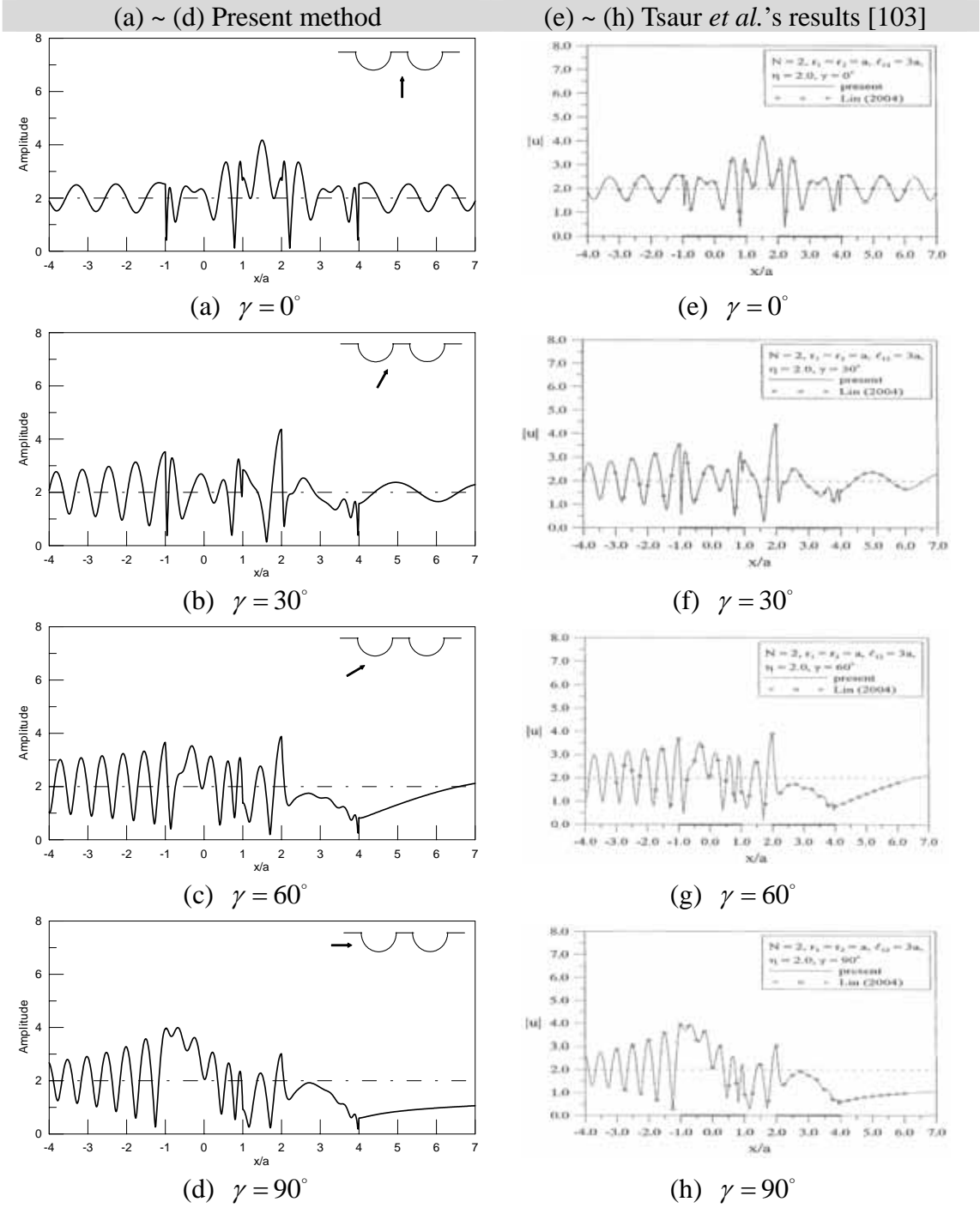
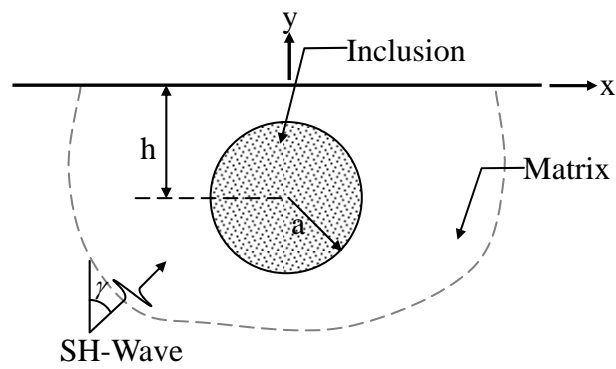


Figure 4-24 Limiting case of two canyons ($\mu^I / \mu^M = 10^{-8}$ and $\eta = 2$).



ρ^I : density of inclusion

ρ^M : density of matrix

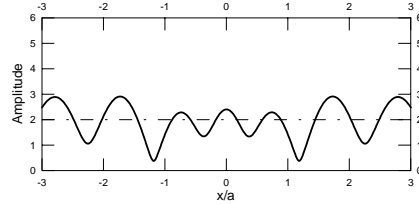
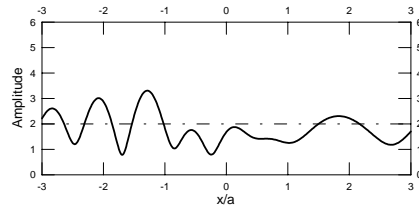
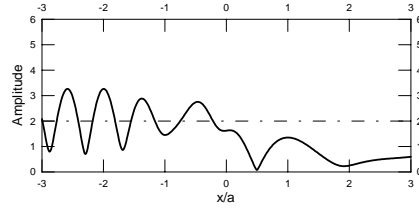
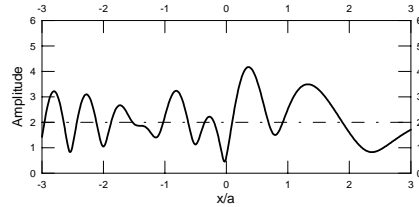
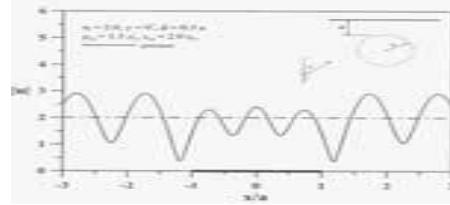
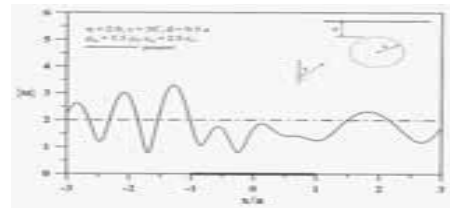
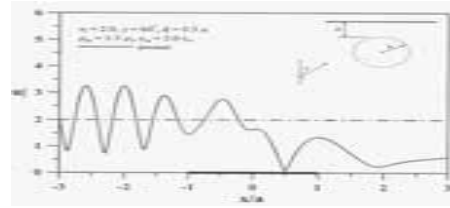
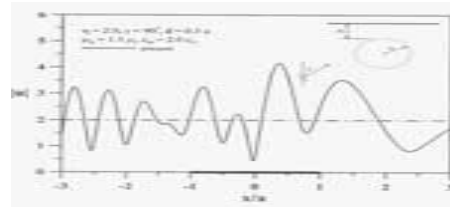
μ^I : shear modulus of inclusion

μ^M : shear modulus of matrix

γ : angle of incident wave and y-axis

Figure 4-25 A half-plane problem with a circular inclusion subject to the incident SH-wave.

(a) ~ (d) Present method

(a) $\gamma = 0^\circ$ (b) $\gamma = 30^\circ$ (c) $\gamma = 60^\circ$ (d) $\gamma = 90^\circ$ (e) ~ (h) Tsaui *et al.*'s results[102](e) $\gamma = 0^\circ$ (f) $\gamma = 30^\circ$ (g) $\gamma = 60^\circ$ (h) $\gamma = 90^\circ$

(i) ~ (l) Manoogian and Lee's results [62]

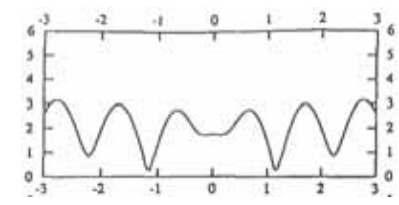
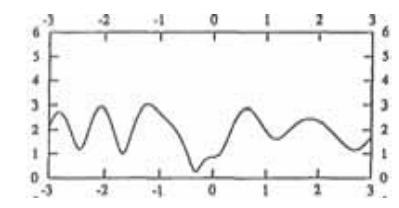
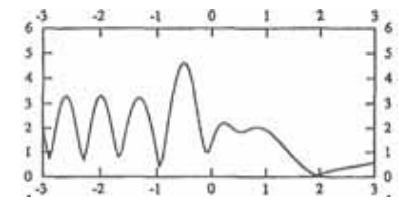
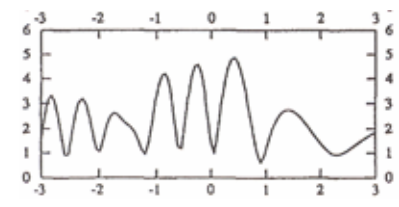
(i) $\gamma = 0^\circ$ (j) $\gamma = 30^\circ$ (k) $\gamma = 60^\circ$ (l) $\gamma = 90^\circ$

Figure 4-26 Surface displacements of a inclusion problem under the ground surface with $\eta = 2$ and $h/a = 1.5$ ($\mu^I / \mu^M = 1/6$, $\rho^I / \rho^M = 2/3$).

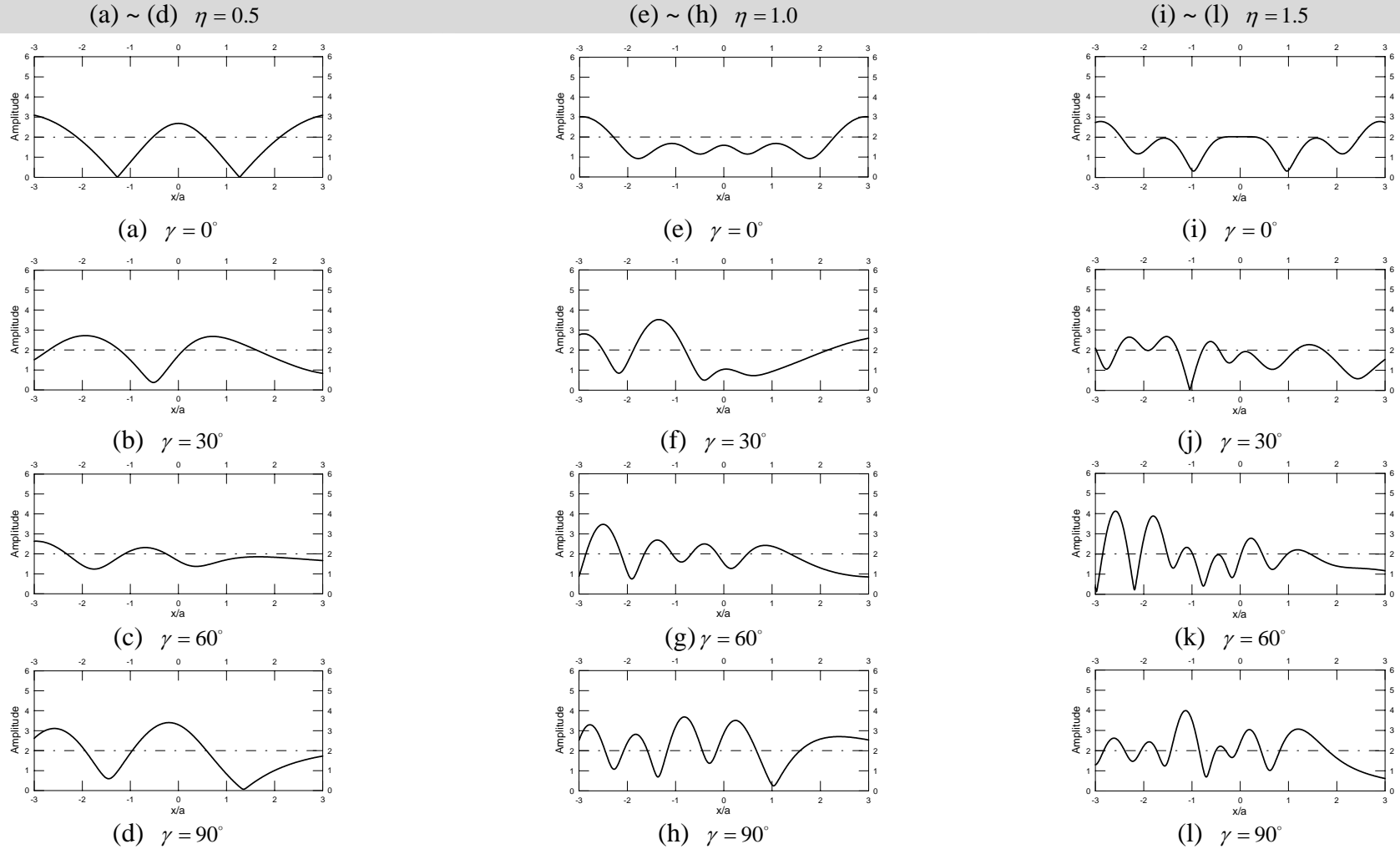


Figure 4-27 Surface amplitudes of the inclusion problem for various values of η and $h/a = 1.5$ ($\mu^l / \mu^M = 1/6$, $\rho^l / \rho^M = 2/3$).

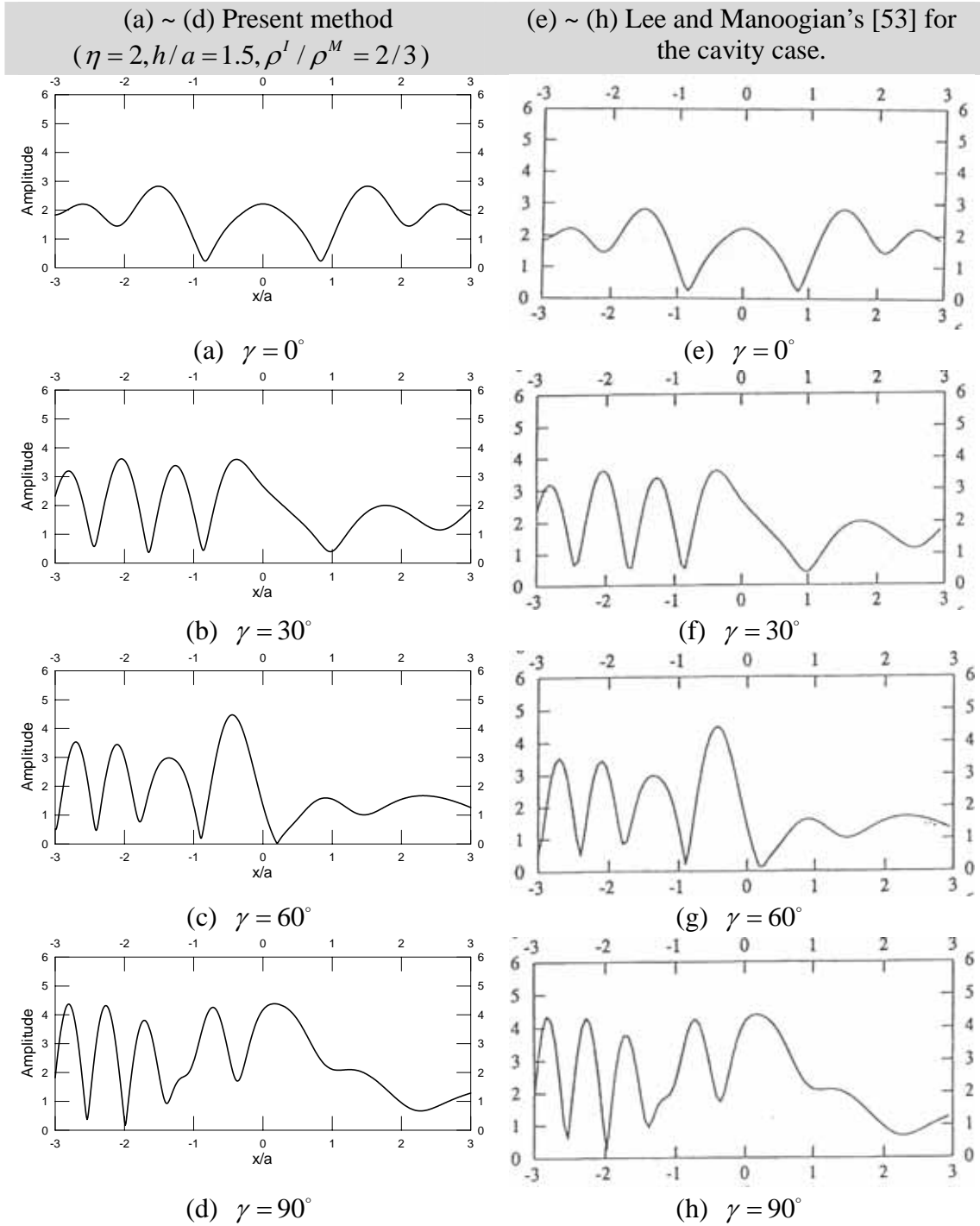


Figure 4-28 Limiting case of a cavity problem ($\mu^I / \mu^M = 10^{-8}$).

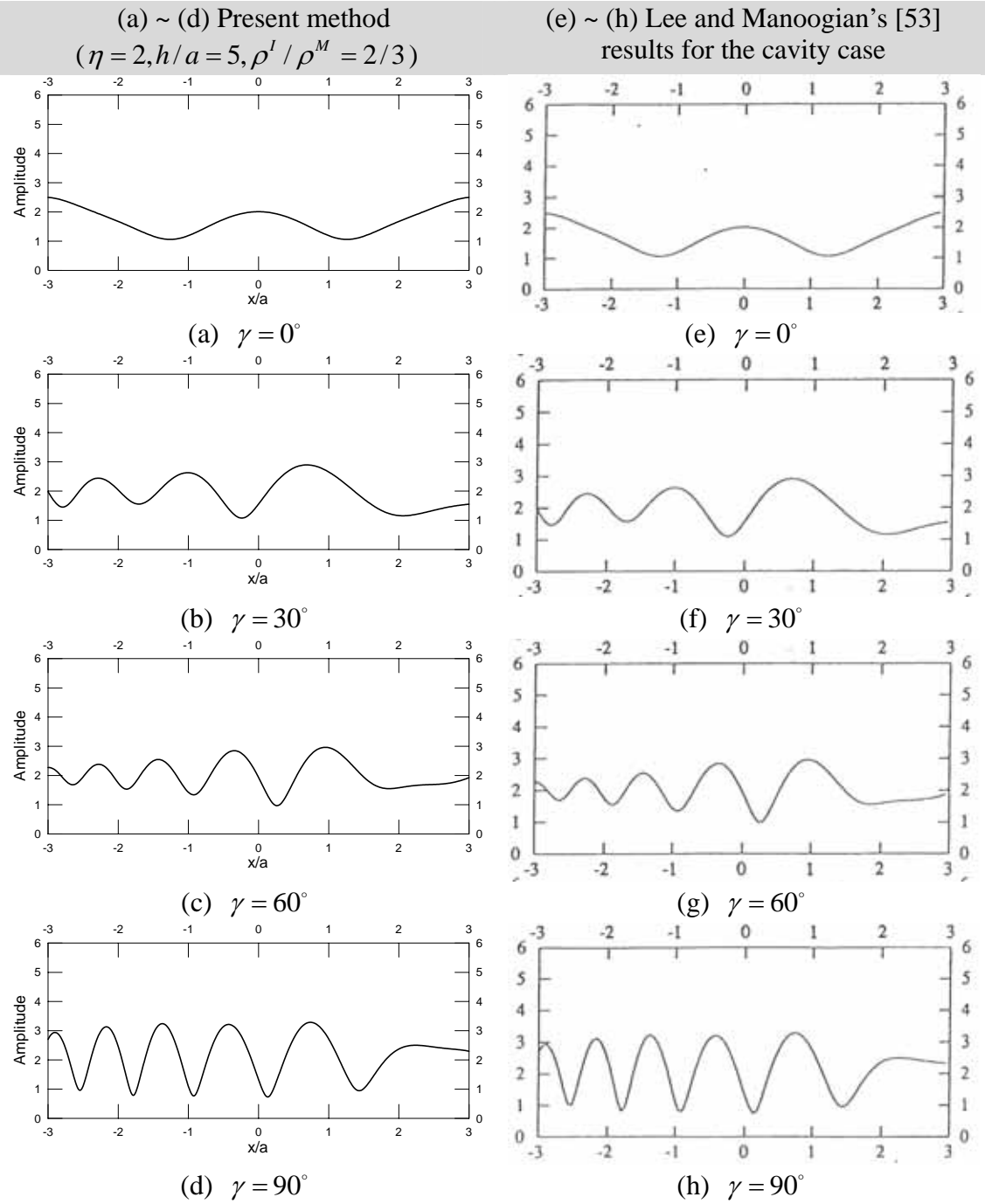


Figure 4-29 Limiting case of a cavity problem ($\mu^I / \mu^M = 10^{-8}$).

$$h/a=1.5, \rho^I / \rho^M = 2/3 \text{ and } \eta=2$$

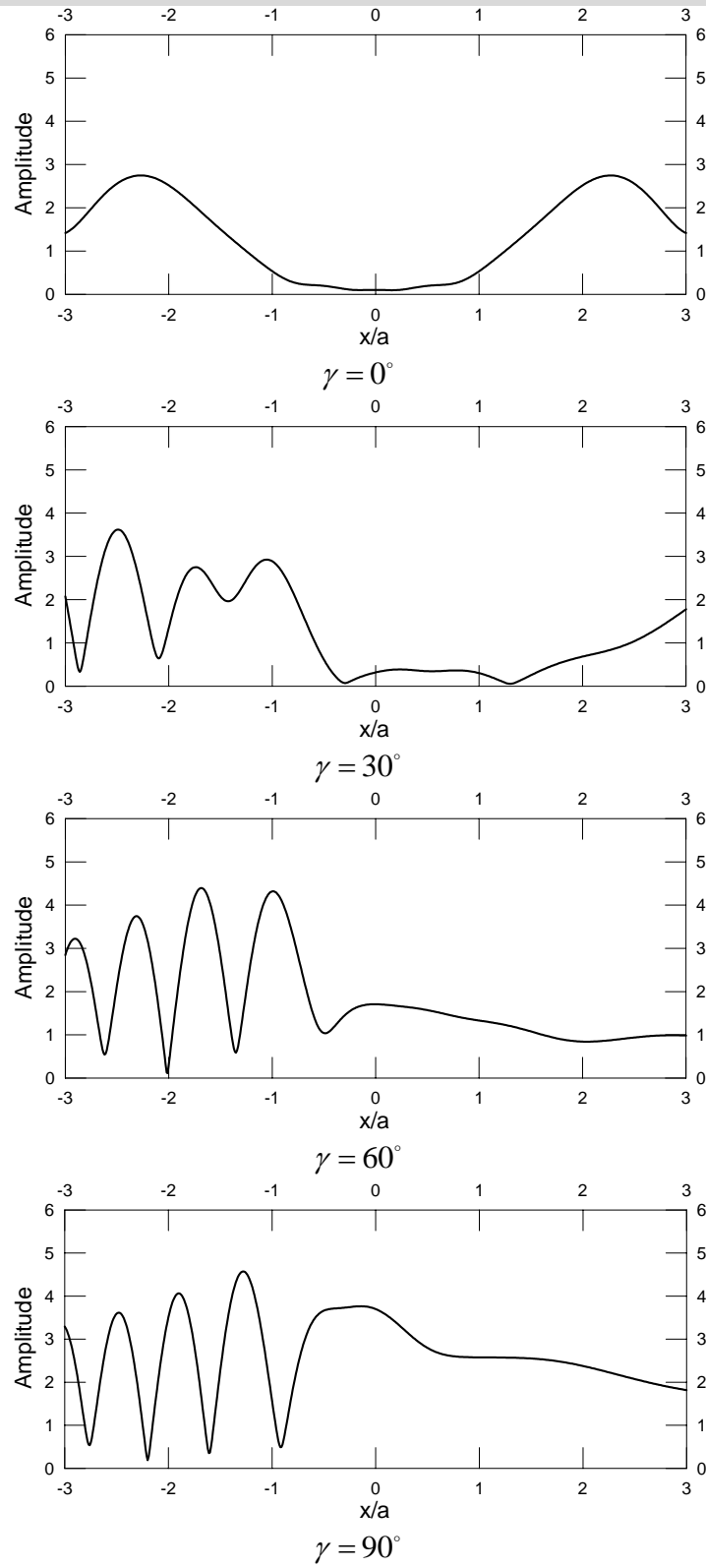
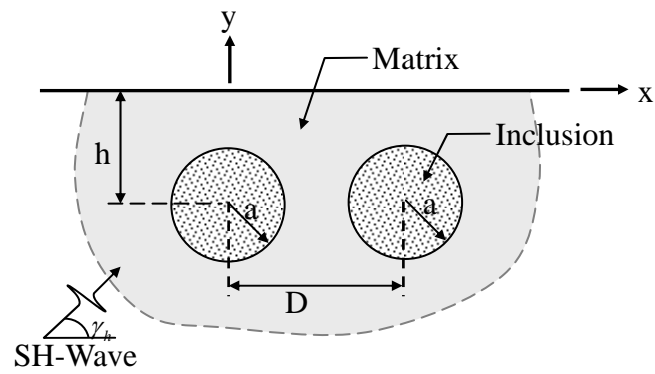


Figure 4-30 Limiting case of a rigid inclusion problem ($\mu^I / \mu^M = 10^4$).



ρ^I : density of inclusion
 ρ^M : density of matrix
 μ^I : shear modulus of inclusion
 μ^M : shear modulus of matrix
 γ_h : angle of incident and x-axis

Figure 4-31 A half-plane problem with two circular inclusions subject to the SH-wave.

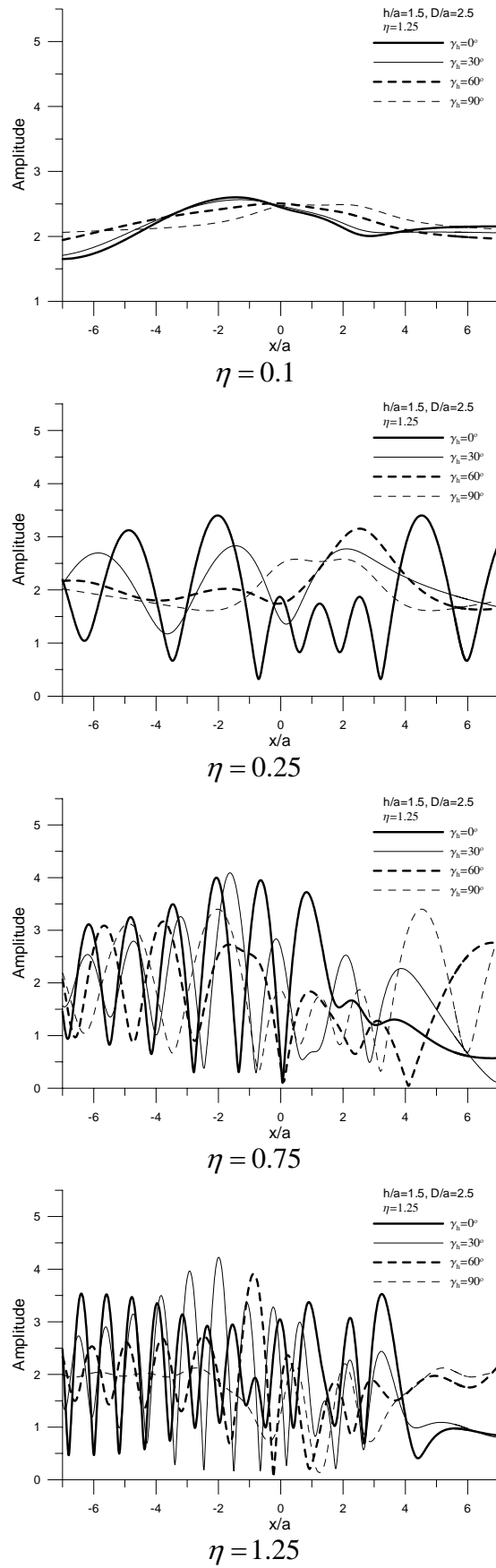


Figure 4-32 Surface amplitudes of two-inclusions problem
 $(\mu^I / \mu^M = 1/6, \rho^I / \rho^M = 2/3, h/a = 1.5, D/a = 2.5, L = 10)$.

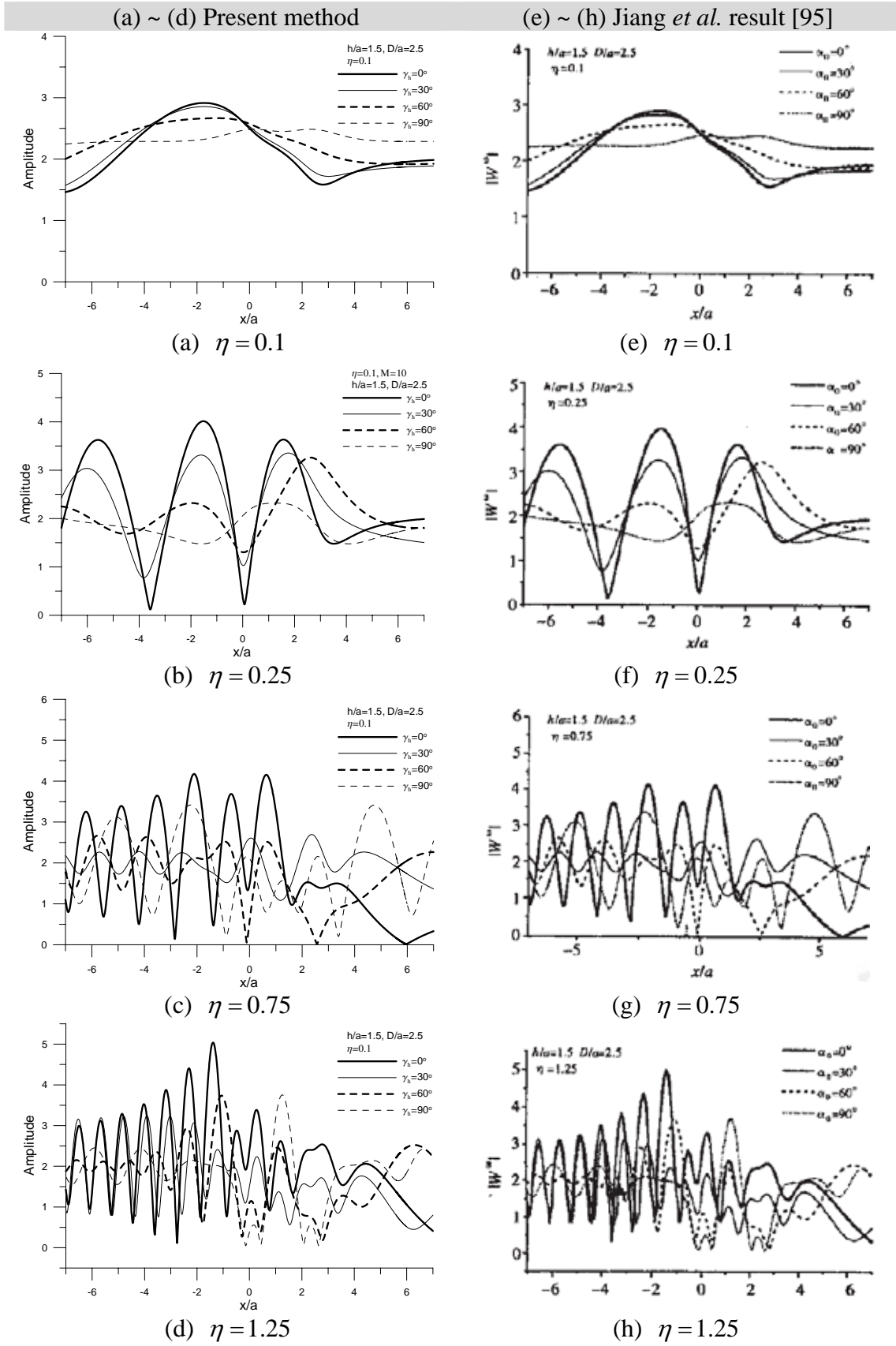
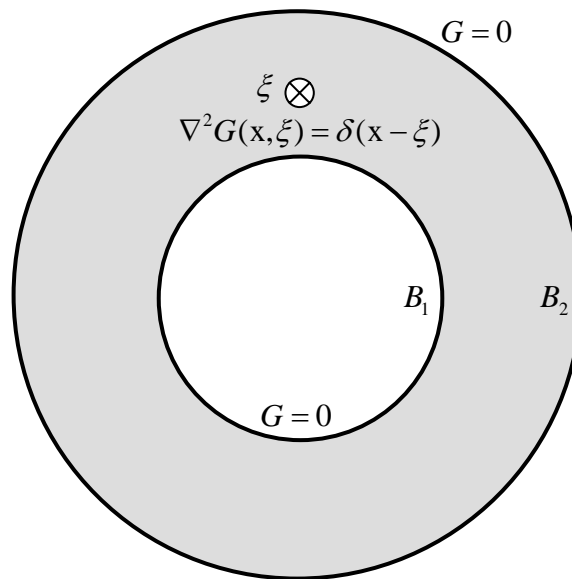
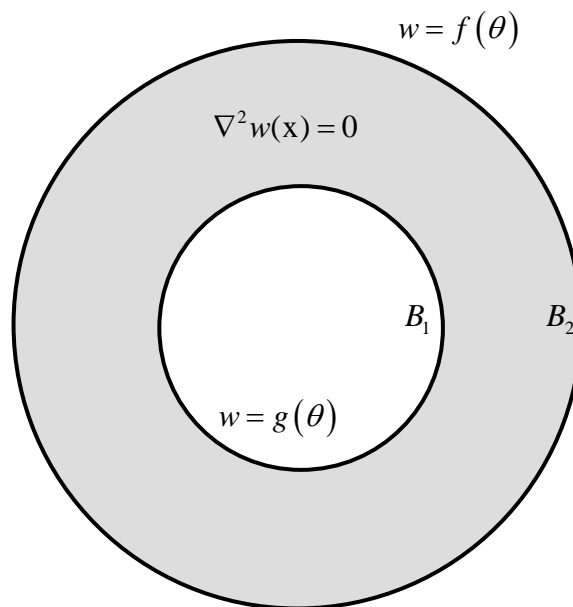


Figure 4-33 Limiting case of two-cavities problem
 $(\mu^l / \mu^M = 10^{-8}, \rho^l / \rho^M = 2/3, h/a = 1.5, D/a = 2.5 \text{ and } L = 10)$.

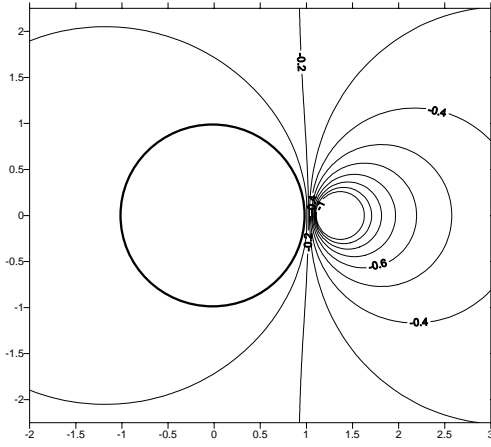


(a) Green's function of an annular case

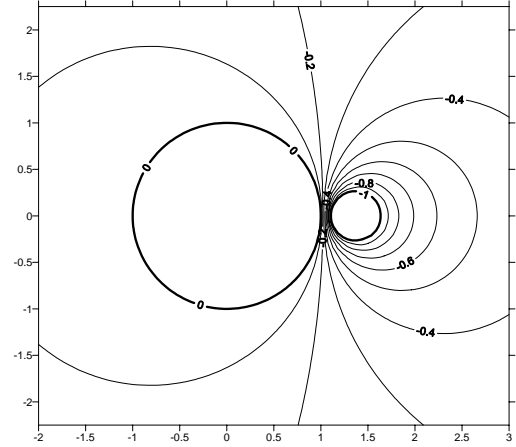


(b) An annular Dirichlet problem

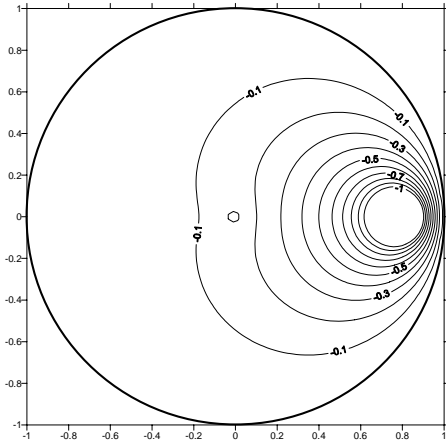
Figure 5-1 A two-dimensional annular problem



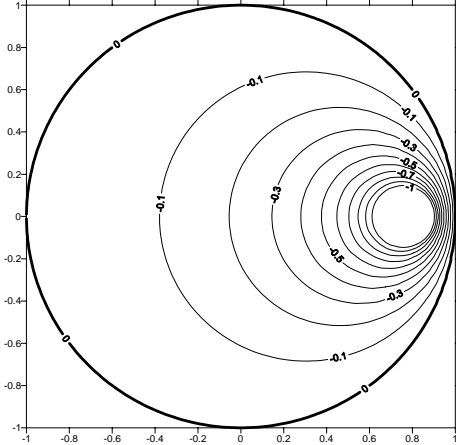
(a) Limiting case of the annular Green's function ($a = 1, b = 10^7, L = 20, \xi(1.25, 0^\circ)$)



(c) Series-form Green's function of exterior case [31]



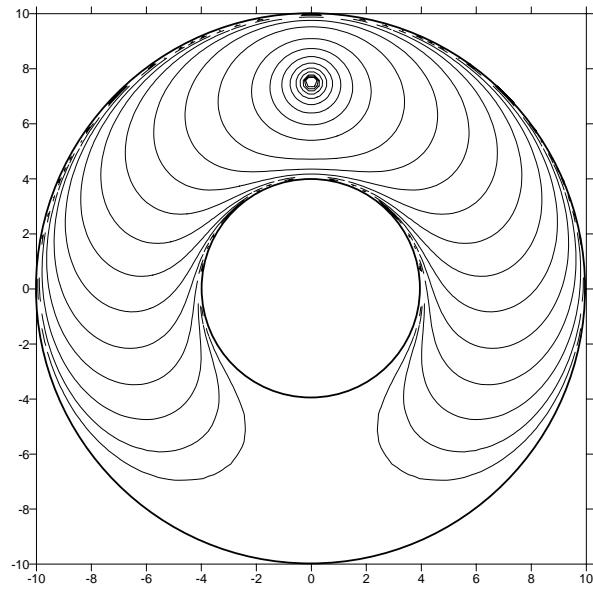
(b) Limiting case of the annular Green's function ($a = 0.001, b = 1, L = 20, \xi(0.8, 0^\circ)$)



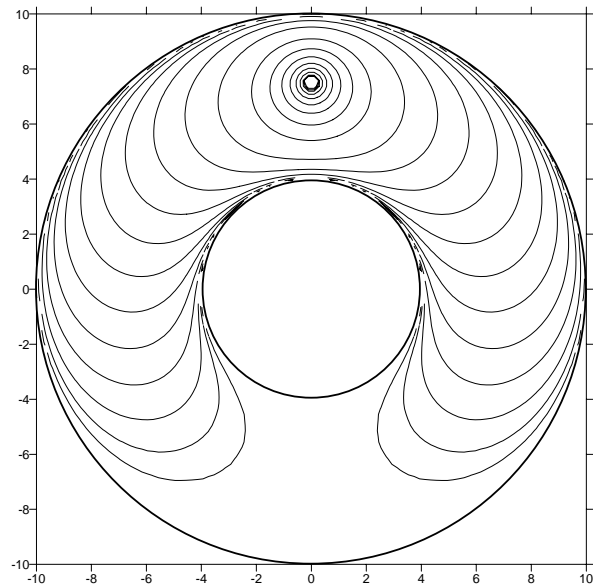
(d) Series-form Green's function of interior case [31]

Figure 5-2 Two limiting cases ($a \rightarrow 0, b \rightarrow \infty$) of the annular Green's function

- (a) $a = 1, b = 10^7, L = 20, \xi(1.25, 0^\circ)$
- (b) $a = 0.001, b = 1, L = 20, \xi(0.8, 0^\circ)$
- (c) Exterior case [31]
- (d) Interior case [31]



(a) Analytical solution ($L = 50$)



(b) Semi-analytical solution ($L = 50$)

Figure 5-3 Contour plots for the annular Green's function

作者簡歷

中文姓名：陳柏源

英文姓名：Po-Yuan Chen

出生日期：民國 71 年 06 月 17 日

籍貫：台灣省新竹縣

聯絡地址：303 新竹縣湖口鄉愛勢村民族街 181 號

聯絡電話：(03)5993-308

行動電話：0919-391493

E-mail address: M93520010@mail.ntou.edu.tw



學歷：

國立台灣海洋大學河海工程研究所碩士 (2004.8 ~ 2006.7)

國立台灣海洋大學河海工程系學士 (2000.8 ~ 2004.7)

國立新竹高級中學 (1997.8 ~ 2000.7)

新竹縣立新湖國中 (1994.8 ~ 1997.7)

新竹縣立新湖國小 (1988.8 ~ 1994.7)

著作：

(A) 期刊論文

- 1 Chen, J.T., Shen, W.C., Chen, P.Y., 2006, Analysis of circular torsion bar with circular holes using null-field approach, *Computer Modeling in Engineering Science*, Vol.12 (2), pp.109-119.
- 2 Chen, J.T. and Chen, P.Y., 2006, A semi-analytical approach for stress concentration of cantilever beams with circular holes under bending, *submitted*.
- 3 Chen, J.T., Chen, P.Y. and Liao H.Z., 2006, Derivation of Green function and Poisson integral formula for annular Laplace problems, *submitted*.
- 4 Chen, J.T., Chen C.T., Chen, P.Y. and Chen I.L., 2006, A semi-analytical approach for radiation and scattering problems with circular boundaries, *submitted*.

(B) 會議論文

- 1 Chen, P.Y. and Chen, J.T., 2006, A semi-analytical approach for stress concentration of cantilever beams with circular holes under bending, *The 8th National Conference on Structure Engineering*, Sun Moon Lake, Taiwan.
- 2 Chen, P.Y., Chen, C.T. and Chen, J.T., 2005, A semi-analytical approach for dynamic stress concentration factor of Helmholtz problems with circular holes, *The 29th National Conference on Theoretical and Applied Mechanics*, NTHU, Hsinchu.
- 3 Shen, W.C., Chen, P.Y. and Chen, J.T., 2005, Analysis of circular torsion bar with circular holes using null-field approach, *九十四年電子計算機於土木水利工程應用研討會*, 台南成大.